UNIVERSITÀ DELLA CALABRIA

UNIVERSITA' DELLA CALABRIA

Dipartimento di Fisica

Scuola di Dottorato

"Archimede", in Science, Comunicazione e Tecnologie

Indirizzo

Scienze e Tecnologie dei Sistemi Complessi

CICLO XXVII

NEUTRON INDUCED SINGLE EVENT BURNOUT ON POWER MOSFETs

Settore Scientifico Disciplinare: ING-INF/01

Direttore: Ch.mo Prof. Pietro Pantano
Firma Pietro Pantano

Supervisore: Ch.mo Prof. Calogero Pace
Firma Calogero Pace

Dottorando: Dott. Carlo Giordano
Firma

Pubblication list

1. Consentino, G.; Laudani, M.; Privitera, G.; Parlato, A.; Marchese, N.; Tomarchio, E.; Pace, C.; **Giordano, C.**; Mazzeo, M.; Ambato, J.L.H., "Dangerous effects induced on power MOSFETs by terrestrial neutrons: A theoretical study and an empirical approach based on accelerated experimental analysis," AEIT Annual Conference, 2013 , vol., no., pp.1,6, 3-5 Oct. 2013, doi: 10.1109/AEIT.2013.6666813;

2. Consentino, G.; De Pasquale, D.; Galiano, S.; D'Ignoti, A.; Pace, C.; Hernandez Ambato, J.L.; Mazzeo, M.; **Giordano, C.**, "Innovative instrumentation for HTRB tests on semiconductor power devices," AEIT Annual Conference, 2013 , vol., no., pp.1,5, 3-5 Oct. 2013, doi: 10.1109/AEIT.2013.6666814;

3. Consentino, G.; Laudani, M.; Privitera, G.; Pace, C.; **Giordano, C.**; Hernandez, J.; Mazzeo, M., "Effects on power transistors of Terrestrial Cosmic Rays: Study, experimental results and analysis," Applied Power Electronics Conference and Exposition (APEC), 2014 Twenty-Ninth Annual IEEE , vol., no., pp.2582,2587, 16-20 March 2014, doi: 10.1109/APEC.2014.6803667.

Acronyms

ADC Analog to Digital Converter

ANITA Atmospheric like Neutrons from a thIck TArget

API Application Programming Interface

ASER Accelerated Soft Error Rate

AWP Automated WorkPlace

BORN Beam Off with pReset flueNce

COTS Commercial Of The Shelf

CVI C Virtual Instrument

DAQ Data AcQuisition

DMOS Double Diffused MOS

DUT Device Under Test

ECAD Electronic Computer Aided Design

ENDF Evaluated Nuclear Data Files

ESR Equivalent Series Resistance

FIB Focused Ion Beam

FIT Failure In Time

GPIB General Purpose Interface Bus

GUI Graphical User Interface

HV High Voltage

LCD Linear Charge Deposition

LDMOS Lateral Diffused MOS

LET Linear Energy Transfer

MCNP Monte Carlo N Particle transport code system

MTTF Mean Time To Failure

NPLC Number of Power Line Cycles

NRSE Non Referenced Single Ended

PCB Printed Circuit Board

PGIA Programmable Gain Instrumentation Amplifier

PMMA Poly Methyl Metha Crylate

SCPI Standard Command for Programmable Instruments

SEB Single Event Burnout

SEGR Single Event Gate Rupture

SEE Single Event Effect

SER Soft Error Rate

SEU Single Event Upset

SJ Super Junction

SHV Safe High Voltage

SMU Source Measuring Unit

SOA Safe Operating Area

SPICE Simulation Program with Integrated Circuit Emphasis

SRIM Stopping and Range of Ions in Matter

SUP Standard User Position

TCAD Technology Computer Aided Design

TEOS TetraEthyl OrthoSilicate

TFBC Thin Film Breakdown Counter

TFS Trench Field Stop

TDMS Technical Data Management Streaming

TRIM Transport and Range of Ions in Matter

TSL Theo Svedberg Laboratory

UniPA University of PAlermo

USB Universal Serial Bus

VDMOS Vertical Diffused MOS

VISA Virtual Instrument Software Architecture

Contents

List of Figures

List of Tables

Abstract

Il presente lavoro di tesi ha come oggetto lo studio dei SEB su MOSFET di potenza. In generale, questa tematica si inquadra nell'ambito dell'affidabilità dei dispositivi a semiconduttore, con particolare riferimento agli effetti indotti dalle radiazioni. Il SEB appartiene ai cosiddetti Single Event Effect (SEE), cioè agli effetti indotti dall'interazione di una singola particella estremamente energetica, come uno ione pesante, un protone o un neutrone. Storicamente, i primi SEB sono stati riscontrati in ambito aerospaziale ed associati ai raggi cosmici, composti per lo più da particelle cariche ad alta energia. Più recentemente, fallimenti analoghi sono stati osservati anche in applicazioni terrestri, come gli inverter per i pannelli fotovoltaici. Infatti, anche al livello del mare, questi dispositivi sono esposti ad una pioggia di neutroni aventi energie comprese tra qualche eV e il centinaio di MeV e derivanti dall'interazione primaria tra i raggi cosmici provenienti dallo spazio e l'atmosfera terrestre. Rispetto alle particelle cariche, i neutroni ionizzano attraverso meccanismi indiretti, tramite l'emissione di particelle cariche secondarie risultanti da reazioni nucleari, fissione, spallazione o decadimento radioattivo. L'effetto risultante della ionizzazione è la formazione di filamento di plasma all'interno dell'area attiva del dispositivo. A causa del campo elettrico associato alla polarizzazione tra i terminali di drain e source, le coppie elettrone-lacuna vengono separate, dando luogo ad una corrente transitoria. Inoltre, per effetto della ionizzazione da impatto, la carica iniziale viene moltiplicata e in taluni casi, la corrente risultante può essere talmente elevata da innescare l'accensione localizzata del transistore bipolare parassita, che è parte integrante della struttura di un power MOSFET. L'effetto finale è la formazione di hot spot che provoca un corto circuito tra drain e source a livello di cella.

Un parametro fondamentale per l'effettivo innesco dei SEB è la polarizzazione applicata. Tipicamente, infatti, i SEB si osservano solo per tensioni maggiori di un certo valore di soglia. Questo principio viene utilizzato per minimizzare le probabilità di fallimento dei MOSFET commerciali utilizzati in applicazioni terrestri. In sostanza si applica un margine di sicurezza sulla

tensione di breakdown, in modo da polarizzare i dispositivi ad una tensione inferiore al valore di soglia. Tale approccio, tuttavia, comporta una perdita di performance in termini di resistenza di on. Per questo motivo è necessario caratterizzare accuratamente questo parametro attraverso costose campagne sperimentali. Una interessante alternativa è rappresentata dagli strumenti TCAD, a patto di ottenere una ragionevole aderenza con i dati sperimentali.

L'attività di ricerca sui SEB da neutroni è stata condotta sia a livello sperimentale sia con simulazioni TCAD. Per quanto riguarda l'attività sperimentale, sono stati effettuati test accelerati, presso la sorgente Am-Be dell'Università di Palermo e la sorgente ANITA del The Svedberg Lab di Uppsala. In entrambi i casi, gli esperimenti sono stati effettuati su power MOSFET commerciali, forniti da ST Microelectronics. I dispositivi sono stati sottoposti ad un irraggiamento equivalente a 20 anni di esposizione ai neutroni terrestri a livello del mare, cioè l'intero ciclo di vita utile del pannello fotovoltaico, in diverse condizioni di polarizzazione. Attraverso questi esperimenti sono state effettuate delle valutazioni di failure rate e di MTTF. Successive investigazioni sono state compiute con l'ausilio di simulatori TCAD. In particolar modo, è stata proposta una nuova metodologia per la stima della tensione di soglia da SEB e del fattore di derating. Particolare attenzione è stata dedicata allo studio delle iterazioni nucleari, con specifiche elaborazioni delle sezioni d'urto del database Evaluated Nuclear Data Files (ENDF), al fine di ricavare, per un dato dispositivo e per un dato spettro energetico, le reazioni nucleari più probabili.

Introduction

Nowadays, power electronic devices are used in more and more branches of the human activities. One of the most important components used to commutate the energy flow is the power MOSFET. In particular, power MOSFETs are utilized as switch in electronic DC/DC power converters and inverters in many segments of the market such as industrial, automotive and telecommunication applications. Furthermore, in these last years, a huge increment of the demand was observed in the segment of applications for renewable energy such as photovoltaic. In such kind of market, power MOSFETs are largely utilized in the inverter block, managing up to 3 kW of electric power and the reliability of the systems need to be guaranteed for 20 to 25 years based on international and regional regulations. Typical devices used in such inverters are High Voltage Super Junction power MOSFETs or Trench Field Stop IGBT, with breakdown voltage between 600 V and 650 V. When used in these applications, converters are located outdoors, between sea level and 2000 m of altitude. In these conditions, the power transistors are exposed to natural radiation environment. In fact, when galactic cosmic rays coming from the outer space reach the earth's atmosphere, they collide with the nuclei of nitrogen and oxygen atoms and create cascades of secondary radiation, i.e. terrestrial cosmic rays which are composed of different kind of particles including protons, muons, pions and neutrons. On the contrary of charged particles, neutrons do not undergo Coulomb scattering and represent more than 95% of total particles at sea level.

Under specific operating conditions, a single neutron interaction may induce catastrophic failures, such as Single Event Burnout (SEB), Single Event Gate Rupture (SEGR) or both. These phenomena normally affect power MOSFETs operating in switching mode, polarized in the off-state, with applied bias near to the rated breakdown voltage. They involve filamentary current resulting from electron-hole pairs generated by ionization. In fact, neutrons are able to ionize in an indirect manner, by means of charged recoils generated as a result of nuclear reactions, radioactive decays, spallation and so on. After that, a positive feedback can be established, resulting in a drain-source short and/or a drain/gate short.

This can be a reliability issue not only for photovoltaic inverters, but also for all power electronic equipment operating in hostile radiative environments, such as nuclear reactors, nuclear medicine equipment or experiments of high energy physics.

The probability of SEB can be significantly reduced, biasing the device not to its maximum rated voltage (even with an efficiency worsening in terms of on-resistance). In fact, for a given radiative environment, SEB occurs only for drain-source voltages greater than a threshold value, which can change from device to device. To characterize this parameter, it is necessary to perform costly experimental tests. An interesting alternative could be represented by TCAD tools, provided you get a reasonable fit with the experimental data.

The research on neutron induced SEB was performed both experimentally and with TCAD simulations. Regarding the experimental activity, accelerated tests were performed with the moderated Am-Be source at the University of Palermo and the ANITA source at the The Svedberg Lab in Uppsala. In both cases, the experiments were carried out on commercial power MOSFET, manufactured by ST Microelectronics. The devices were subjected to an irradiation equivalent to 20 years of exposure to terrestrial neutrons at sea level, that is, the entire useful life of the photovoltaic panel, for different bias voltages. Weibull statistical analysis was also made to evaluate the Mean Time To Failure and the failure rate of the DUTs.

Subsequent investigations have been carried out with TCAD simulators. In particular, it has been proposed a new methodology for the estimation of the SEB threshold voltage and the derating factor. In fact, the current SEE simulation paradigm is based on specific models for heavy ions ionizing effects and subsequent transient analysis; however, some modifications are needed in order to use the same approach for neutron effects simulations.

Chapter 1

Neutron effects on power MOSFETs

Contents

In microelectronics, the success and market diffusion of a new technology mainly depends on its reliability, i.e. the ability to maintain their own operating specifications over the time. In this sense, a failure may be any kind of electrical parameter variation, outside the range specified by the manufacturer. Several factors affect the reliability of a device; the most common failure mechanisms fall in the following categories:

- material-interaction-induced mechanisms;
- stress-induced mechanisms
- mechanically induced failure mechanisms
- environmentally induced failure mechanisms.

The radiation induced failures belong to the environmental category. In principle, an electronic device exposed to radiation may experience two kind of degradations: cumulative effects, caused by prolonged exposure and absorption of radiation doses or SEEs, related to the interaction of a single energetic particle. Neutrons can lead both effects. Furthermore, for power devices, a single effect may result in a catastrophically damage.

SEEs involve a broad domain of physics such as natural radiation environment modeling, radiation mechanisms, ion energy depositions in semiconductors, charge transport and collection in elementary semiconductor devices such as PN junctions or elementary MOS transistors. In this chapter, neutron induced SEE will be over viewed, starting from the interaction of neutrons with matter and the ionization mechanisms to the description of a typical power MOSFET structure.

1.1 Terrestrial neutron environment

The main natural radiation background affecting silicon devices originates from cosmic rays. In outer space proton are most abundant, largely as part of the solar wind with energies into the MeV range. Cosmic rays also contain heavier ions, mainly iron. The earth atmosphere shields most of this radiation. However, when cosmic rays enter earth's atmosphere, they collide with atomic nuclei in air and create cascades of secondary particles: primarily neutrons, plus some protons and a few pions. The highest density of this secondary particles is reached at a height of about 18 km above ground (Pfotzer peak) and drops off to sea level at which the neutron flux is significant.

In general, the flux of neutrons varies with altitude (the atmosphere attenuates both the cosmic rays and the neutron flux), latitude (due to the variation of the earth's magnetic field shielding efficiency from equator to the poles), and to a lesser extent with longitude. The flux of neutrons can be modulated by solar activity and solar eruptions.

Recently, analytical models describing these variations have been presented in JESD89A standard. Measurements have been performed using different monitors or spectrometers. The energy spectrum is generally considered to be independent of altitude. It extends from thermal energies up to 10 GeV. In first approximation, the differential energy spectrum dn/dE can be considered to be proportional to $1/E$. This means that we get about the same number of neutrons in the energy range 1 MeV to 10 MeV, 10 MeV to 100 MeV and 100 MeV to 100 MeV. For $E > 1\,\mathrm{GeV}$, the slope dn/dE can be considered with a good approximation to be proportional to E^{-2}. More precisely, the neutron spectrum has three major peaks, thermal energy peak, evaporation peak around 1 MeV, and cascade peak around 100 MeV. The reference flux is taken at New York City at sea level to be $13\,\mathrm{cm}^{-1}\,\mathrm{s}^{-1}$ $E > 10\,\mathrm{MeV}$.

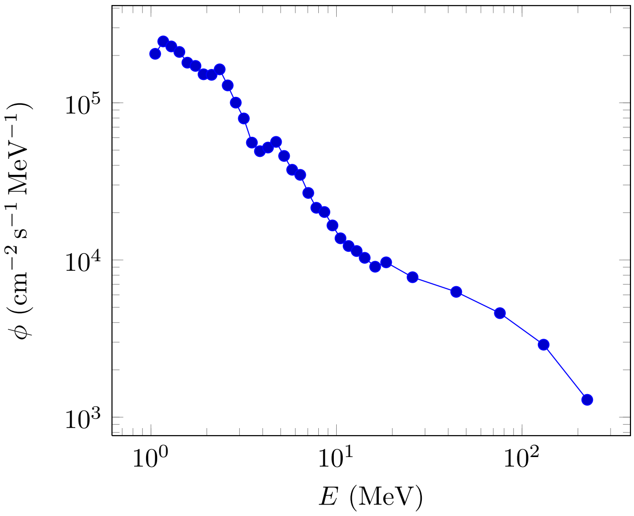

Figure 1.1: Terrestrial neutron spectrum, according JESD89A

1.2 Neutron interaction with matter

Neutrons are uncharged particles and hence can travel appreciable distance in matter without interacting. Like photons, neutrons do not interact with orbital electrons (i.e. there is no Coulomb's interaction, as for charged particles).

A simple notation can be used to give a concise indication of an interaction of interest. If a neutron n impinges on a target nucleus T, forming a resultant nucleus R and the release of an outgoing particle g, this is interaction is shown as $\mathrm{T(n,g)R}$. The heavy nuclei are shown outside the parentheses. To denote a type of interaction without regard for the nuclei involved, only the portion in parentheses is shown.

Neutrons can interact with atomic nucleus with several mechanisms depending on their energy. Despite the great variety, those mechanisms may be one of two major types: *scattering* or *absorption*. A third mechanism, occurring for very high neutron energies (more than 100 MeV) is the *spallation*.

1.2.1 Scattering process

When a neutron is scattered by a nucleus, its speed and direction change but the nucleus is left with the same number of proton and neutrons it had before the interaction. The nucleus will have some recoil velocity an it may be left in an excited state that will lead to the eventual release of radiation. Scattering events can be subdivided into *elastic* and *inelastic* scattering.

In *elastic* scattering, the recoil nucleus is identical to the target nucleus.

For this reason, this mechanism is indicated by the notation (n, n). In the collision, the total kinetic energy and the momentum of the neutron-target nucleus system are conserved. The energy lost by the neutron is transferred to the recoiling nucleus depending on the recoiled angle. The maximum energy that can be given to the recoil is:

$$E_{max} = 4E \cdot \frac{A}{(A+1)^2} \tag{1.1}$$

where A is the atomic number of the target nucleus.

Inelastic scattering is similar to elastic scattering except that the nucleus undergoes an internal rearrangement into an excited state from which it eventually releases radiation. More specifically, the incident neutron is absorbed in the target nucleus and a short time later a neutron is ejected with a lower energy, sharing a part of the total kinetic energy with the recoil target nucleus. This kind of interaction is indicated by the notation (n,ń)

1.2.2 Absorption process

Absorption interactions group all the processes that result in a fragmentation of the nucleus in two or more recoil fragments: e.g. nuclear reactions, fissions and so on. A further classification is made depending on the recoil type: *electromagnetic* absorption, if a γ ray is emitted; *charged* absorption for charged recoils as protons, deutons and α particles; *neutral* absorption if two or more neutron are emitted and *fission* if many recoils, both electromagnetic, charged or neutral are ejected.

Generally, the lighter recoil is indicated to describe the reaction: (n, p), (n, α), (n, d). The heavier element is obtained by the equilibrium of the number of neutrons and protons before and after the reaction. For example, with ^{28}Si (the most abundant silicon isotope), (n, p) reaction results in a proton and Al recoil; (n, p) reaction results in He and Mg recoils. The incident energy of the neutron diminished by the mass variation is shared between the secondary particles and the main recoil nucleus. These reactions, require that the incident neutron energy is larger than the threshold energy of the reaction, that is the *Q-value*, defined as:

$$Q = K_{final} - K_{initial} = (m_{initial} - m_{final})\, c^2 \tag{1.2}$$

where K_{final} and $K_{initial}$ are the products and reactants kinetic energies, m_{final} and $m_{initial}$ are the the products and reactants masses and c is the speed of light in vacuum. A reaction with a positive Q-value is exothermic, i.e. has a net release of energy, since the kinetic energy of the final state is greater than the kinetic energy of the initial state. A reaction with a negative Q-value is endothermic, i.e. requires a net energy input, since the kinetic energy of the final state is less than the kinetic energy of the initial state.

For a given neutron energy, different reactions are possible but their relative probability varies with the neutron energy.

1.2.3 The cross section concept

The probability of a particular event occurring between a neutron and a nucleus is expressed through the concept of the cross section. If a large number of neutrons of the same energy are directed into a thin layer of material, some may pass through with no interaction, others may have interactions that change their directions and energies, and still others may fail to emerge from the sample. There is a probability for each of these events. For example, the probability of a neutron not emerging from a sample (that is, of being absorbed or captured) is the ratio of the number of neutrons that do not emerge to the number originally incident on the layer. The cross section for being absorbed is the probability of neutrons being absorbed divided by the areal atom density (the number of target atoms per unit area of the layer). Thus the concept of cross section can be quantified physically in terms of characteristic area, where a larger area means a larger probability of interaction. The standard unit for measuring a cross section (denoted as σ) is the b, which is equal to 1×10^{-28} m or 1×10^{-24} cm.

Cross section can be measured for all possible interaction processes together, in which case they are called total cross section, or for specific processes, distinguishing elastic scattering and inelastic scattering; of the latter, the absorption cross sections are of particular interest.

1.3 Charged recoils: ionization and ranges

The basic physical picture of a SEE is that excess electron-hole pairs are generated by ionization mechanism in the silicon device. The field in the neighbourhood of the PN junction, if sufficiently strong, separates these electrons and holes before they recombine, and sweeps the excess carriers of the appropriate sign to a nearby device contact.

For heavy ions and charged particles, this mechanism is direct, because they lose their energy by Coulomb interaction with the electrons of the target atoms; on the contrary, neutrons do not have electrical charge, but can induce the emission of charged recoils, thus the ionization mechanism is indirect. Therefore, the picture described above can be applied for each charged recoil produced after the neutron interaction with the target.

The key parameters for the recoils track description are the stopping power, or energy loss per unit track length, which is a measure of the local energy exchange between the incoming particle and the electrons in the medium and the projected range. It is useful to convert the energy loss into ionization pairs per unit track length. For silicon, the conversion factor is 3.6 eV per electron-hole pair. An energy loss of $1\,\mathrm{MeV}\,\mu\mathrm{m}^{-1}$ in silicon is

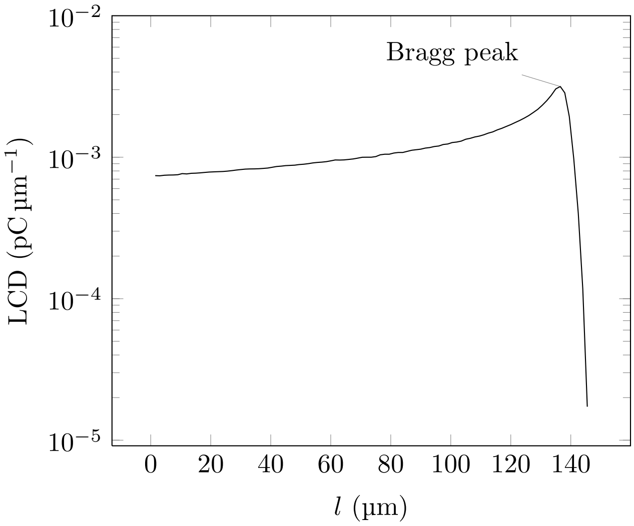

Figure 1.2: A typical Bragg curve

therefore associated with the generation of 2.8×10^5 electron-hole pairs per µm, which is equivalent to a local linear charge density of 44 fC µm^{-1}.

When the stopping power is plotted against particle penetration length, a so-called Bragg curve is obtained. This curve is flat and has small values at small path lengths, but it rises steeply and reaches a maximum value near the end of the particle range. Most of the kinetic energy of the particle is deposited into a narrow Bragg region which surrounds the peak of the ionization curve.

1.4 Power MOSFET basics

Before delving into the SEB mechanisms, the main concepts related to power MOSFETs will be briefly discussed, paying particular attention to the super-junction devices.

Several structures had been explored at the beginning of the 1980s, when the first power MOSFETs were introduced. However, most of them have been abandoned in favour of the Vertical Diffused MOS (VDMOS) structure. In fact, the classical planar structure of the MOSFET is not suitable for high power applications, because, in order to increase the maximum drain current, it is necessary to maximize the aspect ratio W/L, with a large width W and a channel length L kept as smallest as possible. Unfortunately, reducing the channel length in a planar MOSFET, a drastic breakdown voltage reduction occurs. In particular, the depletion region of the body-drain junction reaches the channel, resulting in a quite low breakdown voltage. In short, the current and breakdown voltage ratings are both functions of the channel dimensions.

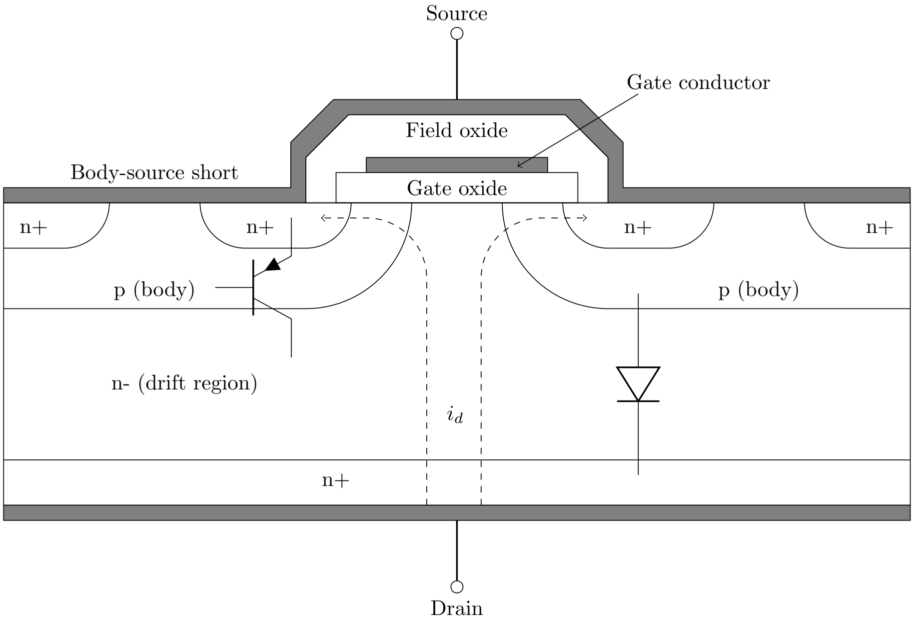

Figure 1.3: Power MOSFET structure

On the contrary, in a vertical structure, the voltage rating of the transistor is a function of the doping and thickness of the epitaxial layer, while the current rating is a function of the channel width. This makes possible for the transistor to sustain both high blocking voltage and high current within a compact piece of silicon.

Typical layers found in the VDMOS from top to bottom are the source metal layer, isolation oxide layer, poly-silicon gate layer, gate oxide layer, epitaxial layer, substrate layer and backside metal layer. The device is termed double-diffused because both the source and the body are diffused using the poly-silicon gate as a mask. A cross sectional view is showed in figure 1.3. It can be seen that the source electrode is placed over the drain, resulting in a current mainly vertical when the transistor is in the on-state. Current flow between the drain and source is turned on or turned off by modulating the surface conductivity in the p-body region under the poly-silicon gate (this conductivity surface region is referred to as the channel), which is controlled by the gate-source voltage.

For a fixed value of channel length L, the current handling capability of a power MOSFET is determined by its gate channel width W (the third or z-axis dimension of the picture in figure). In order to create a very wide channel, the power MOSFET is realized with many paralleled elementary cells. This layout technique allow to achieve the large currents required in the on state, while retaining the same channel length of the individual cell. Several shapes have been proposed for these cells, the most famous being the hexagonal shape from International Rectifier. Another way to increase the channel density is to reduce the size of the elementary structure. This allows for more cells in a given surface area, and therefore more channel width. However, as the cell size shrinks, it becomes more difficult to ensure proper contact of every cell. To overcome this, a strip layout is often used.

It is worth noting that power MOSFETs with lateral structure exist. They are mainly used in high-end audio amplifiers. Their advantage is a better behaviour in the saturated region than the vertical MOSFETs, which are specifically designed for switching applications.

1.4.1 Parasitic BJT issues

The power MOSFET vertical structure embed a parasitic BJT,: the body region of the MOSFET serves as the base of the BJT, the source as the BJT emitter and the drain as the BJT collector. The beta of this parasitic BJT may be significantly greater than 1 because the length of the body region where the channel of the MOSFET is formed is kept as short as possible to minimize the on-resistance.

The inadvertent turn on of the parasitic BJT can lead to permanent failures for 2 reasons:

1. a current flows between the source and drain contacts, without the gate control;
2. the BJT cannot be turned off via the base terminal because the base in is not accessible(latchup condition).

Furthermore, as we will see in the following sections, the parasitic BJT plays a key role into the SEB triggering.

From the foregoing, it is fundamental to prevent the BJT activation, keeping the potential of the parasitic base as close to the source potential as possible. This is the purpose of the body-source short. As a result, there is a parasitic diode connected between the drain and source of the MOSFET, which can be exploited as a free-wheeling diode in half-bridge and full-bridge converters.

dV/dt limitation

Although the body-source short is quite effective in preventing BJT turn on from a static point of view, it does not guarantee the turn on during fast switching transients. As showed into figure, the base of the parasitic BJT is connected to the drain terminal by the base resistance R_b and the drain-body capacitance C_{db}. A drain voltage variation dV/dt induce a displacement current i_d, given by:

$$i_d = C_{db}\frac{dV}{dt} \tag{1.3}$$

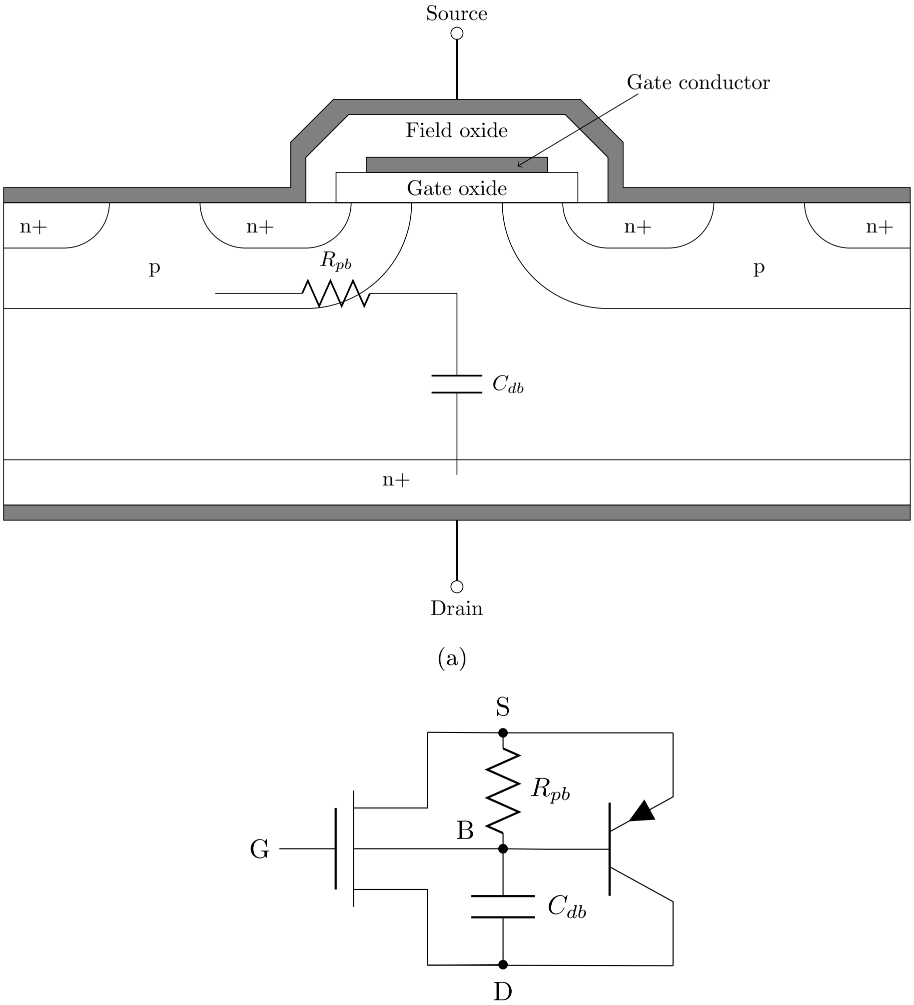

(a)

(b)

Figure 1.4: Parasitic BJT inside the power MOSFET structure

If the rate of rise of the drain voltage is very high, the displacement current may be large enough to induce a voltage drop along the base resistance higher than 0.7 V. Subsequently the parasitic BJT turns on. For a given device design and process technology, the base resistance and drain-body capacitance are fixed: therefore, this potential BJT turn on mechanism imposes a maximum rate of rise dV/dt.

Second breakdown

Power bipolar transistors may undergo a catastrophically failure mode, usually called *second breakdown*. The term *second* stressed the fact it does not depend on impact ionization and an attendant avalanche breakdown of a PN junction.

The second breakdown is triggered by non-uniform current density distribution over the entire device, evolving, due an elettro-thermal instability, into filamentary currents and hot points. Several intrinsic aspects of the transistor combine to give the BJT its susceptibility to second breakdown. First there is the general propensity of minority-carrier devices to thermal runaway when the voltage across them is held approximately constant as the device temperature increase. In fact, minority-carrier devices have a negative temperature coefficient of resistivity, because the minority-carrier densities are proportional to the intrinsic carrier density n_i, which increases exponentially with temperature with the following expression:

$$n_i = \sqrt{N_c N_v} \exp\left(-\frac{E_g}{2k_B T}\right) \tag{1.4}$$

where N_c and N_v are respectively the density of states of the conduction and valence bands, E_g is the energy band-gap, k_B is the Boltzmann's constant and T is the absolute temperature. This means the power dissipation will increase as the resistance drops as long as the voltage remain constant. A stability factor S can be defined:

$$S = R_{th} V_{ce} \frac{\partial I_c}{\partial T} \tag{1.5}$$

where R_{th} is the total thermal resistance of the device (i.e. from the junction to the case), V_{ce} is the applied collector voltage and $\partial I_c / \partial T$ is the partial derivative of the collector current with respect to temperature. The meaning of 1.5 is the following: the term $V_{ce} \cdot \partial I_c / \partial T$ is the variation of the electric power and, hence, the thermal power, with temperature at a fixed collector voltage, while the thermal resistance represents the rate of heat removal. If the rate of increase in power dissipation with temperature is higher than linear with temperature, i.e. $S > 1$, then an unstable situation will result and the temperature diverges, growing very quickly to unacceptably high values. This situation is a classic case of positive feedback in which the

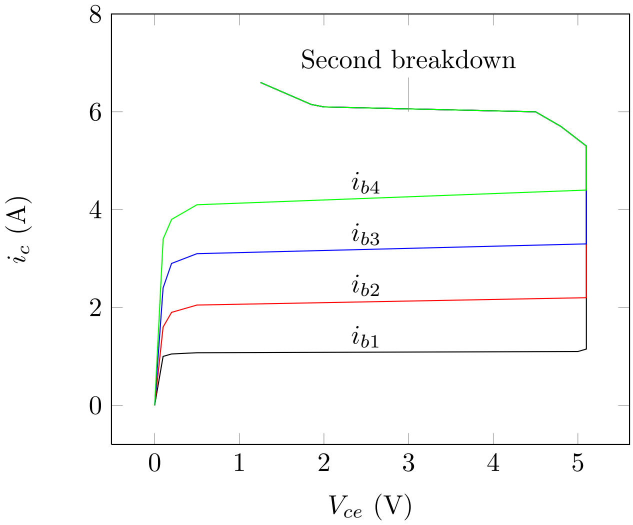

Figure 1.5: Second breakdown in the forward I/V characteristics of a power BJT

power dissipation leads to an increase in temperature, which leads to further increases in power dissipation, and so on, until the device destruction.

On the output characteristic, the second breakdown signature is a precipitous drop into the collector-emitter voltage at high collector currents.

1.4.2 Super-junction devices

When in the off state, the VDMOS is equivalent to a reverse biased PIN diode, constituted by the P+ body diffusion, the N- epitaxial layer and the N+ drain substrate. The light doping of the epitaxial layer, compared to the heavy doping of the body region, ensures that the depletion region of the junction does not extend far into the body toward source so that breakdown via reach-through is avoided. The blocking capability of the device relies on the thickness and doping of the epitaxial layer. In order to increase the blocking voltage, the doping must be simultaneously reduced and the layer thickness increased. However, when the VDMOS is in the on state, the epitaxial layer acts as a simple drift region: furthermore, as it is lightly doped, its intrinsic resistivity is non-negligible and heavily contributes to the overall on resistance. More precisely, for breakdown voltages greater than a few hundred volts, the drain drift region dominates the on state resistance. Experimental results indicate that the resistance of transistor increases disproportionately strongly as a function of its blocking capability:

$$R_{on} \propto {BV_{dss}}^{2.4 \ldots 2.6} \tag{1.6}$$

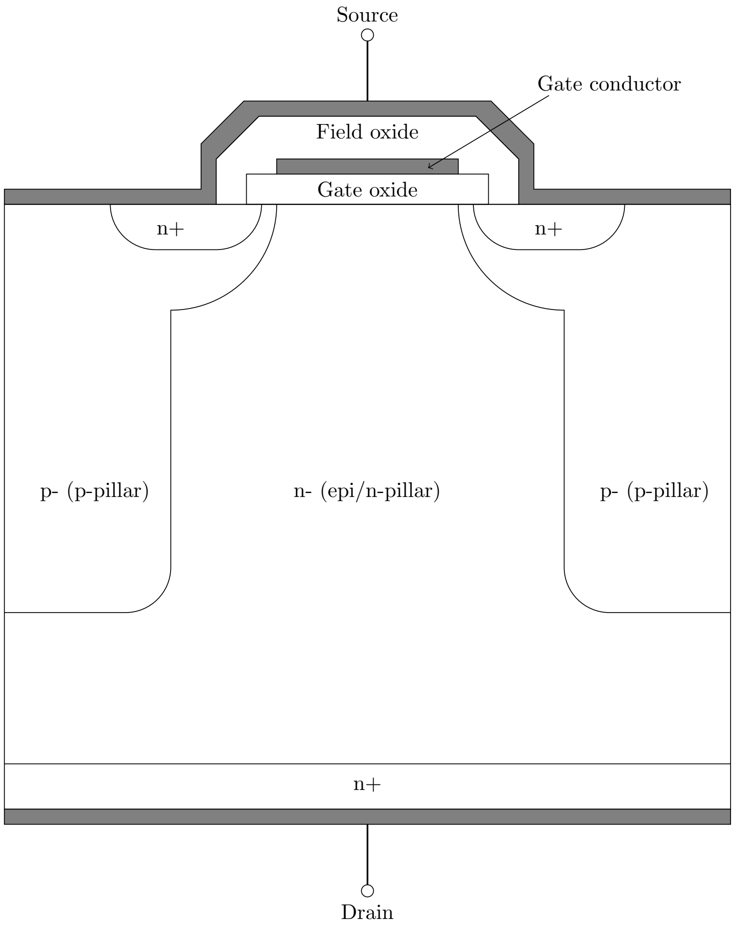

Figure 1.6: Super-junction device structure

This relation is also known as the 1D silicon limit. Super-junction devices were introduced to overcome this limitation: the more than square law dependence in the case of standard MOSFET has been broken and a linear voltage dependence achieved. This was accomplished, structuring the epi-layer into p-type and n-type pillars, as shown in figure. The p-type pillars are performed by multiple local p-type implantations followed by n epi-layer growth steps. As a result, a transverse PN junction is included. With positive drain-source voltages, this transverse junction is reverse biased, because the p-pillar is connected to the body-source region, while the n-pillar is connected to the drain. Consequently, the electric field profile in the drift region become bi-dimensional, varying appreciably not only along the vertical direction (from source to drain), but also in the horizontal one. The great advantage of this structure is that, if the pillars are completely depleted before the breakdown, the electric field profile is nearly flat, leading to a new dependency between BV_{dss} and R_{on} no longer quadratic, but linear. The change in the electric field profile is due to some sort of charge compensation: along the horizontal direction, the net charge is zero, therefore integrating the Poisson equation, we get a constant field equal to the value obtained in the proximity of the body-epi region. The n-type and p-type columns are depleted even at very low voltages.

1.5 SEB in power MOSFETs

SEB is a failure mode for power MOSFETs operating in switching mode and polarized in the off state (blocking a high drain-source voltage, with the body-drain junction reverse biased). Observation of this effects was first published in 1986 by a group of researchers from Aerospace Corp who reported on a destructive latched current effect in a number of different n-type power MOSFETs from several suppliers. In this study, the DUTs were exposed to the radiation field of a ^{252}Cf neutron source. Destructive failures were observed when the drain source bias exceeded about 50% of the maximum rating of the transistors. In the following years, many other studies have been carried out, especially for heavy ion induced failures, thanks the particular attention devoted by the aerospace community. For this reason, most of SEB models were developed for heavy ions and the conventional VDMOS structure; however, they are valid also for neutron induced failures and for different power MOSFET structures, such as super-junctions.

When the heavy-ion traverses different semiconductor layers, it sheds energy in accordance to its Linear Energy Transfer (LET) function for that material, creating a sheath of electron–hole pairs along its path. In the normal incident case, the heavy ion track covers one or two elementary cells at most: therefore, SEB is a highly localized phenomenon.

In the presence of the electric field within the depletion region, the

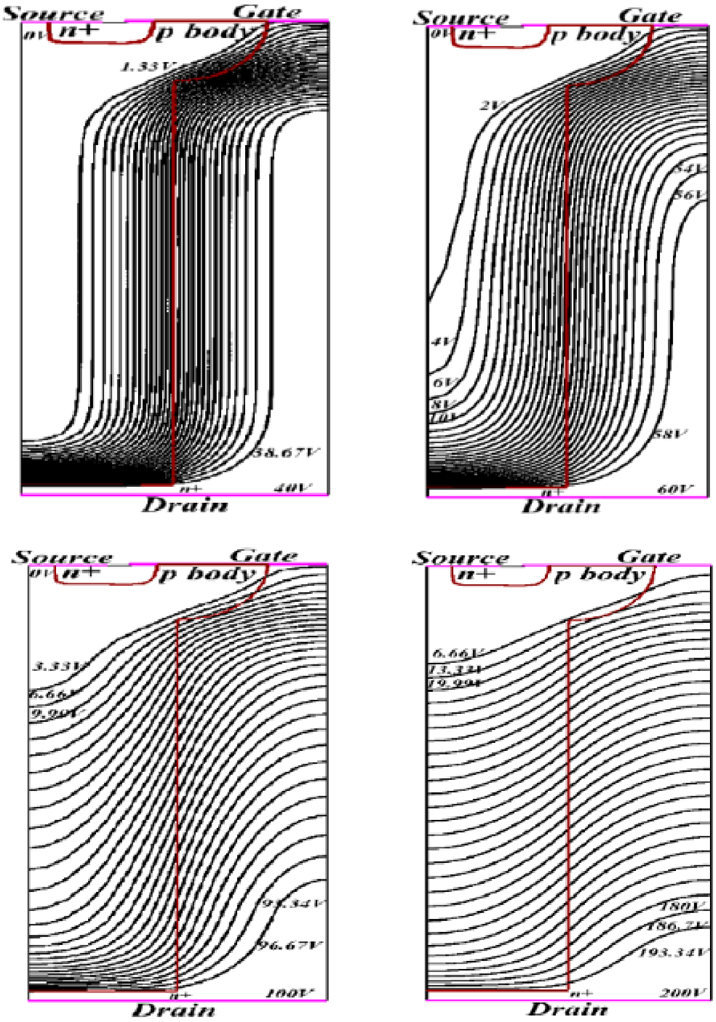

Figure 1.7: Bi-dimensional electric profile inside the drift region of a super-junction device

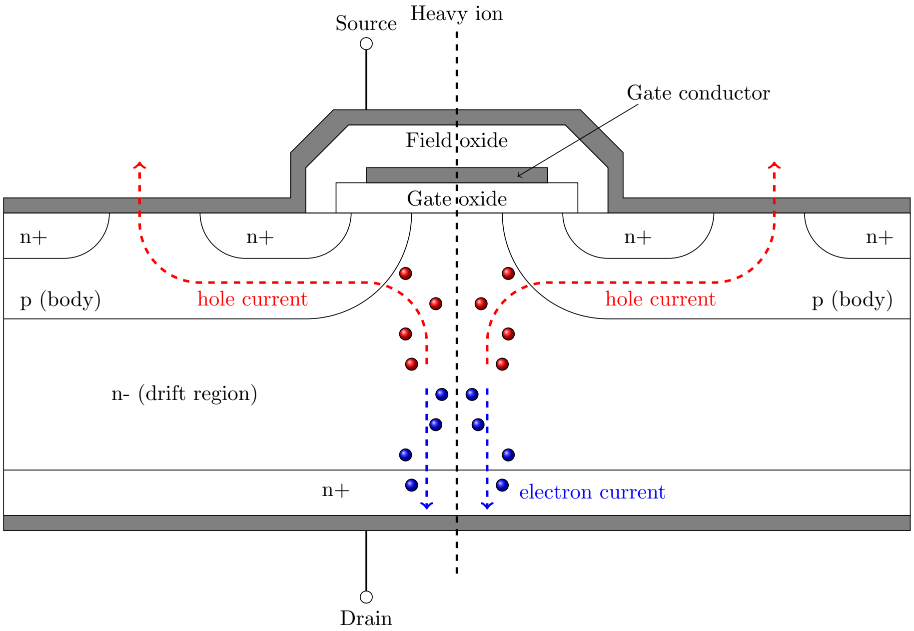

Figure 1.8: Pictorial representation of SEB

charges separate with electrons flowing to the drain region, while holes are swept into the p-body diffusion. Subsequently, a filamentary current flows between drain and source contacts. Moreover, this overall process is enhanced by avalanche multiplication. If the applied drain-source voltage is high enough and the heavy ions traverses the sensitive region of the device, a positive feedback or regenerative mechanism can be trigger, resulting in an uncontrolled drain current increase.

Two physical mechanisms are responsible for the self-maintenance of this positive feedback:

1. the parasitic BJT turn-on;
2. the current induced avalanche in the epitaxial region.

In fact, the hole current flows laterally across the p-body junction to exit the device. Current flow through the p-body region under the source region induces a voltage potential (due to the resistivity of the material in this region). If that voltage potential exceeds the built-in potential (approximately 0.7 V), the parasitic bipolar transistor that is inherent to the MOSFET structure turns on, allowing substantially higher currents to flow along this path, and the process becomes self-sustaining. A positive feedback is established because electrons are injected from emitter (source) into collector (epi-drain), new holes are generated by impact ionization and drifted toward the body-source enhancing the base current and the base-emitter

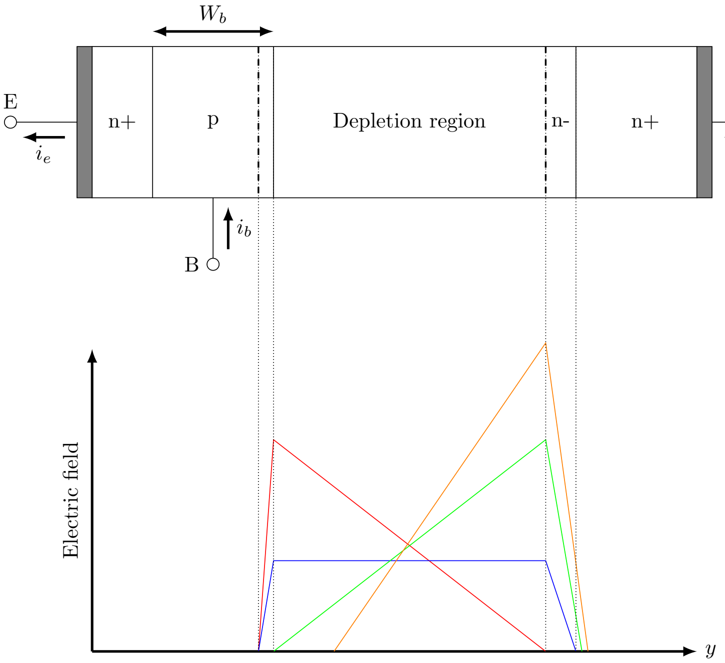

Figure 1.9: Electric field profile inversion under current induced avalanche conditions

voltage difference. The result is that the collector currents in the parasitic BJT increase to the point where thermal failure creates a permanent short between the source and drain, entering the MOSFET in second breakdown. It was also observed that regenerative feedback depends on the gain of the parasitic NPN transistor and the spreading resistance of the body region.

SEB can be triggered not only by the parasitic BJT turn-on: in fact, similar phenomena have been observed also in the power diodes, which have no parasitic bipolar structures such as the vertical power MOSFET. In blocking state, the body-epi junction is reverse polarized, resulting in a triangular profile of the electric field as a function of depth. This can easily be demonstrated by integrating the Poisson equation in the space charge region $0 < y < W_{drift}$ (which extends almost entirely in the weakly doped n-type drift region):

$$\frac{dE(y)}{dy} = -q\frac{N_D}{\epsilon} \tag{1.7}$$

where N_D is the n-dopant density and ϵ is the silicon dielectric constant. The field peak is at body-epi junction ($y = 0$). The previous equation is valid in full depletion conditions, i.e. the mobile charge concentration is negligible compared to the fixed charge associated with the ionized impurities N_D. However, the heavy ion may generate a non-negligible electrons current in the epitaxial region, therefore the Poisson equation becomes:

$$\frac{dE(y)}{dy} = -q\frac{(N_D - n)}{\epsilon} \tag{1.8}$$

Given the high magnitude electric fields, the electrons reach their saturation velocity v_{sat} and n can be expressed as:

$$n = \frac{j}{qv_{sat}} \tag{1.9}$$

where j is the electron current density. From 1.9, j (and hence n) increments result in the modulation of the electric field profile, whose integral against depth must remain constant and equal to the drain-source voltage. In particular:

- the slope assumes an opposite sign (the electric field increases with depth);
- the peak value shifts towards the epi/drain junction. Here it can overcome the silicon dielectric rupture value and locally avalanche breakdown occurs.

Obviously the resulting combination of high currents and high voltages determines power dissipation and therefore thermal damage. In power MOSFETs this mechanism can be exacerbated by parasitic BJT activation.

1.5.1 Temperature dependence

Increased temperature reduces susceptibility to SEB, through its effect on impact ionization in the body-epi space charge region. Impact ionization rate decreases with increasing temperature, causing a reduced hole current flow into the base region of the parasitic BJT and a lower base emitter voltage at the source region

1.5.2 Channel conductivity effects

Experimental data continue to show that p-channel MOSFETs are less susceptible to the SEB when compared with their equivalent n-channel counterparts. One reason that p-channel MOSFETs are less susceptible to SEB is that holes have a lower impact ionization coefficient than electrons. Furthermore, the p-channel devices are fabricated with n-type bodies which are characterized by a lower resistance. Therefore, p-channel devices require higher ion-induced current flow to turn on the parasitic bipolar transistor. Finally, the PNP parasitic BJT has a lower emitter efficiency. Although they are more resilient to SEB, pMOSFET are less attractive with respect nMOSFET in terms of on-resistance.

1.6 SEGR

SEGR is often observed simultaneously with SEB, because the localized melting in the MOSFET will often damage the gate, so a resulting leakage path from the gate to the source and/or drain may result.

SEGR is caused by heavy ion strike in the neck region (a region located in the silicon layer below the gate oxide between two adjacent P-body well) of the power MOSFET. In the presence of a gate potential the field across the gate oxide can be large but not as large to cause the insulator failure. It is understood and accepted that the total electric field causing SEGR in power MOSFET is coming from two sources. The first is the steady state electric field due to the applied gate and drain biases. The second is the transient electric field due to electrons and holes redistribution after a heavy ion strike. When a heavy ion hits the MOSFET's neck region, the charge deposited by the ion are separated, the holes migrates towards the Si-SiO_2 interface and the electrons towards the n-doped substrate. The movements of these yielded carriers produce voltage drop that locally weaken the space-charge region between the n-epitaxial layer and the p-diffusions. This involves in a dangerous drop of the drain-source voltage on the gate oxide increasing its electrical field, which can exceed the critical value and lead to a localized gate rupture. Once the rupture is initiated, current flows through the gate oxide to the poly results in a thermal runaway condition, locally melting the silicon, dielectric and poly.

Bibliography chapter 1

[1] P.C. Adell and L.Z. Scheick. "Radiation Effects in Power Systems: A Review". In: *Nuclear Science, IEEE Transactions on* 60.3 (June 2013), pp. 1929–1952. ISSN: 0018-9499. DOI: `10.1109/TNS.2013.2262235`.

[2] M. Allenspach et al. "SEGR and SEB in n-channel power MOSFETs". In: *Nuclear Science, IEEE Transactions on* 43.6 (Dec. 1996), pp. 2927–2931. ISSN: 0018-9499. DOI: `10.1109/23.556887`.

[3] M. Allenspach et al. "Single-event gate-rupture in power MOSFETs: prediction of breakdown biases and evaluation of oxide thickness dependence". In: *Nuclear Science, IEEE Transactions on* 42.6 (Dec. 1995), pp. 1922–1927. ISSN: 0018-9499. DOI: `10.1109/23.489234`.

[4] B.J. Baliga. *Advanced power MOSFET concepts.* Ed. by Springer Science. 2010.

[5] B.J. Baliga. *Fundamentals of power semiconductor devices.* Ed. by Springer Science. 2008.

[6] J.R. Brews et al. “A conceptual model of a single-event gate-rupture in power MOSFETs”. In: *Nuclear Science, IEEE Transactions on* 40.6 (Dec. 1993), pp. 1959–1966. ISSN: 0018-9499. DOI: `10.1109/23.273457`.

[7] T. Fujihira. “Theory of semiconductor superjunction devices”. In: *Japanese Journal of Applied Physics* 36.1 (Oct. 1997), 6254–6262.

[8] R. Gailard. “Single event effects: mechanism and classification”. In: *Soft Errors in Modern Electronic Systems.* Springer, 2010.

[9] Jakob H. Hohl and K.F. Galloway. “Analytical Model for Single Event Burnout of Power MOSFETs”. In: *Nuclear Science, IEEE Transactions on* 34.6 (Dec. 1987), pp. 1275–1280. ISSN: 0018-9499. DOI: `10.1109/TNS.1987.4337465`.

[10] Jakob H. Hohl and G.H. Johnnson. “Features of the triggering mechanism for single event burnout of power MOSFETs”. In: *Nuclear Science, IEEE Transactions on* 36.6 (Dec. 1989), pp. 2260–2266. ISSN: 0018-9499. DOI: `10.1109/23.45433`.

[11] S. Huang, G.A.J. Amaratunga, and F. Udrea. “Analysis of SEB and SEGR in super-junction MOSFETs”. In: *Nuclear Science, IEEE Transactions on* 47.6 (Dec. 2000), pp. 2640–2647. ISSN: 0018-9499. DOI: `10.1109/23.903820`.

[12] F. Iannuzzo, C. Abbate, and G. Busatto. “Instabilities in Silicon Power Devices: A Review of Failure Mechanisms in Modern Power Devices”. In: *Industrial Electronics Magazine, IEEE* 8.3 (Sept. 2014), pp. 28–39. ISSN: 1932-4529. DOI: `10.1109/MIE.2014.2305758`.

[13] *JESD89A: Measurement and reporting of alpha particle and terrestrial cosmic ray induced soft errors in semiconductor device.* Standard Rev. A. JEDEC Solid State Technology Association, 2006.

[14] G.H. Johnson et al. “A review of the techniques used for modeling single-event effects in power MOSFETs”. In: *Nuclear Science, IEEE Transactions on* 43.2 (Apr. 1996), pp. 546–560. ISSN: 0018-9499. DOI: `10.1109/23.490900`.

[15] G.H. Johnson et al. “Analysis of the time-dependent turn-on mechanism for single-event burnout of n-channel power MOSFETs”. In: *Radiation and its Effects on Components and Systems, 1993.,RADECS 93., Second European Conference on.* Sept. 1993, pp. 441–445. DOI: `10.1109/RADECS.1993.316562`.

[16] G.H. Johnson et al. “Temperature dependence of single-event burnout in n-channel power MOSFETs [for space application]”. In: *Nuclear Science, IEEE Transactions on* 39.6 (Dec. 1992), pp. 1605–1612. ISSN: 0018-9499. DOI: `10.1109/23.211342`.

[17] P.N. Kondekar, H.S. Oh, and Y.B. Kim. “Study of the Degradation of the Breakdown Voltage of a Super-Junction Power MOSFET due to Charge Imbalance”. In: *Journal of the Korean Physical Society* 48.4 (Apr. 2006), 624–630.

[18] J.L. Leray. “Effects of atmospheric neutrons on devices, at sea level and in avionics embedded systems”. In: *Microelectronics Reliability* 47.9–11 (2007). 18th European Symposium on Reliability of Electron Devices, Failure Physics and Analysis, pp. 1827–1835. ISSN: 0026-2714. DOI: `http://dx.doi.org/10.1016/j.microrel.2007.07.101`. URL: `http://www.sciencedirect.com/science/article/pii/S0026271407003666`.

[19] S. Liu, J.L. Titus, and M. Boden. “Effect of Buffer Layer on Single-Event Burnout of Power DMOSFETs”. In: *Nuclear Science, IEEE Transactions on* 54.6 (Dec. 2007), pp. 2554–2560. ISSN: 0018-9499. DOI: `10.1109/TNS.2007.910869`.

[20] L. Lorenz et al. “COOLMOSTM-a new milestone in high voltage power MOS”. In: *Power Semiconductor Devices and ICs, 1999. ISPSD ’99. Proceedings., The 11th International Symposium on.* 1999, pp. 3–10. DOI: `10.1109/ISPSD.1999.764028`.

[21] N Mohan, T.M Undeland, and W.P. Robbins. *Power electronics: converters, application and design.* Ed. by John Wiley and Sons Inc. 2002.

[22] P. Rinard. “Neutron interaction with matter”. In: *Passive nondestructive assay of nuclear materials.* ISBN 0-16-032724-5, 1991.

[23] F.W. Sexton. “Destructive single-event effects in semiconductor devices and ICs”. In: *Nuclear Science, IEEE Transactions on* 50.3 (June 2003), pp. 603–621. ISSN: 0018-9499. DOI: `10.1109/TNS.2003.813137`.

[24] Prabjit Singh. “Power MOSFET failure mechanisms”. In: *Telecommunications Energy Conference, 2004. INTELEC 2004. 26th Annual International.* Sept. 2004, pp. 499–502. DOI: `10.1109/INTLEC.2004.1401515`.

[25] H.H.K. Tang. “Nuclear physics of cosmic ray interaction with semiconductor materials: Particle-induced soft errors from a physicist’s perspective”. In: *IBM Journal of Research and Development* 40.1 (Jan. 1996), pp. 91–108. ISSN: 0018-8646. DOI: `10.1147/rd.401.0091`.

[26] J.L. Titus. “An Updated Perspective of single event gate rupture and single event burnout in Power MOSFETs”. In: *Nuclear Science, IEEE Transactions on* 60.3 (June 2013), pp. 1912–1928. ISSN: 0018-9499. DOI: `10.1109/TNS.2013.2252194`.

[27] P. Voss. *Radiation effects in silicon.* URL: `http://www.mupvoss.de/Strahlung/RadEffInSi.html`.

[28] Han Wang, E. Napoli, and F. Udrea. “Breakdown Voltage for Superjunction Power Devices With Charge Imbalance: An Analytical Model Valid for Both Punch Through and Non Punch Through Devices”. In: *Electron Devices, IEEE Transactions on* 56.12 (Dec. 2009), pp. 3175–3183. ISSN: 0018-9383. DOI: `10.1109/TED.2009.2032595`.

[29] T.F. Wrobel and D.E. Beutler. “Solutions to heavy ion induced avalanche burnout in power devices”. In: *Nuclear Science, IEEE Transactions on* 39.6 (Dec. 1992), pp. 1636–1641. ISSN: 0018-9499. DOI: `10.1109/23.211346`.

[30] T.F. Wrobel et al. “Current Induced Avalanche in Epitaxial Structures”. In: *Nuclear Science, IEEE Transactions on* 32.6 (Dec. 1985), pp. 3991–3995. ISSN: 0018-9499. DOI: `10.1109/TNS.1985.4334056`.

[31] J.F. Ziegler. “Terrestrial cosmic rays”. In: *IBM Journal of Research and Development* 40.1 (Jan. 1996), pp. 19–39. ISSN: 0018-8646. DOI: `10.1147/rd.401.0019`.

Chapter 2

SEB measurement

Contents

In this chapter, all the experimental aspects regarding SEB measurements will be discussed. After defining some basic parameters for particle beam characterization, we will overview the abundant literature on SEB measurement techniques and some of the currently used standard for devices qualification, such as the MIL 750 E and the JESD89A. This will help us to better illustrate our experimental approach. The remaining part of this chapter is devoted to our experimental apparatus description, with all the design considerations, from the capacitor and DUT boards to the virtual instrument programming. This is preceded by a section about the neutron facilities that we used for our experiments. Finally, some reliability and Weibull analysis concepts will be introduced.

2.1 Beam characterization

A particle beam can be characterized by some average quantities, such as the flux, fluence and spectrum.

The *flux* is the amount of radiation crossing a surface per unit of time. It can be expressed in several ways:

- the *integral* flux is the number of particles per unit area per unit time ($\mathrm{cm^{-2}\,s^{-1}}$), above a certain energy threshold;
- the *differential* flux is differential with respect to the energy and is the number of particles per unit area, per unit time, per unit energy ($\mathrm{cm^{-2}\,s^{-1}\,MeV^{-1}}$);
- the *differential* flux is differential with respect to the solid angle and is the number of particles per unit area, per unit time, per steradian ($\mathrm{cm^{-2}\,s^{-1}\,sr^{-1}}$), above a certain energy threshold.

In some cases, fluxes are also treated as differential with respect to the LET.

The *fluence* is the time integral of flux, so it is equal to the total number of particle that impinge upon a unit surface area and is normally given in units of $\mathrm{cm^{-2}}$.

The *spectrum* is the flux distribution over the particles average energy.

2.2 Standard references

2.2.1 MIL 750 E, method 1080

SEEs on the power devices are very different from those affecting the digital circuits and require specific measurement techniques. The unique standard that specifically establishes procedures for characterization and verification of discrete power MOSFETs for SEB and SEGR is the STD MIL 750 E, method 1080. Despite being oriented to heavy ion irradiation, this test method may be applicable in principle to testing where neutrons, protons, or other light particles are used.

Two test typologies are addressed: *verification* and *characterization.*

Verification testing requires the irradiation of the DUT to specified test conditions (e.g. gate bias, drain bias, neutron energy, flux or fluence). Verification testing is useful for hardness assurance and qualification testing of discrete power MOSFETs to determine their suitability at the specified test conditions. These tests use a pass/don't pass criterion and can be destructive. For destructive testing method and related issues see section 2.3.1

Characterization testing is performed when the DUT susceptibility under different test conditions need to be investigated. In contrast to the verification tests where the output information is essentially binary (DUT failed or not failed), the characterization tests provide cross sections and threshold curves. SEB and SEGR cross sections represent the total area of the sample sensitive to the these phenomena, independently on how such area is distributed on the sample. They are expressed in cm^2 and calculated as:

- the ratio between the number of events N and the total fluence φ_{tot} of the run, for SEB :
$$\sigma_{SEB} = \frac{N}{\varphi_{tot}}$$
- the reciprocal of the fluence φ for which the first event is detected, for SEGR:
$$\sigma_{SEGR} = \frac{1}{\varphi}$$

Cross sections are usually expressed in function of the applied bias or the particle LET (especially for heavy ion irradiation) . In any case, being SEB and SEGR threshold events, they are characterized by an ideal step trend, as depicted in figure 2.1. They have a negligible value (no sensitivity) for LET or bias lower the threshold values and rise suddenly at a constant value of saturation(maximum sensitivity) in correspondence of the threshold LET or bias. Actually, they usually:

- grow with a finite slope in the threshold region to reach a knee region;
- Increase with a gradual approach to the asymptotic value of the cross section of saturation.

This is mainly due to statistical variations of the charge collection and the volume of the sensitive region where the charge is collected.

SEB-SEGR threshold curves are usually plotted in V_{ds}-V_{gs} graphs and represent the limit conditions in terms of bias, for a given particle o spectrum, to have failures. An example of threshold curves is depicted in figure 2.2. These curves are useful for system designers to understand how much the maximum rated voltages of their devices should be lowered to operate in safety conditions.

According to the required accuracy, both the cross sections and the threshold curves consist of multiple experimental points. Each of them involves one or more exposures. Therefore characterization tests require more samples than verification tests, because many operating conditions need to be tested. For this reason, circumvention techniques (see section 2.3.2), i.e. non destructive test circuits, are adopted.

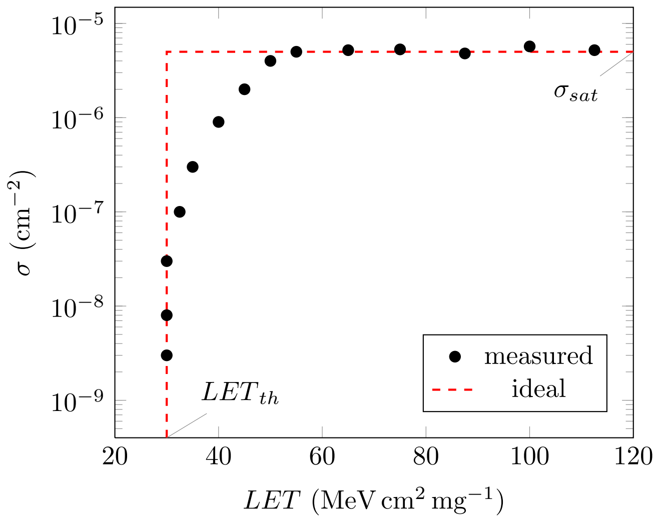

Figure 2.1: Typical trend of SEB/SEGR cross section

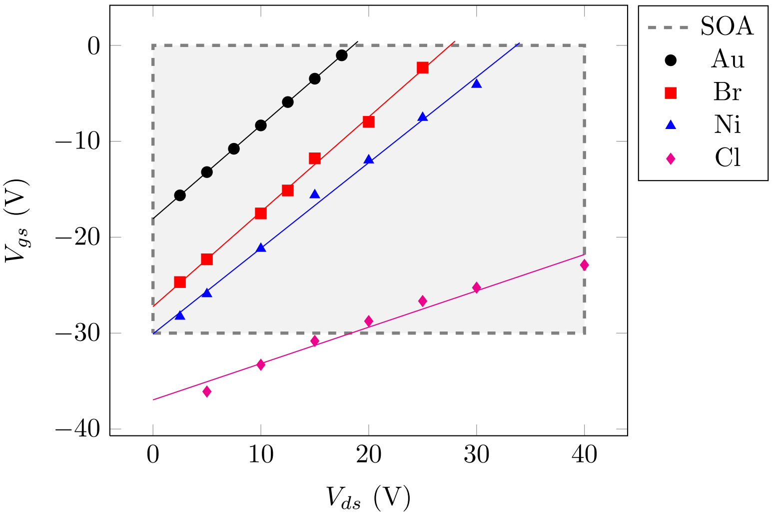

Figure 2.2: SEB/SEGR threshold curves. The grey box represents the SOA of the device; the really dangerous points are those inside the SOA

2.2.2 JESD89A

This specification defines the standard requirements and procedures for terrestrial Soft Error Rate (SER) testing of integrated circuits and reporting of results. We want to mention this standard, despite it concerns about the SEE on memories and digital circuits, because it makes explicit reference to the effects induced by terrestrial radiative environment. Therefore, we will highlight the aspects related to radiation sources, rather than general methodologies, which are very different from those of SEB and SEGR.

There are two fundamental methods to determine a product's SER. One is to test a large number of actual production devices for a long enough period of time (weeks or months) until enough soft errors have been accumulated to give a reasonably confident estimate of the SER. This is generally referred to as a *real-time* or un-accelerated SER testing. Real-time testing has the advantage of being a direct measurement of the actual product SER requiring no intense radiation sources, extrapolations to use conditions, etc. However, real-time testing does require an expensive system capable of monitoring hundreds or thousands of devices in parallel, for long periods of time. For SEB/SEGR testing this approach is more difficult because many exposures need to be performed [8], changing the bias voltage, while for memories the bias is fixed to the worst case condition, separately evaluated.

The other method commonly employed to allow more rapid SER estimations and to clarify the source of errors is Accelerated Soft Error Rate (ASER) testing. In ASER testing, devices are exposed to a specific radiation source whose intensity is much higher than the ambient levels of radiation the device would normally encounter. ASER allows useful data to be obtained in a fraction of the time required by un-accelerated real-time testing. Only a few units are needed and complete evaluations can often be done in a few hours or days instead of weeks or months. The disadvantages of ASER are that the results must be extrapolated to use conditions and that several different radiation sources must be used. In particular, three radiation components are identified and specifically addressed by the JESD89A standard: alpha particle radiation (for taking into account radio-isotopic impurities effects in the package and chip materials), low or thermal neutrons and high energy neutrons (for secondary cosmic rays effects).

An overall assessment of a device's SER is complete, only when an un-accelerated test is done under actual use conditions, or accelerated SER data for the alpha-particle component, the high-energy cosmic-radiation component, and if necessary, the thermal neutron component has been obtained and extrapolated to the use conditions. Now we will focus on neutrons.

Low energy neutrons accelerated testing

Testing for chip SER due to thermal neutrons can be done using a wide variety of sources. Thermal neutrons are available from both nuclear reactors and particle accelerators. Particle accelerator facilities use nuclear reactions such as energetic protons on Li targets to produce neutrons. These neutrons are then moderated (lowered in energy) by passing the neutrons through low-Z materials like polyethylene. 14 MeV neutron generators may also be used to produce thermal neutrons, again by using a moderating material to slow down the higher energy neutrons.

High energy neutrons accelerated testing

To simulate how the atmospheric neutrons induce single event upsets in microelectronic components at a highly accelerated rate, high energy particle beams may be used. Three different types of facilities are recommended which provide such high energy particle beams:

1. spallation neutron source;
2. mono energetic (or quasi-mono energetic) neutron source;
3. mono energetic (or quasi-mono energetic) proton source.

Spallation neutron sources provide neutrons over a wide range of energies, with the shape of the spectrum being similar to that of the terrestrial neutron environment. A spallation neutron source, such as the ICE House (formerly known as the Weapons Neutron Research, WNR) facility at the Los Alamos Neutron Science Center (LANSCE) or the TRIUMF Neutron Facility allows one to measure the Single Event Upset (SEU) rate and derive an averaged SEU cross section. Because the neutrons produced from a spallation source cover a wide energy spectrum, the user cannot extract a SEU cross section at a specific energy from such measurements, but rather obtains the contribution of SEU events from neutrons of all energies within the spectrum. When testing with a spallation neutron source, the SEU recorded will be due primarily to the high energy (e.g. greater than 10 MeV) neutrons. The SEU contribution of the neutrons in the energy range comprised between 1 and 10 MeV is less than 10%, but these neutrons comprise about the 40% of all neutrons having energies higher than 1 MeV in the terrestrial spectrum. With measurements using spallation neutrons, one can derive an averaged neutron SEU cross section which can be defined as:

$$\langle \sigma_{SEU} \rangle = \frac{N_{SEU}}{\phi_{spec}} \tag{2.1}$$

where N_{SEU} is the number of SEU and ϕ_{spec} is the fluence of neutrons over the spectrum from energies greater than 10 MeV.

In order to assess the SEU cross section value at a specific energy E, mono energetic facility can be used. Mono energetic neutron beams are to be distinguished from quasi-mono energetic neutron beams. There are three main types of truly mono energetic neutron beams with energies greater than 1 MeV in which almost all of the neutrons are within ±1 MeV of the peak energy. All are produced by accelerating a charged particle into a tritium (T) or deuterium (D) target. D-T reactions produce neutrons of 14 MeV, and this is the most common type of neutron generator. D-D reactions produce neutrons 3 MeV to 5 MeV, depending on the energy of the deuteron, and p-T reactions produce neutrons with energies depending on the energy of the proton. Neutron SEU cross sections can be defined as:

$$\sigma_{SEU}(E_n) = \frac{N_{SEU}}{\phi} \tag{2.2}$$

where E_n is the neutron energy. Neutron-induced SEU cross sections can also be measured using a quasi-mono energetic neutron beam. This beam differs from a truly mono energetic neutron beam in that a significant fraction of the neutrons are at energies less than the peak energy. The standard beam of this kind is obtained by accelerating mono energetic protons into a lithium target, although other production mechanisms are also possible. The neutrons from this beam comprise a two part distribution: the neutrons at the peak energy E_n, which is about 1 MeV to 2 MeV below the proton energy E_p, and the neutrons within the so-called low energy tail, from $E_n - 2$ MeV down to zero. Thus, the tail may contain neutrons spread out over more than 100 MeV, and the challenge in using this type of source is to separate out the SEU contribution of the neutrons in the low energy tail from those at the energy peak. The number of error events measured with a quasi-mono energetic facility need to be adjusted to account for upsets only from the neutrons at peak energy.

Having similar interaction mechanisms for energies higher than approximately 50 MeV, protons can be used as well as neutron for SEU cross-section measurements.

2.3 Literature overview

2.3.1 Basic destructive circuitry

SEB and SEGR experiments are inherently expensive to perform because of the catastrophic nature of the failure mechanisms. Therefore, they require a large number of samples to represent a meaningful statistics. During irradiation, the power MOSFET?s are biased in the off state with a large drain-source bias applied. In SEB measurements, the gate and source contacts are typically shorted together. In SEGR measurements, the gate bias polarizes the MOS structure in accumulation mode to achieve a pre-strike

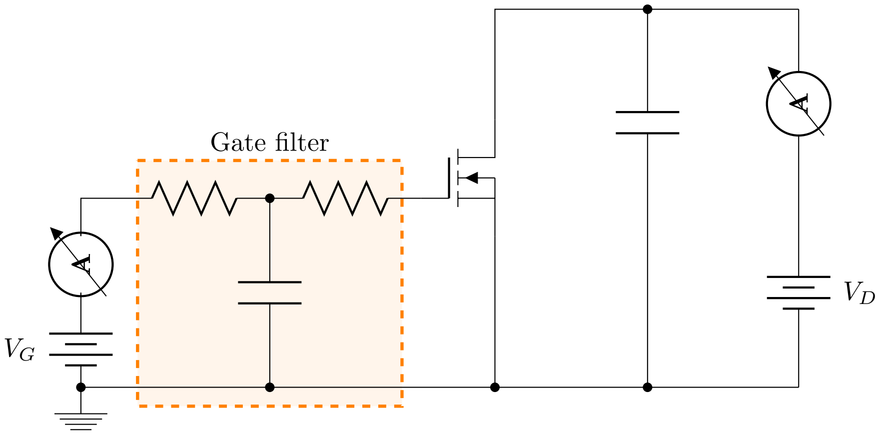

Figure 2.3: Basic destructive SEB test circuit

independence of the oxide field from the drain to source bias. For the n-channel power MOSFET?s, the gate is biased negatively with respect to the source. For only SEB measurements, gate and source contacts are connected to ground.

In both types of measurements, the drain-source current is monitored during irradiation; in SEGR measurements, the gate-source current is also monitored. Alternatively, SEB could be detected by monitoring the drain-source voltage. In fact, parasitic BJT turn on drives the DUT into secondary breakdown mode, with a resulting drain-source short.

The devices are irradiated until a pre-specified neutron fluence is obtained. If SEB or SEGR has not occurred after the specified ion fluence, the bias conditions are increased and another exposure is performed.

Figure 2.3 presents an example of a basic test circuit for SEB and SEGR, as in STD MIL 750 E. The gate resistor-capacitor-resistor network provides a simple gate transient filter to help suppress external voltage transients from damaging the gate oxide due to circuit over stresses. The drain-to-source capacitors are inserted to ensure sufficient charge is available at the DUT and minimize parasitic circuit effects (e.g. resistance and inductance of power cables between the DUT and the power supply).

SEB signature

One important aspect of performing neutrons and evaluating the MOSFET?s SEE performance is properly identifying the failure mechanism. SEB causes some common failure characteristics that help identify it as the failure mode. Four common SEB failure characteristics are as follows [32]:

1. the SEB failure threshold voltage should be independent of the off-state gate bias;

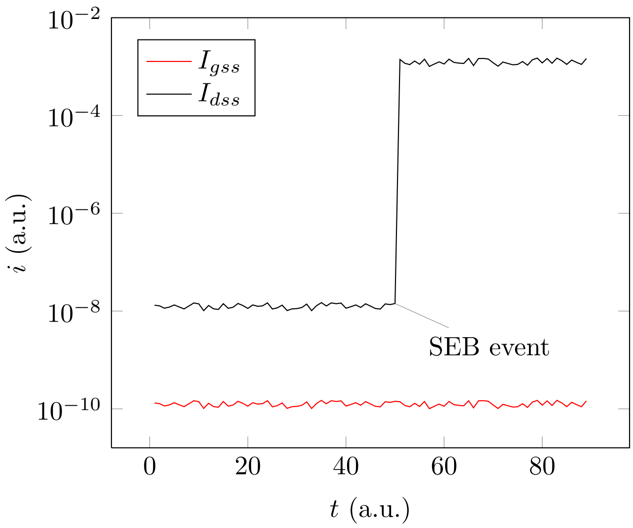

Figure 2.4: Typical drain and gate current trends during a SEB event

2. SEB failures should cause visible discolouration and/or die surface damage;
3. SEB failures should cause a resistive short between the drain and source nodes (the gate node may or may not be damaged after SEB);
4. the SEB is sensitive to circuit impedance in the drain and source nodes (resistance and inductance)

Figure 2.4 is a pictorial example of typical drain and gate current responses during heavy-ion irradiation before and after SEB. Before SEB event, the drain and gate currents are at the same levels of the leakage currents I_{dss} and I_{gss}, respectively. The recorded drain and gate leakage currents depend strongly upon the device's leakage characteristic, parasitic leakages caused by the test setup, and the measurement capability of the test system. When the SEB occurs, the drain current exhibits a significant increase, but the gate current remains relatively constant. This type of drain and gate current signature represents a classic example when SEB occurs in the device during neutron exposure.

Figure 2.5 is an example of a device before SEB depicting no signs of damage and after SEB depicting discolouration and visible die damage. After a failure occurs, the die surface should be examined to identify any signs of discolouration or die damage. Visible signs of surface damage are good indicators that SEB occurred. The amount of visible die damage depends on the available stored energy from the test circuit as well as from the actual device itself. SEB damage can be extremely isolated to a small area or cover a large area.

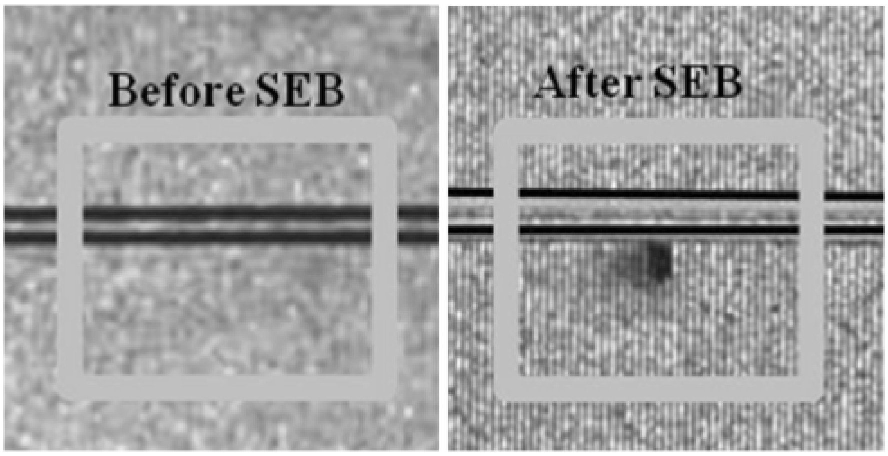

Figure 2.5: Microscopic view of the active area of a power MOSFET before (on the left) and after (on the right) a SEB

2.3.2 Circumvention techniques

Non destructive techniques are often used in SEB measurements. This significantly reduces the number of devices needed for an adequate sample size. A resistor is inserted between the drain and the power supply (see figure 2.6) that limits the maximum drain-source current and prevents the high current levels that trigger second breakdown of the parasitic BJT. The higher the transient current, the higher the voltage drop across the load resistor, which in turn reduces the voltage bias on the device. If the voltage drop across the load resistor is sufficient to reduce the voltage on the device to below the SEB failure voltage, the device would be protected from fatal burnout. Therefore this technique actuates a current limiting.

A counter is used to track the number of current pulses. The sensitive cross section of the device is obtained by dividing the number of pulses by the total ion fluence.

A current viewing-probe (e.g. resistor or current transformer) can be used to capture SEB-type pulses using an oscilloscope or other recording device. This current-viewing probe can be placed either in the drain node or between the stiffening capacitor and ground.

Alternatively to the drain current, it is possible to monitor the drain voltage and verify on reduction beyond a certain threshold compared to the test voltage (typically the 80%).

There are no non destructive test methods applicable to SEGR to date.

SEB pulse

The observed non destructive pulses are those which would have caused device burnout if there were no current limiting. Once properly designed the

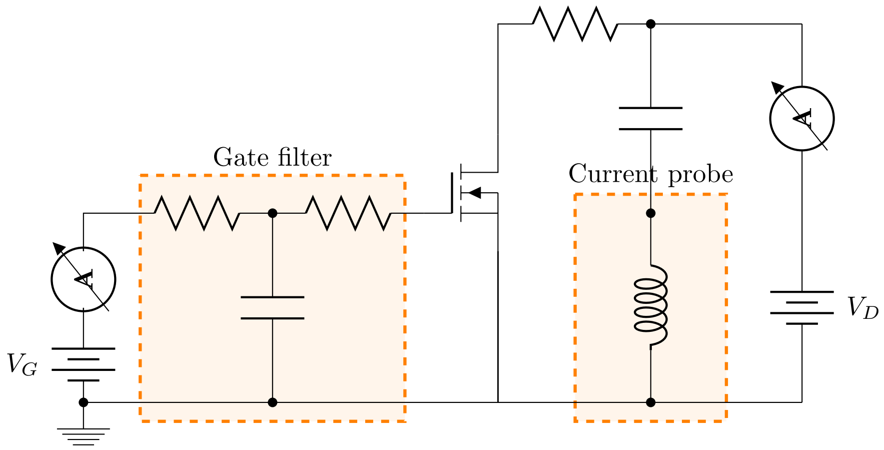

Figure 2.6: Basic non destructive SEB test circuit

circumvention network, the basic assumption is that significant pulses are observed only in the case of potential SEB events; otherwise no pulses are observed. Of course it all depends on the value of the series resistance. As an example, we report the SEB pulses observed by Obert and Wert [23] in figure 2.7. In particular, on the left we have a non-destructive pulse observed with a limiting resistor of 1 kΩ and on the right we have the corresponding destructive pulse obtained with the same test voltage and the same radiative conditions, but with no limiting resistor.

Circumvention network design criteria

As previously mentioned, protective SEB test method was originally proposed by Oberg and Wert [23] in 1987. Their experimental results showed that adding a drain resistor of 1 kΩ or higher would provide needed protection against SEB. Though widely adopted immediately after their work, protective SEB test method has not been fully evaluated in terms of how to select the resistor that would provide the needed protection. Recently, Liu et al [18] have proposed a circumvention network design criteria based on the quasi-stationary avalanche curve of the DUT, obtained by TCAD simulations. As a short remainder, this curves (see figure 2.8) are traced over the breakdown regime (so in the off condition, with gate and source contacts shorted) and are characterized by a negative differential resistance region for very high drain current densities. This region is delimited by 2 snap-back points [20]: the first, with lower drain current, where the negative differential resistance region initiates, corresponds to the parasitic BJT activation and the second, where the negative differential resistance region finishes, corresponds to the second breakdown onset. Furthermore, this second point has a voltage value (V_{sb}) lower than the nominal breakdown and it is associated with the SEB threshold. In order to prevent failure events, the series resis-

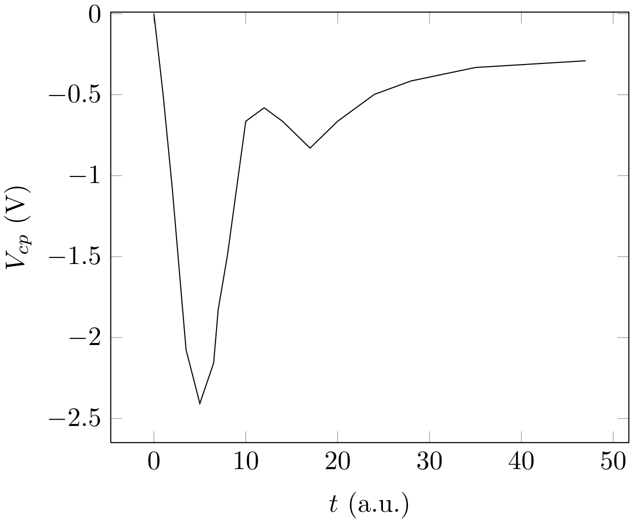

(a)

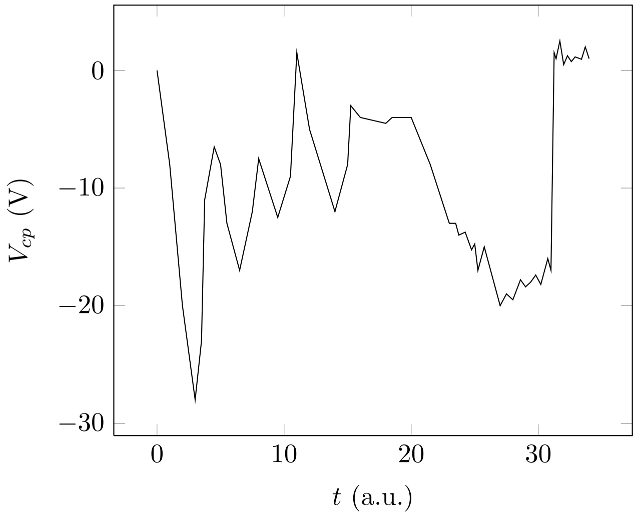

(b)

Figure 2.7: SEB waveforms recorded with a current probe. A safe pulse, i.e. that decays to zero, is represented in 2.7(a); a destructive pulse doesn't extinguish as depicted in 2.7(b). Note, also, the different amplitudes

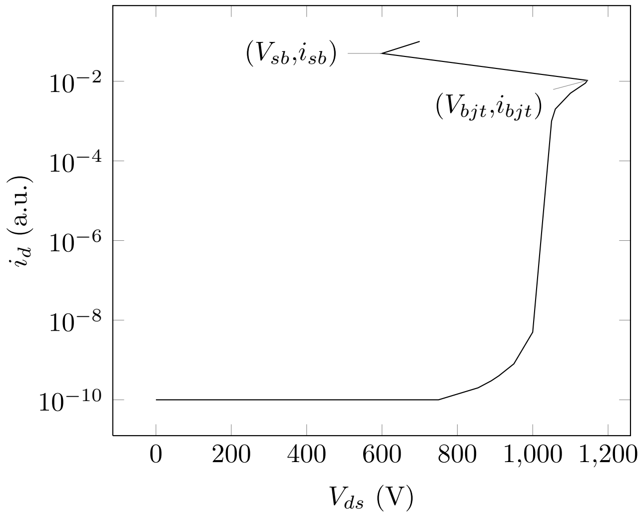

Figure 2.8: Typical avalanche curve obtained by TCAD simulations

tance R_s have to limit the drain current I_d to a lower value than the second breakdown current I_{sb}, that is:

$$I_d = \frac{V_{test} - V_{sb}}{R_s} < I_{sb}$$

where V_{test} is the test voltage. Therefore:

$$R_s > \frac{V_{test} - V_{sb}}{I_{sb}} \tag{2.3}$$

The limit of this approach is that the avalanche curves can not be obtained experimentally and then the series resistor choice is linked to the goodness of the simulations. However, this is the first ever attempt to provide objective criteria for SEB circumvention network design.

2.4 Adopted neutron facilities

2.4.1 ANITA

ANITA is a neutron facility at the TSL in Uppsala (Sweden), specifically designed for accelerated SEE testing. ANITA exploit the spallation process, a particular nuclear reaction in which a light projectile (mostly proton) with the kinetic energy from several hundreds of MeV to several GeV interacts with a heavy nucleus (e.g., lead) and causes the emission of a large number of neutrons or fragments. On average, about 20 to 30 neutrons are expelled for each incoming proton. This type of neutron facilities are classified as ?pulsed? because they can be instantly turned on or off, simply shuttering

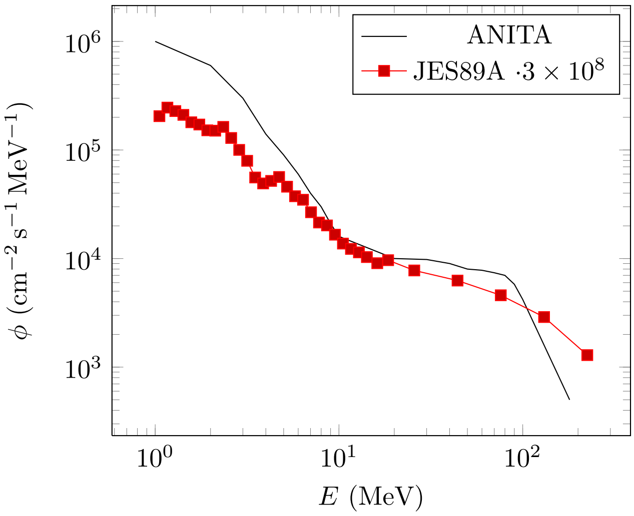

Figure 2.9: Energy spectrum comparison between the ANITA facility and terrestrial neutrons with energies higher that 1 MeV, according the standard JESD89A

or not the primary proton beam (in reactor or radioisotopes nuclear sources, the shut down depends on the decay of the radionuclide involved in the reaction, having its own characteristic half-life time). Before being fired upon the target, the protons pass into a ring where they accumulate in bunches. Each bunch of protons is released from the ring as a pulse. The high-energy proton pulses strike a heavy-metal target, which is a container of liquid mercury. Corresponding pulses of neutrons freed by the spallation process are slowed down in a moderator and guided through beam lines to areas containing highly specialized instruments for conducting experiments.

An attractive feature of the spallation sources is that they produce neutrons with so-called *white* spectra, which resemble the spectrum of neutrons in the atmosphere and at the terrestrial level. In fact, the spallation process mimics the natural interactions between primary cosmic rays and atmospheric atoms leading to *cascade* and *evaporation* peaks in the neutron spectrum (at 100 MeV and 1 MeV, respectively). A comparison between the terrestrial neutron spectrum for energies higher than 1 MeV and the ANITA spectrum is showed in figure 2.9.

A schematic layout of ANITA is presented in figure 2.10.

After acceleration in the Gustav Werner cyclotron, the primary proton beam with the energy of approximately 180 MeV is guided to a 2.4 cm thick 99.8% pure tungsten target, which fully stops the incident protons. The target is situated inside the massive bending magnet in a concrete cave for enhanced shielding of surrounding areas against neutrons and gamma rays produced in the target.

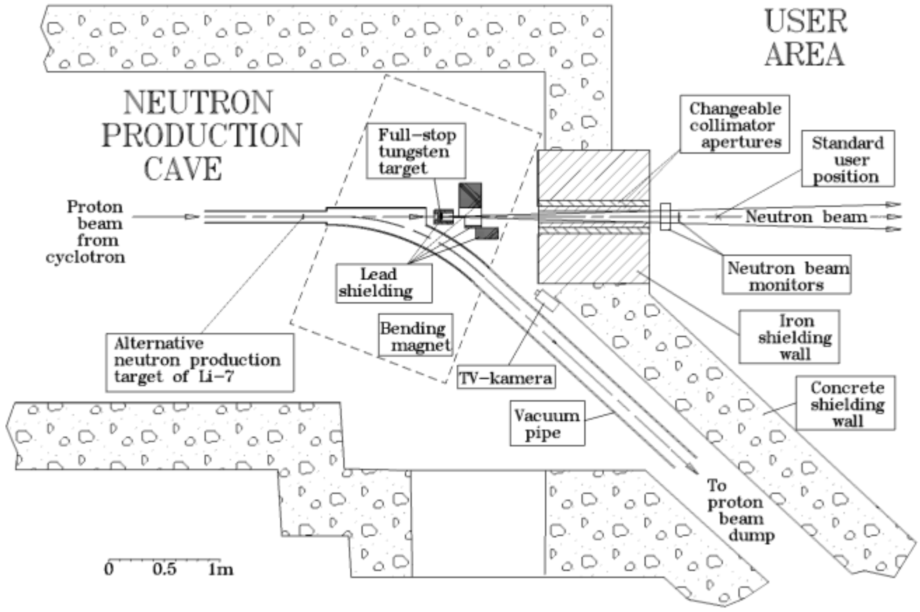

Figure 2.10: Anita facility schematic layout

The neutron beam is formed geometrically by a collimator aperture in a 1 m thick iron frontal wall, which separates the neutron production cave from the user area. A modular design of the aperture allows the user to select the size and the shape of the neutron beam. At present, cylindrical apertures are available with diameters of 2, 3, 5.6, 7.5, 10.2, 15.7, 20 and 30 cm. In addition, a 1 cm × 1 cm square aperture is also available.

Downstream of the aperture, the neutron beam arrives at neutron monitor devices based on ionization chambers and thin film breakdown counters. An additional monitoring option is provided by measurement of the proton beam current on the neutron production target, which functions as a Faraday cup. All mentioned monitors operate in real-time mode and produce electrical pulses that are counted and logged in the facility control system. Both the pulses and the logs are available for the user on-line.

The temporal structure of the neutron beam is defined by the corresponding structure of the primary proton beam. It is made up of periodic macro pulses with a typical duration of almost 500 µs. The repetition rate of these macro pulses can be changed in the range from 1 Hz to at least 150 Hz. Each macro pulse is in turn made up of a trail of micropulses, with a repetition frequency of 22 MHz and 4 ns duration. The macro pulse repetition rate affects the average neutron flux.

The user area extends from 250 cm to 15 m downstream of the production target. The neutron beam propagates from the production target towards the beam dump as a cone or as a pyramid, for cylindrical and square apertures,

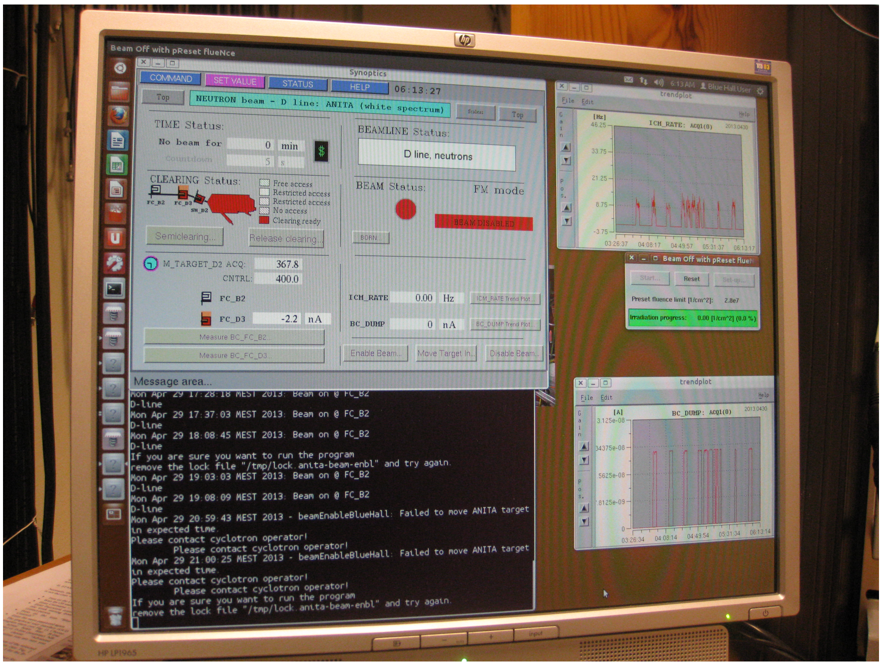

NEUTRON beam - D line: ANITA (white spectrum)

No beam for 0 min

Countdown 5 s

D line, neutrons

BEAM DISABLED

M_TARGET_D2 ACQ: 367.8

CNTRL: 400.0

FC_D3 -2.2 nA

ICM_RATE 0.00 Hz

BC_DUMP 0 nA

Preset fluence limit [1/cm^2]: 2.8e7

Irradiation progress: 0.00 [1/cm^2] (0.0 %)

Message area...

```
Mon Apr 29 17:28:18 MEST 2013: Beam on @ FC_B2
D-line
Mon Apr 29 17:37:03 MEST 2013: Beam on @ FC_B2
D-line
Mon Apr 29 18:08:45 MEST 2013: Beam on @ FC_B2
D-line
If you are sure you want to run the program
remove the lock file "/tmp/lock.anita-beam-enbl" and try again.
Mon Apr 29 19:03:03 MEST 2013: Beam on @ FC_B2
D-line
Mon Apr 29 19:08:09 MEST 2013: Beam on @ FC_B2
D-line
Mon Apr 29 20:59:43 MEST 2013 - beamEnableBlueHall: Failed to move ANITA target
in expected time.
Please contact cyclotron operator!
        Please contact cyclotron operator!
Mon Apr 29 21:00:25 MEST 2013 - beamEnableBlueHall: Failed to move ANITA target
in expected time.
Please contact cyclotron operator!
        Please contact cyclotron operator!
If you are sure you want to run the program
remove the lock file "/tmp/lock.anita-beam-enbl" and try again.
```

Figure 2.11: GUI of the BORN system at TSL

respectively, with the beam axis going at the height of 1.5 m above the floor.

The highest neutron flux is available at the Standard User Position (SUP), located at the distance $L_{SUP} = 250\,\mathrm{cm}$ downstream of the production target. The energy integrated neutron flux above 10 MeV amounts to $10^6\,\mathrm{cm}^{-2}\,\mathrm{s}^{-1}$. The minimum flux in the same conditions is $200\,\mathrm{cm}^{-2}\,\mathrm{s}^{-1}$. The flux can be further decreased to the minimum of $5\,\mathrm{cm}^{-2}\,\mathrm{s}^{-1}$ by placing the DUT closer to the downstream end of the beam path. Anyway, at a given position, the available flux variation amounts to at least a factor of 150, which is achieved by variation of the repetition frequency of the beam macro pulses.

Users can control the beam operation from the PC in the counting rooms, thanks the Automated WorkPlace (AWP), i.e. a control software, with a simple graphical interface, that allows you to:

- enable/disable the beam;
- control the clearing procedure outcome;
- start the beam;
- monitor the output signals from the dosimeters in real time.

Another important feature of the ANITA AWP is the Beam Off with pReset flueNce (BORN) system: the user chooses a set point fluence and the system .automatically stops the beam as soon as the pre-set fluence is achieved.

2.4.2 UniPA

The UniPA facility is made up of several Am-Be sources. In this type of sources, neutrons are emitted through the (α, n) reaction that is obtained by mixing (typically in the form of powders) a radioisotope that decays spontaneously with alpha particles and a low atomic weight material. In the case of Am-Be sources, the reaction is the following:

$$\alpha + {}^{9}_{4}\mathrm{Be} \longrightarrow {}^{12}_{6}\mathrm{C} + n \tag{2.4}$$

where the alpha particles comes from the natural decay of ^{241}Am isotope. It should be noted that, depending on a radioisotope decay, this neutron source cannot be instantaneously turn off, such as spallation sources.

The typical neutron spectrum obtained with a Am-Be source is between few keV and 12 MeV: the flux peak is about $1 \times 10^{6}\,\mathrm{cm^{-2}\,s^{-1}}$ at 5 MeV.

The UniPA facility is made up of 4 Am-Be sources located on the bottom of a water pool, in order to obtain an adequate level of radiation shielding. These sources are placed at the corners of a 20 cm square. At the centre of this square there is a vertical tube used as a sample holder with an inner diameter of 25 mm, a length of 1 m and a watertight closure at the lower end. Therefore, the neutrons emitted by the sources must cross a thickness of about 14 cm of water before reaching the sample holder compartment, which is invested by 4 directions to ensure a uniformity of irradiance that was estimated to be better than 3% in the experimental volume where the devices are placed. To obtain information about the intensity and spectrum of the neutron flux, 2 complementary analysis were performed: simulations of neutron transport with MCNP [1] and activation analysis.

The simulated energy spectrum is depicted in figure 2.12. Due the water moderation, we have a large component of thermal neutrons, but there are also fast neutrons having energies between 1 MeV and 11 MeV.

The neutron activation analysis was performed to experimentally verify the presence of fast neutrons, with energies greater than the threshold values for the (n, α) and (n, p) reactions with the ^{28}Si isotope (2.60 MeV and 3.87 MeV respectively). In this type of investigation, the sample is irradiated till saturation (i.e. an equilibrium condition between the rate of production of a radionuclide and their decay) and subsequently analyzed with a gamma-spectrometer, which allows the qualitative and quantitative determination of the gamma-emitting radionuclide. To detect fast neutrons, we chose a sample of aluminium with the following features: radius 0.635 cm, thickness 0.0762 cm, weight 0.2566 g, ^{27}Al 100% isotopic ratio. The examined interactions are summarized in table. In our case, the sample was irradiated for 48 hours and 20 minutes and analysed with the spectrometer for 2000 and 15 000 s, in order to identify the greater and smallest half life radioisotopes. Both readings have produced positive results verifying the presence of the two radioisotopes.

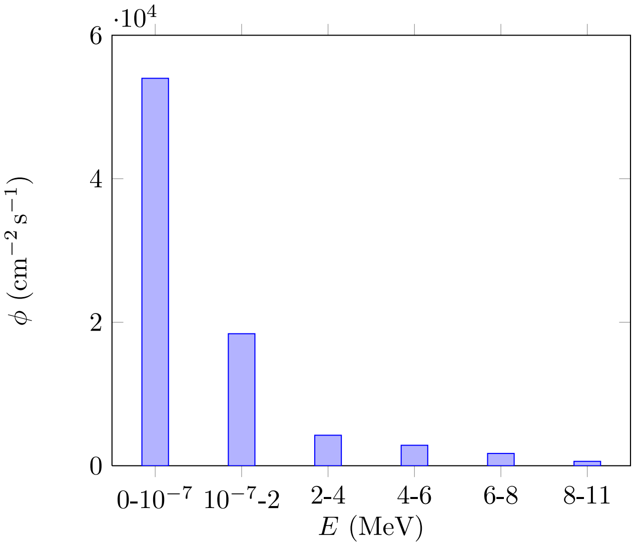

Figure 2.12: UniPA estimated spectrum with MCNP simulations

Interaction	E_{th} (MeV)	$t_{1/2}$	E_γ (MeV)
$^{27}\mathrm{Al}(n,\alpha)^{24}\mathrm{Na}$	4.9	15.0 h	1.37
$^{27}\mathrm{Al}(n,p)^{27}\mathrm{Mg}$	3.8	9.4 min	0.84-1.01

Table 2.1: Nuclear reactions used for the activation analysis, with the respective threshold energies (second column), half-life time (third column) and gamma energies (fourth columns)

Therefore, the flux was calculated from the gamma rays counts detected by the spectrometer at the characteristic energies in table 2.1as it follows:

$$\varphi = \frac{C \cdot \lambda}{\varepsilon \cdot I \cdot \Sigma_{mac}} \frac{1}{a \cdot b \cdot c} \tag{2.5}$$

where C is the number of counts recorded for a given energy value, λ is the decay constant of the activated nucleus, ε is the detection efficiency, I is the emission intensity, Σ_{mac} is the sample macroscopic cross section, a, b and c are temporal functions which state the number of activated nuclei in the sample during the different stages of the analysis. In particular:

$$\begin{aligned} a &= 1 - \exp\left(-\lambda \cdot t_i\right) \\ b &= \exp\left(-\lambda \cdot t_w\right) \\ c &= 1 - \exp\left(-\lambda \cdot t_c\right) \end{aligned}$$

where t_i, t_w and t_c are the irradiation, transfer and detecting times. The experimental ($6.39 \times 10^2\,\mathrm{cm}^{-2}\,\mathrm{s}^{-1}$) and simulated ($6.09 \times 10^2\,\mathrm{cm}^{-2}\,\mathrm{s}^{-1}$) flux values were compared in the energy range between 8 MeV and 11 MeV in which the cross section are relevant for the activation and differs from each other by an amount less than 5%.

2.5 Experimental apparatus

Our experimental approach for SEB measurements was to perform characterization test (with different bias voltages), as defined in MIL 750 E, method 1080, using a destructive test circuit. Obviously, not circumventing SEB, we didn't count pulses nor calculated cross sections, but we measured the failure times and performed statistical analysis to evaluate more significant quantities in the reliability context, such as failure time and MTTF. A similar approach has been used in [8], but for real-time testing. On the other hand, for a significant statistics, we needed many failures and a big sample size. In order to improve the testing throughput, we specially designed a circuit for testing 8 DUTs per run/exposure. In this section we describe all the details relating to the design of this apparatus.

2.5.1 Block diagram and schematics

During an exposure, for obvious security reasons, the user cannot stay in the irradiation room, so the instrumentation should be automated and remotely controlled from a separate room or at a safe distance.

The block diagram of our experimental apparatus is depicted in figure 2.13. The core block is the host PC, running a software, developed with the National Instruments Labwindows C Virtual Instrument (CVI) suite. The PC acquires data from a DAQ board in the experimental hall through an ethernet connection. In particular, the DAQ board consists of 2 elements:

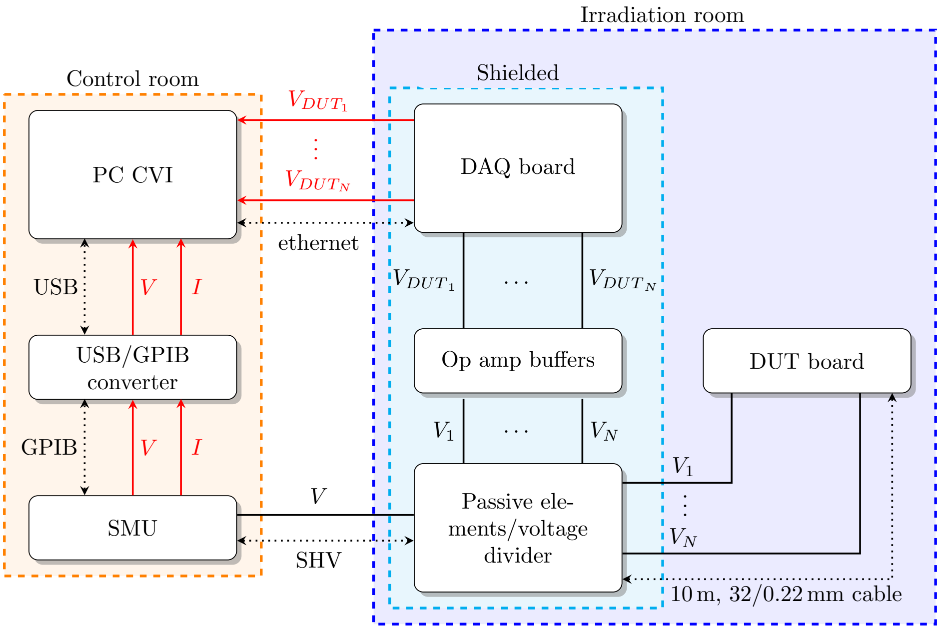

Figure 2.13: Block diagram of the experimental apparatus

1. the National Instruments CompactDAQ 9184 [2], which is a 4 slot Gigabit ethernet chassis, designed for remote or distributed sensor and electrical measurement;
2. the National Instruments 9205 C-Series analog input module [3], with the following features: 32 (in single ended mode) or 16 (in differential mode) multiplexed voltage channels, 16 bit Analog to Digital Converter (ADC) resolution, 250 $\mathrm{kS\,s^{-1}}$ sampling rate, ±10 V, ±5 V, ±1 V and ±0.2 V signal input range, isolation.

The ethernet technology convenience and reliability are long cabling lengths and distributed infrastructure. In fact ethernet is ideal for taking measurements at distances beyond the 5 m limit of a Universal Serial Bus (USB) cable. A single CAT 5E cable can reach 100 m before needing a switch or router to carry the signal farther. Furthermore, one host computer can manage multiple test stations within the same facility or across multiple sites.

The host PC also manages a SMU, which is strategically located in the control room: in fact, it also consists of power switching circuits and may be subject to SEB if exposed in the proximity of the neutron source. The SMU provides the supply voltage to the test circuit and, at the same time, it measures the output current. In our test equipment, we used a Keithley 2410-C, a 20 W instrument that sources and measures voltage from ±5 µV (source) and ±1 µV(measure) to ±1100 V and current from ±10 pA to ±1 A. The Model 2410-C is also able to measure 20 mA while sourcing 1100 V,

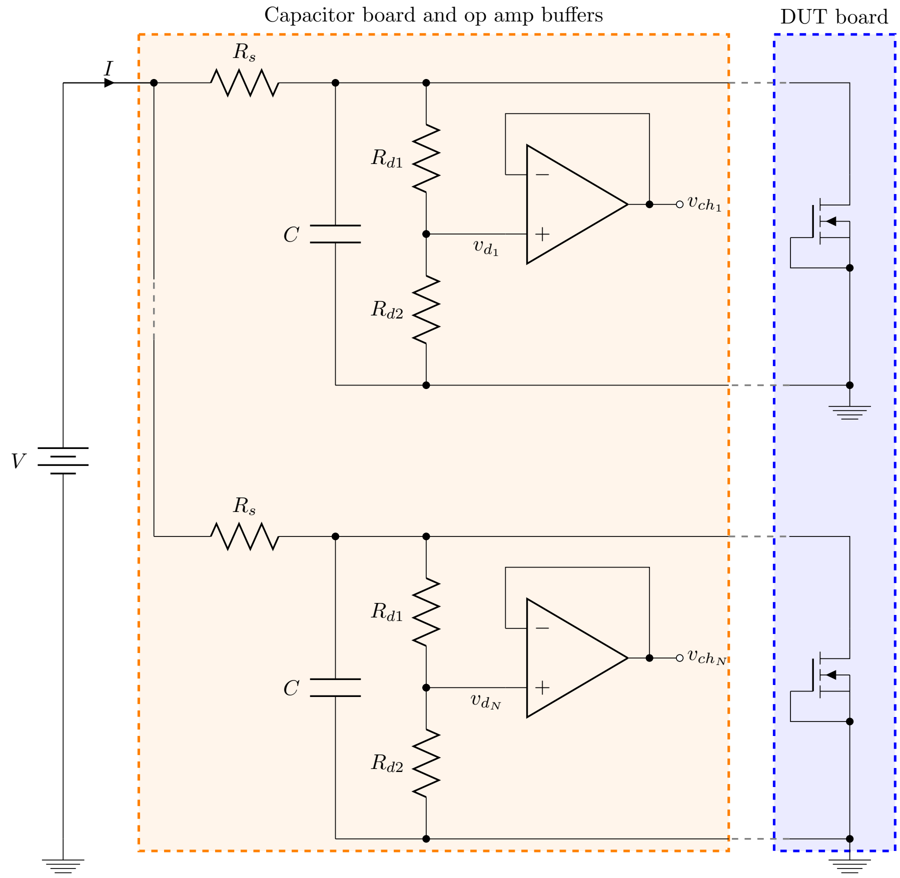

Figure 2.14: Test circuit schematics

providing the extra resolution needed for precision testing of power devices. Another interesting feature of this SMU is the four-quadrant operation, i.e. it can supply positive voltages with negative currents and vice versa. So it can also dissipate power. This mode is used to discharge the capacitances connected in parallel to the DUTs, during the shut down. Otherwise, we would have to design specific circuits for this purpose.

The remote control of the SMU is via the General Purpose Interface Bus (GPIB); on the PC side a GPIB/USB converter is used.

The test circuit is placed in the experimental room and is physically implemented in two modules: the DUT board and the capacitor board. The first module is directly exposed to the neutron beam and contains only the DUTs, with their connections. In particular, the gate and source terminals are locally shorted, while the drain and source terminals are connected to output cables. Actually, being all connected to the same potential, the sources have been shorted to have a single mass cable. The capacitor board is placed, together with the DAQ, at a distance of 10 m from the DUT board

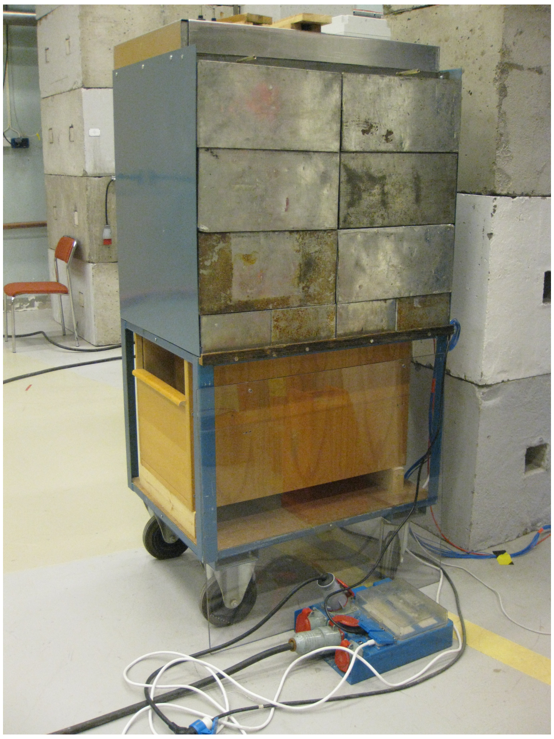

Figure 2.15: Instrument and capacitor board protection with borated wax bricks at the ANITA facility

(see figure 2.16). In fact, at this security distance, the neutron field is less intense. At the TSL, we used a shielded cabinet filled by borated wax bricks in order to absorb thermal neutrons and to protect the equipment (see figure 2.15). The capacitor board is powered by the SMU through a Safe High Voltage (SHV) coaxial cable that extends up to the control room. Furthermore, the capacitor board is constituted by a module with different passive components and by a series of voltage follower for the appropriate signal conditioning (attenuation and impedance matching) of the drain voltages upstream of the ADCs.

The test circuit schematic is shown in figure 2.14. There are so many derivations of the test voltage V as the number of DUTs. Each branch has a series resistor and a parallel capacitor. In steady-state conditions, the capacitor is charged to the test voltage and the DUT leakage current flows into the series resistor, with a negligible voltage drop. If a SEB event occurs, it develops a conductive path between the drain and source contacts of the failed DUT: as a result, the drain voltage suddenly collapse and the capacitor discharges, releasing the previously stored energy. After that, the series resistor limits the post-SEB current to a few mA, avoiding the DUT over damaging (explosion) and the power supply shut down. Note how the

Figure 2.16: Capacitor and DUT boards arrangement into the irradiation room at the UniPA neutron facility

failure of one DUT does not affect the test prosecution on the others, given the separate RC filters.

The figure 2.17 shows the drain voltages and the current supplied by the SMU, measured during a test. At the beginning of the run, the test voltage has been supplied with a slow ramp to prevent the of parasitic BJT turn on because of excessive dV/dt. The same applies to the end of the run, where shut down takes place with a ramp down. During these phases, the current supplied by the SMU is not negligible due to the charge/discharge of the capacitors. In particular, during the ramp down, the current is negative because it is absorbed by the SMU. The SEB events correspond to sudden drops in drain voltages; correspondingly, SMU current steps can also be observed.

2.5.2 Capacitor board design

For the capacitor board design, we referred to the following operating condition: test voltage equal to the maximum voltage supplied by the SMU, i.e. 1100 V and 8 samples to be tested. Another fact is that most of the samples has a maximum leakage current of less than 1 µA.

The voltage divider resistors have been chosen so as to lower the maximum voltage drain from 1100 V to 5 V and to absorb a current equal to the maximum leakage current. Therefore, the total resistance is:

$$R_{d1} + R_{d2} = \frac{V_{max}}{I_{dss}} = \frac{1100\,\mathrm{V}}{1\,\mu\mathrm{A}} = 1.1\,\mathrm{G\Omega}$$

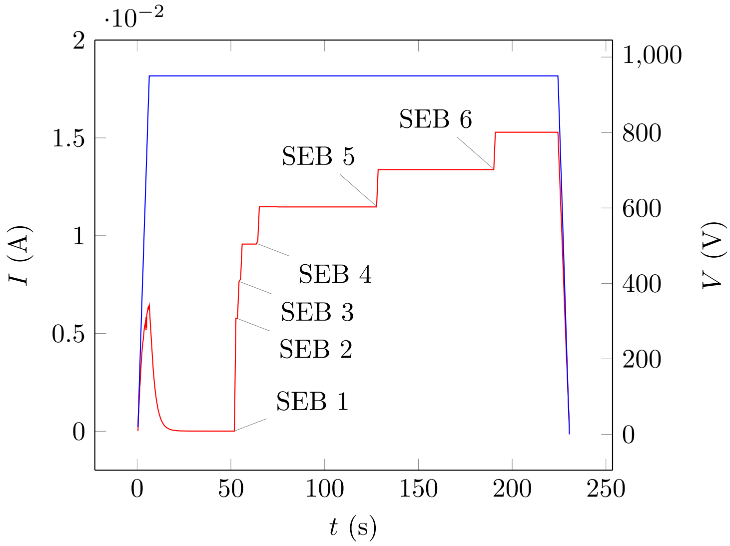

Figure 2.17: Typical trend of the SMU current and voltage during a test

The voltage taken form the divider is:

$$v = V_{max} \cdot \frac{R_{d2}}{(R_{d_1} + R_{d_2})}$$

Hence:

$$R_{d_2} = \frac{v \cdot R_{d1} + R_{d2}}{V_{max}} = \frac{5\,\mathrm{V} \cdot 1.1\,\mathrm{G\Omega}}{1100\,\mathrm{V}} = 5\,\mathrm{M\Omega}$$

For the series resistor we set 2 constraints:

1. a voltage drop (due to the pre-SEB current, i.e. the sum of the leakage and the divider currents) less than 1% of the test voltage;
2. the sum of all post-SEB currents (in the worst case with all DUTs failed) less than 20 mA, i.e. the maximum current supplied by the SMU with a test voltage of 1100 V.

This latter condition is equivalent to require a maximum post-SEB current equal to 2.5 mA for each test circuit branch, i.e. one-eighth of 20 mA. The first constraint imposes an upper limit:

$$R_s < \frac{0.01 \cdot V_{max}}{2 \cdot I_{dss}} = \frac{11\,\mathrm{V}}{2\,\mathrm{\mu A}} = 5.5\,\mathrm{M\Omega}$$

while the second constraint imposes a lower limit, assuming that the drain-source resistance of a failed DUT is much lower than the series resistance:

$$R_s > \frac{V_{max}}{I_{max}/8} = \frac{1100\,\mathrm{V}}{20\,\mathrm{mA}/8} = \frac{1100\,\mathrm{V}}{2.5\,\mathrm{mA}} = 440\,\mathrm{k\Omega}$$

The Capacitance values were chosen to guarantee an amount of available energy for SEB equal to the single avalanche energy (E_{as}). We have done so to identify clearly visible damaging traces on the die surface with a microscope without resorting to the liquid crystal technique.

When selecting passive components for high voltage applications, one should not only verify the resistance or capacitance values, but also the maximum voltage and power dissipation ratings. The chosen elements have the following characteristics:

- axial metal film resistor pairs of 220 kΩ and 270 kΩ (a total resistance of 490 kΩ), with a relative tolerance of 5%, maximum voltage of 500 V and maximum power of 3 W, for R_s;
- radial thick film resistors of 1 GΩ, with a relative tolerance of 1%, maximum voltage of 15 kV and maximum power of 3 W, for R_{d1};
- axial metal glaze resistors of 4.7 MΩ, with a relative tolerance of 5%, maximum voltage of 10 kV and maximum power of 1 W, for R_{d2};
- through hole polypropylene film capacitors of 5 µF, with a relative tolerance of 10%, maximum voltage of 1300 V and Equivalent Series Resistance (ESR) of 6 mΩ.

With these resistance and capacitance values, the DAQ inputs see very high impedance signals. This can lead to *ghosting* or *cross-talk* issues. To better understand, we need to deepen the DAQ internal structure (see figure). The NI 9205 C-Series module has one ADC. The multiplexer routes one analog input channel at a time to the ADC through the Programmable Gain Instrumentation Amplifier (PGIA), which applies a different gain setting to the AI signal depending on the input range. The NI 9205 C-Series devices can scan multiple channels at high rates and digitize the signals accurately. However, in multichannel scanning applications, accuracy is affected by settling time. When the device switches from one AI channel to another AI channel, it configures the PGIA with the input range of the new channel. The PGIA then amplifies the input signal with the gain and polarity for the new input range. *Settling time* refers to the time it takes the PGIA to amplify the input signal to the desired accuracy before it is sampled by the ADC. To ensure fast settling times, the signal sources should have an impedance lower than 1 kΩ. Settling times increase when scanning high impedance signals due to a phenomenon called *charge injection*. Multiplexers contain switches, usually made of switched capacitors. When one of the channels, for example channel 0, is selected in a multiplexer, those capacitors accumulate charge. When the next channel, for example channel 1, is selected, the accumulated charge leaks backward through that channel. If the output impedance of the source connected to channel 1 is high enough, the resulting reading of channel 1 can partially reflect the voltage on channel 0. This is referred to as ghosting, or

RS-code	Description	Producer
683-5329	4.7 MΩ resistor, 5%, 1 W, 10 kV	Vishay
296-0780	1 GΩ resistor, 1%, 4 W, 15 kV	TE Connectivity
683-5938	270 kΩ resistor, 5%, 3 W, 500 V	Vishay
683-5934	220 kΩ resistor, 5%, 3 W, 500 V	Vishay
669-0000	5 µF capacitor, 10%, 1.3 kV	TE Connectivity
356-8543	TLC2202CP dual precision op amp	Texas Instruments
748-2030	PVC equipment wire 32/0.2 mm, 100 m	RS

Table 2.2: Bill of materials for capacitor board

crosstalk. To mitigate this effect we used a voltage buffer, for each channel in order to reduce the impedance seen from the DAQ device. In particular, we used the Texas Instruments TLC220, a precision, low-noise operational amplifier, with input impedance levels comparable to top-gate JFET and expensive dielectric-isolated devices.

Finally, the board wasn't realized on a common breadboard or Printed Circuit Board (PCB): we used the Poly Methyl Metha Crylate (PMMA), because it slows down neutrons. The board layout is shown in figure. A bill of material is reported into table 2.2.

2.5.3 DUT board

As the name suggests, the DUT board only contains the DUTs and it is placed on the beam line. Its function is to provide mechanical support to the samples and to implement their terminal connections. The DUT board was realized in PMMA as the capacitor board.

We designed two different boards: one for ANITA and the other for the UniPA facility. The ANITA board is 14 cm × 21.5 cm and it has a central hole with a diameter of 10 cm. DUTs are arranged around the circumference as shown in the figure 2.19. In particular we used several screw connectors, so as to switch the devices between one run and the other. The special arrangement of the DUT comes from the circular symmetry of the beam and was realized to achieve a uniform irradiation among the different samples.

We could not use the same system for the UniPA experiment. In this case, in fact, the samples are submerged in a water tank, through a watertight polyethylene [1] rod. It is 2 m long and has a circular section of diameter equal to 21 mm. The rod has a groove inside that is used to accommodate the DUT board and the power cables. Of course, the end of the rod in contact with the water inside the tank is stoppered. The UniPA board is 1.4 cm × 9.7 cm and the DUTs are arranged back to back as showed in figure 2.20.

---

[1] The polyethylene is a neutron moderator

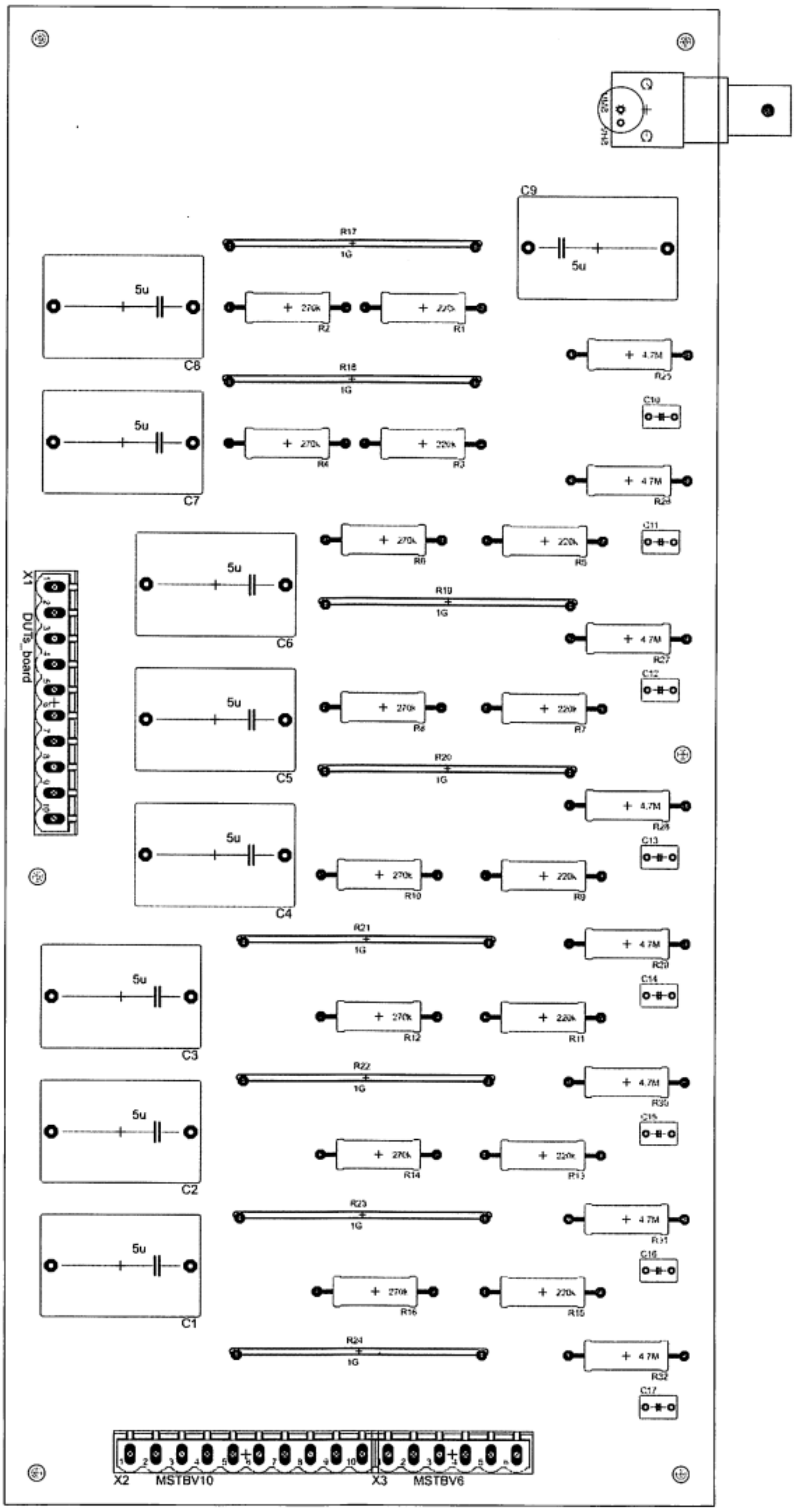

Figure 2.18: Capacitor board layout

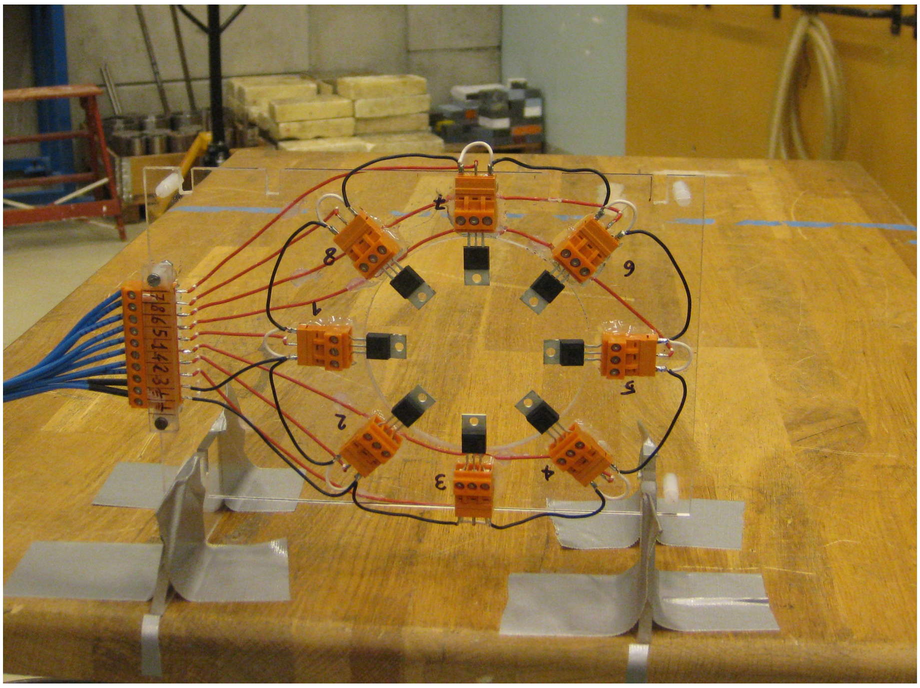

Figure 2.19: DUT board for the ANITA experiment

Figure 2.20: DUT board for the UniPA experiment

2.6 Virtual Instrument programming

As previously mentioned, the control program for our experimental apparatus was developed with Labwindows CVI, a software development environment for C programmers. You can use Labwindows CVI for the following tasks:

- interactively develop programs;
- access powerful function libraries for creating data acquisition and instrument control applications;
- take advantage of a comprehensive set of software tools for data acquisition, analysis, and presentation.

Labwindows applications generally have a GUI (which can be seen as the front panel in LabVIEW) and are structured according to the event-driven approach: the program flow is therefore determined by the occurrence of events, which can be associated to elements of the graphical interface (e.g. a button pressure) or to the hardware resources (e.g. reading of N bytes from the serial port, empty buffer of a DAQ board, etc.). Other events can be defined by the user. The typical structure of a program includes a main function that loads the GUI panel and a set of callback functions that are invoked upon the occurrence of the defined events.

The program will:

- manage the signal acquisition with the DAQ board, saving data to file;
- control the SMU to providing the test voltage and acquire voltage and current measurements (also in this case data will be saved to file);
- plot data in real-time on 9 graphs (1 graph for each channel of the DAQ and 1 graph for the SMU);
- save the ramp-up, beam on, beam off, ramp-down and stop acquisition times on a time-stamp file.

The time-stamp file is used to correctly compute the failure times of the DUTs, having a unique acquisition file for a run, started with the test voltage ramp up and ended with the stop acquisition callback.

2.6.1 DAQ management

Labwindows applications often require acquiring data. If National Instruments hardware products are used, the application development is particularly simplified thanks to the DAQmx driver. It defines an Application Programming Interface (API), which is the same across both device functionality and device families. This means that all of the functionality of a multifunction device is programmed with the same set of functions (analog input, analog output, digital I/O, and counters). Furthermore, both a digital I/O device and an analog output device are programmed using this same set of functions.

If you want to perform a measurement or a signal generation with a National Instruments DAQ board, you have to define a task and get it started. A task is a collection of one or more virtual channels with timing, triggering, and other properties. In our case, we have defined a task with 8 analog input channels for measuring voltage signals in the range of ±5 V, using a Non Referenced Single Ended (NRSE) configuration. In an NRSE measurement system, all measurements are made with respect to a common point (the analog input sense), whose potential can vary with respect to the measurement system ground. This configuration is particularly suited for ground referenced signal sources, because it provides almost the same common mode rejection with respect the differential configuration, but it requires less input channels. The next step was the definition of the clock specifications. In particular, we selected the on-board clock, with the rising active edge, a 100 Hz acquisition frequency, 20 samples per channel and the continuous sampling mode (the DAQ board acquires samples as long as the task is enabled). We associated a specific controller on the GUI for each of these parameters, giving the possibility to the user to change their values from one run to another. With the logging option enabled, the DAQmx can automatically write data to file, i.e. without explicit I/O file statements, as fprintf. Only file path and name are needed. Data are stored in a binary format, the Technical Data Management Streaming (TDMS), specifically designed by National Instruments to efficiently manage data streaming, even at high sample rate. Although a proprietary format, TDMS files can be imported by third party software such, as Excel or Origin. In addition to storing data to a file, we need to plot them in real time on the GUI stripcharts. This means that, at regular intervals, we need to read data from the PC buffer and save them into a dynamically allocated array. For this purpose, we defined an *Every N Sample* event and the appropriate callback function (see figure 2.21), which is called whenever N samples are transferred from the device to the PC buffer. This callback function perform the operations described above.

2.6.2 SMU management

The SMU have to provide the test voltage and, at the same time, measure the output current. The operations to be performed in order to properly set the SMU in the source mode are:

1. set the voltage source level;
2. set the compliance current limit;

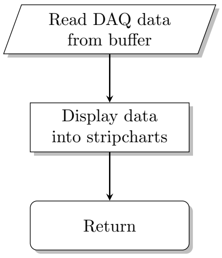

Figure 2.21: DAQ Every N Sample callback flowchart

3. turn output on.

Indeed, to use the SMU as a voltmeter and/or ammeter, it should:

1. select the measurement function;
2. select the measuring range;
3. set the measurement speed.

The speed is meant as the integration time of the ADC, i.e. the period of time the input signal is measured. Integration time affects the reading noise and the ultimate reading rate of the instrument. It is specified in parameters based on the Number of Power Line Cycles (NPLC), where 1 NPLC for 50 Hz is 20 ms. In general, the fastest speed setting (0.01 NPLC) result increased noise, while the slowest speed (1 NPLC) provides the best common mode and normal mode noise rejection. In between settings are a compromise between speed and noise.

Each of the operations described above can be performed either manually, from the instrument front panel, or remotely, sending the appropriate statements via GPIB. This statements are defined in accordance with the SCPI requirements. Some of the most common SCPI statements are reported into table 2.3.

The GPIB communication between the PC and SMU is handled by the Virtual Instrument Software Architecture (VISA) driver, that provides the programming interface between the hardware and the labwindows development environment. Once configured the VISA session with the resource address (in our case, the GPIB address GPIB0::24::INSTR), the communication with the SMU take place with read and write statements, as if it were a common RS-232 serial communication. Write statements are used for the SMU settings, while the read statements are used to acquire the measurements.

2.6.3 Multi-threading

With multi-threading, applications can separate their own tasks into individual threads. In a multi-threaded program, the operating system directs

Command	Description
:SOURce:FUNCtion <name>	Select source function; <name>=VOLTage or CURRent.
:SOURce:xxx:MODE FIXed	Select fixed V or I sourcing mode.
:SOURce:xxx:RANGe <n>	Select measurement rage for V or I source; <n>=range.
:SOURce:xxx:LEVel <n>	Set source amplitude; <n>=amplitude in volts or amps.
:SENSe:FUNCtione <name>	Select measurement function; <name>=VOLTage or CURRent.
:SENSe:xxx:PROTection <n>	Set V or I compliance; <n>=compliance.
:SENSe:xxx:RANGe <n>	Select V or I measurement range; <n>=range.
:SENSe:xxx:RANGe:AUTO <b>	Enable or disable auto range; <b>=ON or OFF.
:OUTPut <b>	Turn output on or off; <b>=ON or OFF.
:READ?	Trigger and acquire one data string

Table 2.3: Most common SCPI commands for the SMU (xxx=VOLTage or CURRent)

each thread to execute code for a period of time, referred to as a time slice, before switching execution to another thread. The act of stopping execution of one thread and starting execution of another is referred to as a thread switch. The operating system typically can perform thread switches quickly enough to give the appearance of concurrent execution of more than one thread at a time. With multiprocessing power, a multi-threaded application can run multiple threads simultaneously, finishing more tasks in less time; to achieve maximum performance from multi-threaded operating systems and/or multiprocessor machines, an application must be multi-threaded.

Labwindows software, not only natively support multi-threaded application creation, but also provide performance optimizations over standard interface to Win32 API threading functions. For example, thread pools help user schedule functions for execution in separate threads. Furthermore, thread pools handle thread caching to minimize the overhead associated with creating and destroying threads.

In our application, we exploited the Labwindows multi-threading capabilities to manage the SMU, defining 3 different threads:

- the ramp up and ramp down functions, invoked to change the test voltage;
- the sensing function, invoked immediately after a voltage ramp up or down.

Besides these, there is another implicit thread, which performs the GUI and the DAQ management and put (remove) the SMU thread into (from) the thread pool. For this purpose, we used the following binary flags:

- *SMU ramp* that, if asserted, indicates a voltage ramp is in progress;
- *SMU sensing* that, if asserted, indicated the SMU has to perform high accuracy measurements;
- *emergency stop* that, if asserted, indicates the output of the SMU must be disabled.

SMU thread functions flowcharts are showed in figure (2.22) and (2.23). Ramp up and ramp down functions are very similar. The first step is to assert the SMU ramp flag; then a higher NPLC value is set, to have several measures during the voltage ramp. Then there is the iterative procedure for the voltage ramp implementation. The user chooses the set point value and the numbers of steps; the functions computes the voltage increment and checks if the set point is reached: if not, a further control on the emergency stop flag is made. If an emergency stop occurs, the SMU ramp flag is cleared and the thread is removed from the thread pool; otherwise, the current voltage value is incremented by the step voltage, a current and voltage measurement is

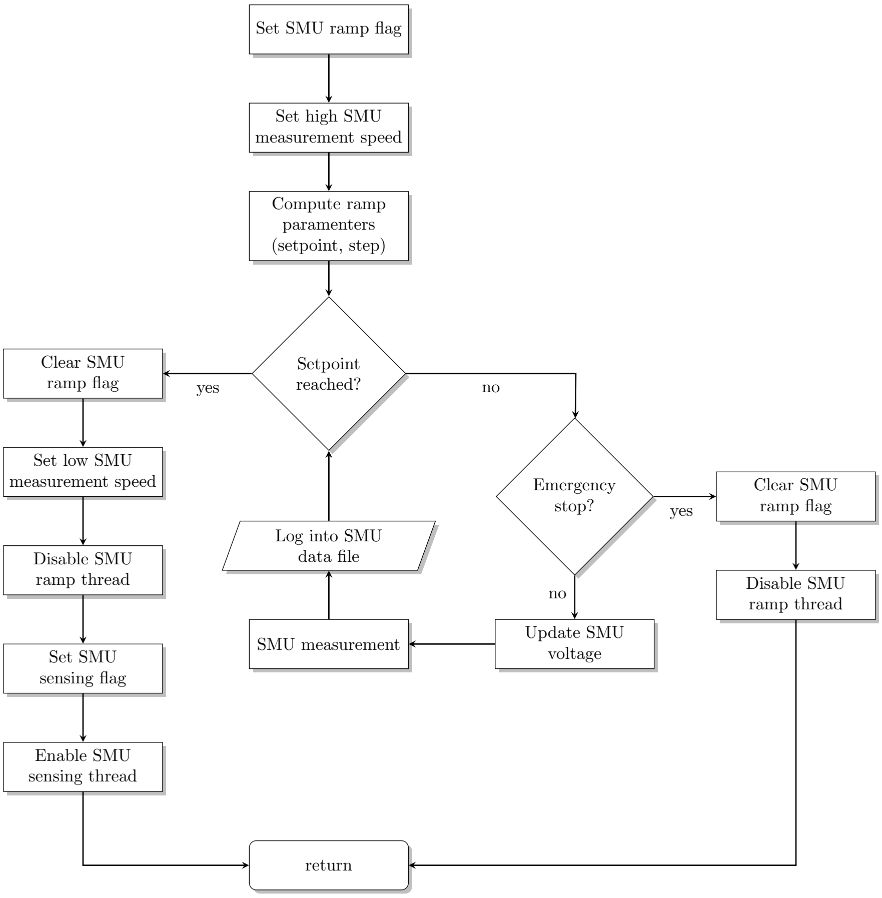

Figure 2.22: SMU ramp up and down threads flowchart

performed by the SMU and these values are plotted into the SMU stripchart and stored into the SMU measurement file. When the set point is reached, the SMU ramp flag is cleared (the voltage ramp is finished), the higher NPLC value is restored and the sensing phase immediately started. This is accomplished removing the ramp thread from the thread pool, asserting the SMU sensing flag and putting the sensing thread into the thread pool.

In the sensing thread, the SMU sensing and emergency stop flags are cyclically checked: if both checks are successful (i.e. sensing flag still asserted and emergency stop flag cleared), the SMU performs a voltage and current measurement; then data are stored to file and visualized into the SMU stripchart; if not, the sensing thread is removed from the thread pool. In the emergency stop case, the function exit is also enforced by clearing the SMU sensing flag.

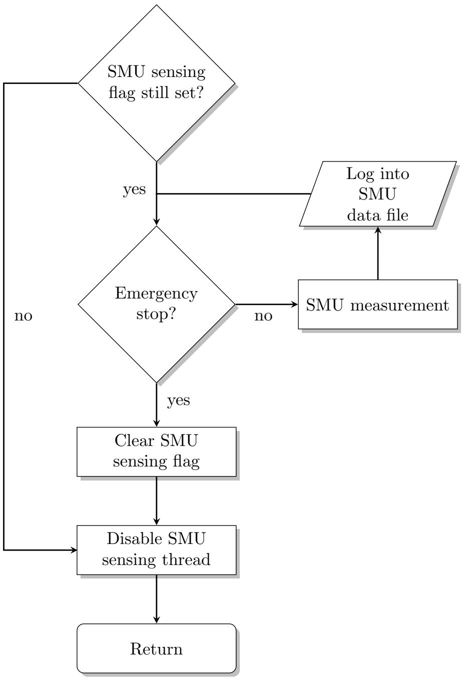

Figure 2.23: SMU sensing thread flowchart

2.6.4 GUI

The GUI is made up of 2 tabs (*Data acquisition* and *Setting parameters*) and a common panel (see figure 2.24). In the Data acquisition tab there is a stripchart for each DUT to visualize, in real-time, the drain voltages temporal evolutions and a special stripchart for the SMU. It displays 3 traces: the effective and the programmed voltage and the supplied current. In addition to the SMU stripchart, there are also 3 numeric indicators for the average values.

The Setting parameters tab is shown in figure 2.25. Here we have several controllers, relating to the DAQ board (input range, measurement configuration, sample rate, buffer size) and SMU parameters (GPIB address, start voltage, ramp time and number of steps, NPLC value, output selection).

The basic elements, placed into the common panel, are the test voltage controller, the measurement files path selector and the *Set Parameters* button, the pressure of which induce the *Init* callback function call. This button is pressed after setting all the DAQ and SMU configuration parameters in the Setting parameters tab, and choosing the measurement files path. After that, all the other buttons are also enabled. More specifically:

- the *Ramp up* button bring the SMU voltage to the test voltage controller value, with a linear ramp and make the DAQ task started;

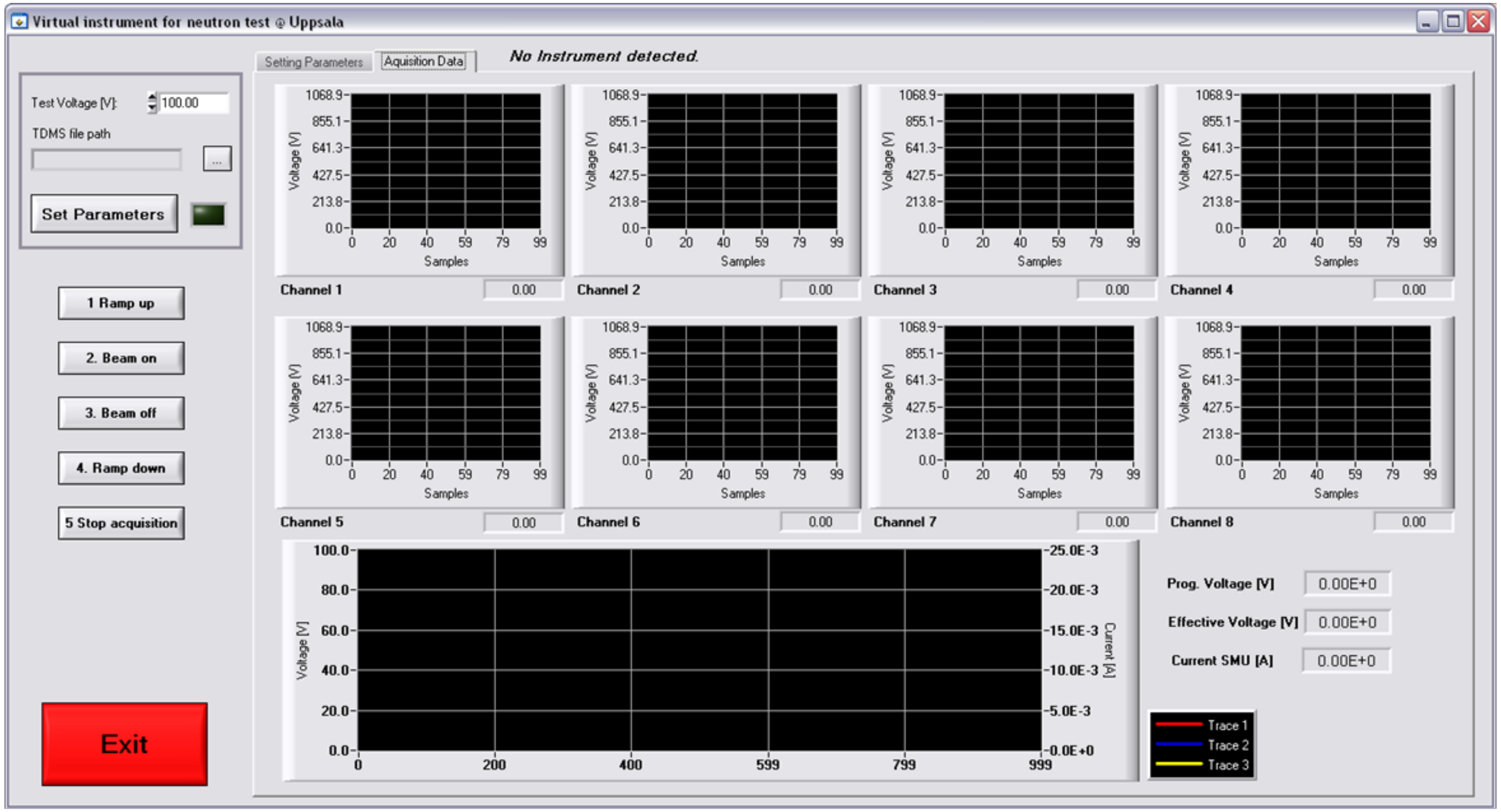

Virtual instrument for neutron test @ Uppsala

No Instrument detected.

Test Voltage [V]: 100.00

Channel 1 0.00

Channel 2 0.00

Channel 3 0.00

Channel 4 0.00

Channel 5 0.00

Channel 6 0.00

Channel 7 0.00

Channel 8 0.00

Prog. Voltage [V] 0.00E+0

Effective Voltage [V] 0.00E+0

Current SMU [A] 0.00E+0

Figure 2.24: Virtual instrument GUI

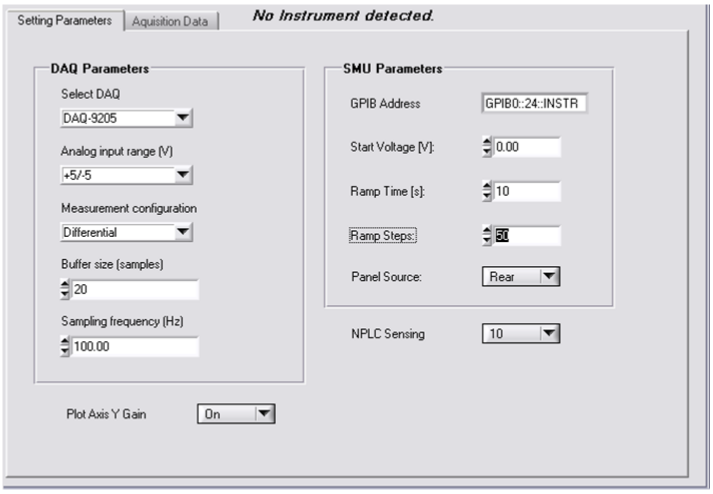

No Instrument detected.

DAQ Parameters

Select DAQ: DAQ-9205
Analog input range (V): +5/-5
Measurement configuration: Differential
Buffer size (samples): 20
Sampling frequency (Hz): 100.00

SMU Parameters

GPIB Address: GPIB0::24::INSTR
Start Voltage [V]: 0.00
Ramp Time [s]: 10
Ramp Steps: 50
Panel Source: Rear

NPLC Sensing: 10

Plot Axis Y Gain: On

Figure 2.25: Setting parameters tab

- the *Beam on* and *Beam off* buttons are used to record the times when exposure respectively begins and finishes;
- the *Ramp down* button bring the SMU voltage to zero with a linear ramp;
- the *Stop acquisition* button stops the DAQ task;
- the *Emergency stop* button shuts down the SMU and exits from the application.

Each of these buttons pressure event is linked to a callback function.

2.6.5 Callback functions

The setting parameter callback flowchart is showed in figure 2.26. The first step is the DAQ board setup, i.e. the task configuration as described in section. Then we have the SMU setup, i.e. the initialization and opening of a VISA session. Finally the SMU and time-stamp files are created.

The ramp up and ramp down callback functions are quite similar (see figure 2.27). Just invoked, they log the ramp time into the time-stamp file. Then, in the ramp up case, the DAQ task is started only if it is not currently running. The next step is the SMU sensing flag clearing: this results in the exit from an eventual sensing thread. Next, the function waits until the SMU ramp flag is cleared to put the ramp up or ramp down thread into the thread pool.

The beam on and beam off callback functions only report the beam on and beam off times into the time-stamp file (see figure 2.28).

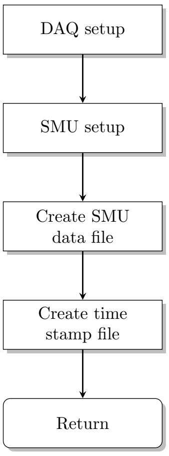

Figure 2.26: Setting parameter callback flowchart

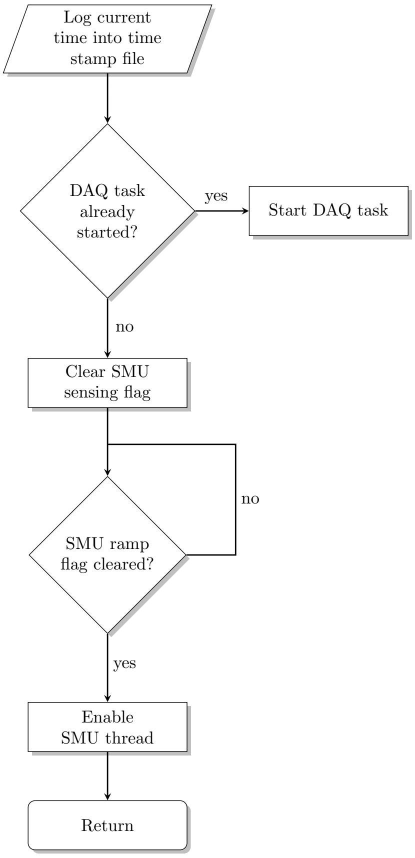

Figure 2.27: SMU ramp up and down callbacks flowchart

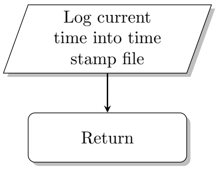

Figure 2.28: Beam on and off callbacks flowchart

The stop acquisition/emergency stop callback functions flowchart is reported in figure 2.29. As in the other callback functions, the first step is the time logging into the time-stamp file. Then the emergency stop flag is asserted, causing the SMU threads exit. Furthermore, the DAQ task is stopped and then cleared. The SMU and the time-stamp files are also closed. Finally, the SMU output is not disable until the SMU ramp and sensing flags are not cleared.

2.7 Statistical analysis of test results

2.7.1 Reliability concepts

Reliability is defined as the probability that an item will perform a required function, under stated conditions, for a stated period of time. Failure is defined as the termination of the ability of an item to perform a required function within previously specified limits, Clearly, reliability reflects the physical performance of products over time and is taken as a measure of their future dependability and trustworthiness. In other terms, the reliability is a measure of the frequency of equipment failures as a function of time.

Various functions are used to statistically describe failures. The probability density function $f(t)$ is the probability that an item will fail between time t and $t + dt$. The cumulative distribution function $F(t)$ is the probability that an item will fail at or before time t. The following relations exits between $f(t)$ and $F(t)$:

$$F(t) = \int_0^t f(t)\, dt \tag{2.6}$$

or

$$f(t) = \frac{dF(t)}{dt} \tag{2.7}$$

It is also clear that:

$$\lim_{t\to\infty} F(t) = 1$$

The reliability function $R(t)$ is the probability that an item will survive to time, therefore it is the ones' complement of $F(t)$:

$$R(t) = 1 - F(t) \tag{2.8}$$

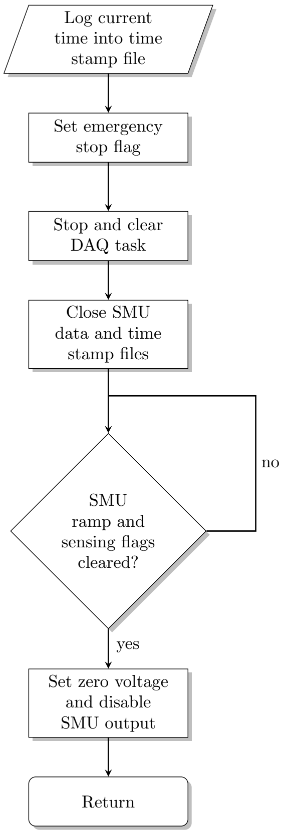

Figure 2.29: Emergency and acquisition stop callbacks flowchart

The *failure* or *hazard rate* λ is the probability that an item will fail between time t and $t + dt$, given that it has survived at time t:

$$\lambda(t) = \frac{f(t)}{1 - F(t)} = \frac{f(t)}{R(t)} \tag{2.9}$$

Since the failure rate is quite low, the unit of Failure In Time (FIT) is used (1 FIT = 1 failure/10^9 hours). This failure rate changes throughout the life of the product according the well-known *bathtub curve*, showed in figure 2.31. It comprises three parts:

1. the first part is a decreasing failure rate, known as *early failures* or *infant mortality*;

2. the second part is a constant failure rate, known as *random failures* or *useful life*;

3. the third part is an increasing failure rate, known as *wear-out failures.*

Another important quantity is the MTTF which can be evaluated as:

$$MTTF = \int_0^\infty t f(t)\, dt \tag{2.10}$$

that is the first-order momentum of the probability density function.

Several statical models are currently used in the microelectronic industry to describe specific failure mechanisms and make lifetime predictions. For example, electro-migration failures usually follow the log-normal distribution while gate oxide breakdown statistics are usually plotted with the Weibull distribution. When the model to be adopted is unknown, one common procedure is to select the probability plotting paper (exponential, Weibull, log-normal, etc.) that allows the data to be graphed as a straight line, but it is not always possible to find an unambiguous model.

For a given test voltage and average flux, the SEB/SEGR probability is constant over the time, so it should be used an exponential model. However, we used the Weibull distribution to take into account eventual cumulative effects due the test facility.

2.7.2 Weibull distribution

In the Weibull distribution function the failure rate varies as a power of the device age. Its probability density function is given by:

$$f(t) = \frac{\beta}{\tau}\left(\frac{t}{\tau}\right)^{\beta-1} \exp\left[-\left(\frac{t}{\tau}\right)^{\beta}\right] \tag{2.11}$$

where τ and β are the scale and the shape parameter, respectively. Consequently, the cumulative distribution function, the reliability function, the failure rate and the MTTF can be expressed as:

$$F(t) = 1 - \exp\left[-\left(\frac{t}{\tau}\right)^{\beta}\right] \tag{2.12}$$

$$R(t) = \exp\left[-\left(\frac{t}{\tau}\right)^{\beta}\right] \tag{2.13}$$

$$\lambda(t) = \frac{\beta}{\tau}\left(\frac{t}{\tau}\right)^{\beta-1} \tag{2.14}$$

$$MTTF = \tau\mathit{\Gamma}\left(1 + \frac{1}{\beta}\right) \tag{2.15}$$

where $\mathit{\Gamma}$ is the gamma function, defined as follows:

$$\mathit{\Gamma}(z) = \int_0^{\infty} t^{z-1}e^{-t}\,dt$$

Depending on the scale parameter value, the Weibull model describes a specific portion of the well-known bathtub curve, representing the failure rate versus time. In fact:

- for $\beta < 1$, failure rate decreases with time;
- for $\beta = 1$, failure rate is constant;
- for $\beta > 1$, failure rate increases with time.

This is more clearly showed into figure, where different Weibull probability distribution functions are plotted with different *beta* values.

2.7.3 Failure rate and MTTF estimation

As explained in section, our test equipment was designed to perform a destructive SEB test. Instead of counting pulses, we continuously monitored the drain voltages of the DUT. A SEB event was identified by the abrupt drain voltage collapse for the failed DUT. In order to make failure rate and MTTF estimations, we first evaluated the failure times t_1, t_2, $\cdots$, t_N; subsequently, we calculated the empirical cumulative function $\hat{F}(t)$, i.e. a discrete function that jumps up by $1/N$ at each of the N data points (see also table 2.4). Then we plotted and fitted data with 2.12), using the Levenberg/Marquard method. Finally we obtain β and τ that we use to compute the failure rate and the MTTF using (2.14) and (2.15).

It should be noted that SEB events are assimilable to random failures; therefore, in the ideal case, the curve fitting with the Weibull model should

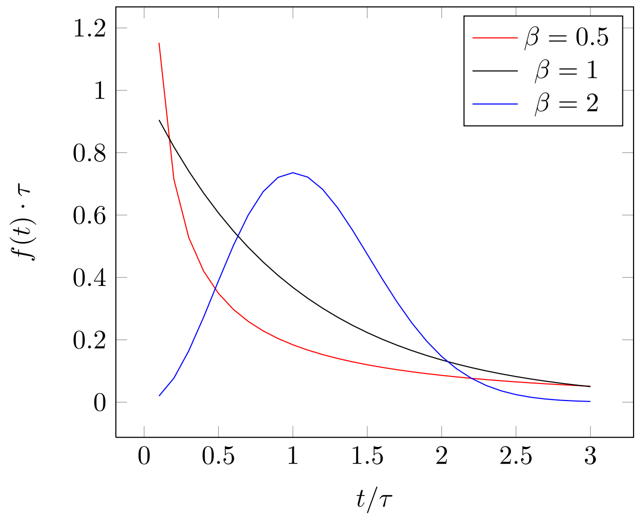

Figure 2.30: Weibull probability distribution functions with different β values

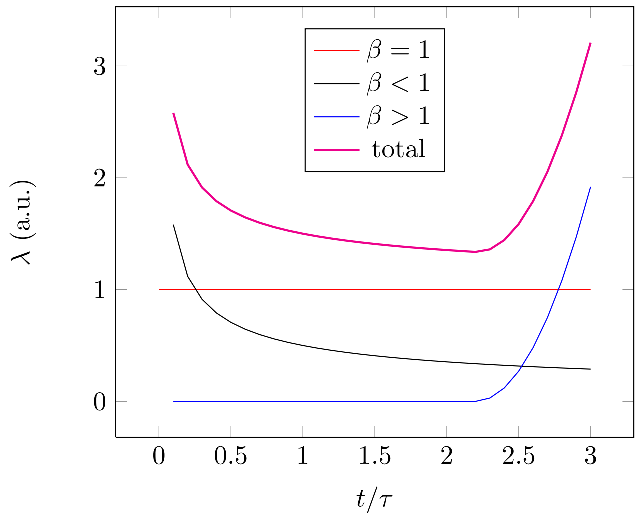

Figure 2.31: Bathtub curve obtained with the superimposition of the Weibull failure rate curves, having $\beta < 1$ (infant mortality), $\beta = 1$ (useful life) and $\beta > 1$ (wear-out)

t	$\hat{F}(t)$
t_1	$1/N$
t_2	$2/N$
$\vdots$	$\vdots$
t_N	1

Table 2.4: Empirical cumulative probability distribution function values

give $\beta = 1$, i.e. a constant failure rate. We could directly use the exponential model, but we used the β parameter to detect possible ageing situations, due to cumulative damages and/or degradations, pulsed neutron irradiation effects and so on.

Goodness of fit

In order to estimate how well the Weibull model fits our experimental data sets, several quantities can be used. The total sum of squares (SST), is a measure of variation of the dependent values y_i around the mean $\bar{y}$:

$$SST = \sum_{i=0}^{N-1} (y_i - \bar{y})^2 \tag{2.16}$$

where N is the total number of experimental points. The total sum of squares can be subdivided into explained variation (or regression sum of squares, SSR), that is attributable to the relationship between the independent variable and the dependent variable, and unexplained variation (or error sum of squares, SSE), that which is attributable to factors other than the relationship between the independent variable and the dependent variable. The regression sum of squares is computed as the sum of squared differences between the fitted values $\hat{y}_i$ and the mean value $\bar{y}$:

$$SSR = \sum_{i=0}^{N-1} (\hat{y}_i - \bar{y})^2 \tag{2.17}$$

while the error sum of squares is the sum of squared differences between the dependent and fitted values respectively:

$$SSE = \sum_{i=0}^{N-1} (y_i - \hat{y}_i)^2 \tag{2.18}$$

A comprehensive parameter for the goodness of fit estimation is the *coefficient of determination*, R^2 , defined as the proportion of the total sample variability explained by the regression:

$$R^2 = \frac{SSR}{SST} = 1 - \frac{SSE}{SST} \tag{2.19}$$

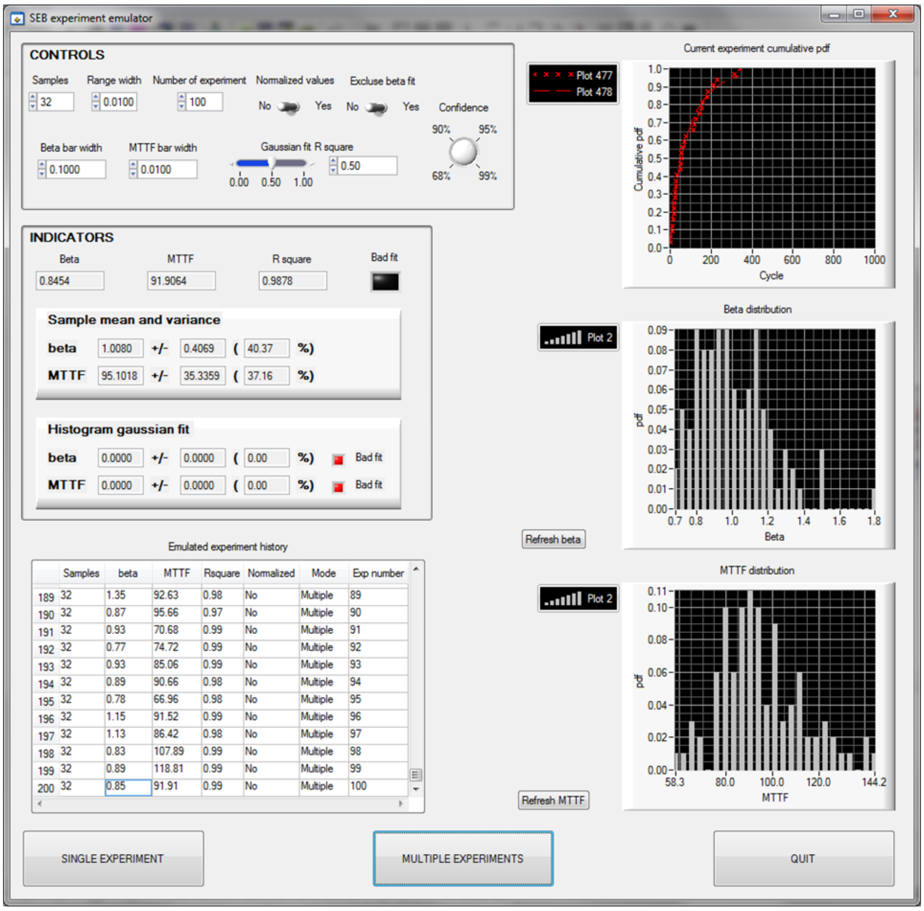

SEB experiment emulator

CONTROLS

Samples: 32

Range width: 0.0100

Number of experiment: 100

Normalized values: No / Yes

Excluse beta fit: No / Yes

Beta bar width: 0.1000

MTTF bar width: 0.0100

Gaussian fit R square: 0.50

INDICATORS

Beta: 0.8454

MTTF: 91.9064

R square: 0.9878

Sample mean and variance

beta 1.0080 +/- 0.4069 (40.37 %)

MTTF 95.1018 +/- 35.3359 (37.16 %)

Histogram gaussian fit

beta 0.0000 +/- 0.0000 (0.00 %) Bad fit

MTTF 0.0000 +/- 0.0000 (0.00 %) Bad fit

Emulated experiment history

	Samples	beta	MTTF	Rsquare	Normalized	Mode	Exp number
189	32	1.35	92.63	0.98	No	Multiple	89
190	32	0.87	95.66	0.97	No	Multiple	90
191	32	0.93	70.68	0.99	No	Multiple	91
192	32	0.77	74.72	0.99	No	Multiple	92
193	32	0.93	85.06	0.99	No	Multiple	93
194	32	0.89	90.66	0.98	No	Multiple	94
195	32	0.78	66.96	0.98	No	Multiple	95
196	32	1.15	91.52	0.99	No	Multiple	96
197	32	1.13	86.42	0.98	No	Multiple	97
198	32	0.83	107.89	0.99	No	Multiple	98
199	32	0.89	118.81	0.99	No	Multiple	99
200	32	0.85	91.91	0.99	No	Multiple	100

Figure 2.32: Labwindows SEB emulator GUI

And it follows that:

$$0 \leq R^2 \leq 1$$

Therefore, the coefficient of determination gives the proportion of the total variation in the dependent variable explained by the independent variable: the closer R^2 to 1, the better is the fit.

Sample size and uncertainty

Without the circumvention techniques, many samples are required to perform a characterization test. Of course, the more the samples, the higher the accuracy of MTTF and failure rate estimations. One may ask how many samples are needed to obtain the desired accuracy with the experimental procedure described so far. To answer this question, we developed a Labwindows application to emulate a SEB experiment. Each neutron interaction is represented by a random number generation, between 0 and 1. An integer

N_{DUT}	$\Delta\beta$ (%)	$\Delta MTTF$ (%)
8	30.6	37.5
16	24.8	27.7
32	18.6	19.2
64	12.1	14.0
128	8.6	9.7
256	5.9	6.6
512	4.2	4.9
1024	3.0	3.4

Table 2.5: β and MTTF percentage uncertainty versus the sample size, with a confidence limit of 68%

counter is incremented after each trial. If the random number falls within a user-selected range (centred on 0.5), a SEB occurs and the actual counter value represent the failure time. Subsequently, the counter is reset and this procedure repeated as many times as the number of DUT selected by the user. At the end, the emulated data are elaborated as described section 2.7.3: we calculate the empirical cumulative probability distribution function and perform the Weibull curve fitting with the resulting β and τ parameters extrapolation. Note that, having only random failures, a unitary β statistics is imposed. This is the *Single Experiment* operation mode. As the name suggests, the *Multiple experiment* repeat N times the single experiment routine in order to obtain a β distribution. For the central limit theorem, as N increases, the β random variable approaches a Gaussian distribution, whose variance is proportional to the β uncertainty, depending on the confidence level. Typically, this proportional factor can be 2 or 3 for a 95% and 99% confidence level respectively. The MTTF uncertainty can be calculated in the same way. We emulated several sample size combinations: the results are reported into table 2.5.

Bibliography chapter 2

[1] `https://mcnp.lanl.gov/`.

[2] `http://www.ni.com/data-acquisition/compactdaq/`.

[3] `http://sine.ni.com/nips/cds/view/p/lang/en/nid/208800`.

[4] `http://www.keithley.com/products/dcac/currentvoltage/?mn=2410`.

[5] M. Allenspach et al. "Evaluation of SEGR threshold in power MOSFETs". In: *Nuclear Science, IEEE Transactions on* 41.6 (Dec. 1994), pp. 2160–2166. ISSN: 0018-9499. DOI: `10.1109/23.340557`.

[6] G. Consentino et al. “Dangerous effects induced on power MOSFETs by terrestrial neutrons: A theoretical study and an empirical approach based on accelerated experimental analysis”. In: *AEIT Annual Conference, 2013.* Oct. 2013, pp. 1–6. DOI: `10.1109/AEIT.2013.6666813`.

[7] *DAQ E Series User Manual.* National Instruments, 2008.

[8] J. van Duivenbode and B. Smet. “An empiric approach to establishing MOSFET failure rate induced by Single-Event Burnout”. In: *Power Electronics and Motion Control Conference, 2008. EPE-PEMC 2008. 13th.* Sept. 2008, pp. 102–107. DOI: `10.1109/EPEPEMC.2008.4635251`.

[9] V. Ferlet-Cavrois et al. “Influence of Beam Conditions and Energy for SEE Testing”. In: *Nuclear Science, IEEE Transactions on* 59.4 (Aug. 2012), pp. 1149–1160. ISSN: 0018-9499. DOI: `10.1109/TNS.2012.2187681`.

[10] *Instrument control in Labwindows/CVI Tutorial.* National Instruments, 2009.

[11] *Introduction to the Labwindows/CVI TDM Streaming library.* National Instruments, 2012.

[12] *JESD89A: Measurement and reporting of alpha particle and terrestrial cosmic ray induced soft errors in semiconductor device.* Standard Rev. A. JEDEC Solid State Technology Association, 2006.

[13] G.H. Johnson et al. “A physical interpretation for the single-event-gate-rupture cross-section of n-channel power MOSFETs”. In: *Nuclear Science, IEEE Transactions on* 43.6 (Dec. 1996), pp. 2932–2937. ISSN: 0018-9499. DOI: `10.1109/23.556888`.

[14] G.H. Johnson et al. “A review of the techniques used for modeling single-event effects in power MOSFETs”. In: *Nuclear Science, IEEE Transactions on* 43.2 (Apr. 1996), pp. 546–560. ISSN: 0018-9499. DOI: `10.1109/23.490900`.

[15] R. Koga. “Single-event effect ground test issues”. In: *Nuclear Science, IEEE Transactions on* 43.2 (Apr. 1996), pp. 661–670. ISSN: 0018-9499. DOI: `10.1109/23.490909`.

[16] *Labwindows/CVI. Getting started with Labwindows/CVI.* National Instruments, 2012.

[17] *Learn 10 Functions in NI-DAQmx and Handle 80 Percent of Your Data Acquisition Applications.* National Instruments, 2012.

[18] S. Liu et al. “Evaluation on Protective Single Event Burnout Test Method for Power DMOSFETs”. In: *Nuclear Science, IEEE Transactions on* 59.4 (Aug. 2012), pp. 1125–1129. ISSN: 0018-9499. DOI: `10.1109/TNS.2011.2177863`.

[19] S. Liu et al. “Recommended Test Conditions for SEB Evaluation of Planar Power DMOSFETs”. In: *Nuclear Science, IEEE Transactions on* 55.6 (Dec. 2008), pp. 3122–3129. ISSN: 0018-9499. DOI: `10.1109/TNS.2008.2006841`.

[20] S. Liu et al. “Single-Event Burnout and Avalanche Characteristics of Power DMOSFETs”. In: *Nuclear Science, IEEE Transactions on* 53.6 (Dec. 2006), pp. 3379–3385. ISSN: 0018-9499. DOI: `10.1109/TNS.2006.884971`.

[21] *Multi-threading in Labwindows/CVI.* White Paper. National Instruments, 2012.

[22] D.K. Nichols et al. “Observations of single event failure in power MOSFETs”. In: *Radiation Effects Data Workshop, 1994 IEEE.* July 1994, pp. 41–54. DOI: `10.1109/REDW.1994.633035`.

[23] D.L. Oberg and J.L. Wert. “First Nondestructive Measurements of Power MOSFET Single Event Burnout Cross Sections”. In: *Nuclear Science, IEEE Transactions on* 34.6 (Dec. 1987), pp. 1736–1741. ISSN: 0018-9499. DOI: `10.1109/TNS.1987.4337546`.

[24] M. Ohring. *Reliability and Failure of Electronic Material and Device.* "Academic Press", 1998. Chap. 4.

[25] E.L. Petersen. “Single-Event Data Analysis”. In: *Nuclear Science, IEEE Transactions on* 55.6 (Dec. 2008), pp. 2819–2841. ISSN: 0018-9499. DOI: `10.1109/TNS.2008.2007903`.

[26] AV. Prokofiev et al. “Characterization of the ANITA Neutron Source for Accelerated SEE Testing at The Svedberg Laboratory”. In: *Radiation Effects Data Workshop, 2009 IEEE.* July 2009, pp. 166–173. DOI: `10.1109/REDW.2009.5336295`.

[27] D.K. Schroeder. *Semiconductor Material and Device Characterization.* "John Wiley and Sons", 2006. Chap. 12.

[28] J.R. Schwank, M.R. Shaneyfelt, and P.E. Dodd. *Radiation Hardness Assurance Testing of Microelectronic Devices and Integrated Circuits: Test Guideline for Proton and Heavy Ion Single Event Effects.* 2008. URL: `http://www.sandia.gov/mstc/services/documents/Sandia_SEE_Guideline_FINAL.pdf`.

[29] F.W. Sexton. “Destructive single-event effects in semiconductor devices and ICs”. In: *Nuclear Science, IEEE Transactions on* 50.3 (June 2003), pp. 603–621. ISSN: 0018-9499. DOI: `10.1109/TNS.2003.813137`.

[30] *STD MIL 750 E: Test methods for semiconductor devices.* method 1080. USA Department of Defence, 2011.

[31] P. Tastet et al. “Burnout sensitivity of power MOSFETs operating in a switching converter”. In: *Nuclear Science, IEEE Transactions on* 41.3 (June 1994), pp. 583–588. ISSN: 0018-9499. DOI: `10.1109/23.299803`.

[32] J.L. Titus. “An Updated Perspective of single event gate rupture and single event burnout in Power MOSFETs”. In: *Nuclear Science, IEEE Transactions on* 60.3 (June 2013), pp. 1912–1928. ISSN: 0018-9499. DOI: `10.1109/TNS.2013.2252194`.

[33] J.L. Titus and C.F. Wheatley. “Experimental studies of single-event gate rupture and burnout in vertical power MOSFETs”. In: *Nuclear Science, IEEE Transactions on* 43.2 (Apr. 1996), pp. 533–545. ISSN: 0018-9499. DOI: `10.1109/23.490899`.

[34] *Using the DAQ Assistant in Labwindows/CVI.* National Instruments, 2007.

Chapter 3

Experiments

Contents

This chapter describes the accelerated experiments performed with the ANITA and UniPA neutron facilities. Test plan, data elaboration and experimental results will be discussed.

3.1 ANITA experiment

The aim of the ANITA experiment was to assess the terrestrial neutron hardness of several Commercial Of The Shelf (COTS) power transistors, typically used into photovoltaic inverters. Thanks to the spectral characteristics of the facility, we reproduced the irradiation conditions equivalent to 25 years[1] of exposure to fast terrestrial neutrons at the sea level and 2000 m altitude. Despite the experiment was designed according to the verification test approach (as referred into the STD MIL 750 E), for different bias voltages, we also tried to calculate the MTTF and the failure rate with the Weibull statistical analysis. However, our estimations are semi-quantitative because, with only 8 samples, the percentage standard deviations of β and MTTF are respectively 30% and 37%. To get a 95% confidence levels, these values have

---

[1] the typical lifetime of a photovoltaic panel

Device	Description	Package	Die size
2M6L	MOS 600 V MDMesh II, standard generation	TO-247	0.49
2F6L	MOS 600 V Fast diode MDMesh II	TO-247	0.49
M5F9	MOS 650 V MDMesh V, standard generation	TO-247	1.00
VJ8L	MOS 800 V SuperMesh, newest generation	TO-220	0.49
VJLL	MOS 950 V SuperMesh, newest generation	TO-220	0.49
EIF7	IGBT 650 V TFS	TO-247	0.44
EIJ7	IGBT 1200 V V TFS	TO-247	0.41

Table 3.1: List of DUT for the ANITA experiment. Die size values are normalized

to be multiplied by a factor of 2. Moreover, having a set point fluence, the experiments didn't last until the failure of all the samples, implying a higher uncertainty.

3.1.1 DUT

Two families of ST Microelectronics power transistors, with different technologies, packages and breakdown voltages, were tested: High Voltage (HV) Super Junction (SJ) power MOSFETs and Trench Field Stop (TFS) IGBTs. The complete list of DUTs is shown in table 3.1. A brief description is as follows. Regarding power MOSFETs, M5F9, 2M6L and 2F6L belong to the MDMesh technology, a particular implementation of SJ. 2M6L and 2F6L are identical except for the fact that 2F6L has also an integrated fast diode, suited for high frequency switching applications. The SuperMesh devices have a hybrid technology which combines some of the best SJ and planar features. Moreover, they have higher breakdown voltages compared to SJ standard devices. As for IGBTs, EIF7 and EIJ7 differ in breakdown voltages (650 V and 1200 V, respectively).

A 24 h high temperature burn-in test was carried out for all DUTs to prevent possible early failures due infant mortality.

3.1.2 Test plan

As suggested by the STD MIL 750 E, an appropriate SEB prediction method should be used to predict the SEB failure thresholds and to properly establish the selection of initial bias conditions. The preferred method is to use previous measurements: not having them, we used part of the resources

Alias	ϕ (cm^{-2})	d (cm)	f_r (Hz)	t (s)	AF
BC 1	2.8×10^6	250 (SUP)	2	275	2.9×10^6
BC 2	2.5×10^7	250 (SUP)	18	250	2.8×10^7
BC 3	2.8×10^7	250 (SUP)	18	278	2.8×10^7
BC 4	2.8×10^7	700	160	323	2.4×10^7
BC 5	2.8×10^7	700	40	1325	5.9×10^6

Table 3.2: Beam conditions for the ANITA experiment. ϕ is the pre set fluence, d the distance from target, f_r the repetition rate, t the exposure time and AF the acceleration factor

(time machine and samples) to carry out some preliminary runs, in order to have a rough estimation of the SEB thresholds and use these values as initial bias conditions for the validation runs. In the preliminary runs we made cumulative exposures on the same DUTs, with gradually increasing test voltages, up to the first failures. In this manner we saved a lot of time, because the samples replacement implies to access into the blue hall, with all the clearing security procedures. Some samples were preserved, stopping the irradiation before the pre set fluence, to allow the post irradiation electrical characterization, in order to detect any cumulative effects.

Regarding the fluence values, JES89A standard states the fast neutron flux above 10 MeV in the reference conditions (New York City, outdoor, sea level, time of average solar activity) is $3.6\,\mathrm{cm}^{-2}\,\mathrm{s}^{-1}$; multiplying this value by 7.8×10^8 s (25 years conversion into seconds) we obtain $2.8 \times 10^6\,\mathrm{cm}^{-2}$. The neutron flux at 2000 m is almost ten times greater than at the sea level: therefore the fluence is $2.8 \times 10^7\,\mathrm{cm}^{-2}$.

The preliminary runs consist of the repetition of a mini-sequence of 2 exposures, having the same test voltage and fluence values of $2.8 \times 10^6\,\mathrm{cm}^{-2}$ and $2.5 \times 10^7\,\mathrm{cm}^{-2}$ respectively (the total fluence is $2.8 \times 10^7\,\mathrm{cm}^{-2}$). Besides the pre set fluence, other beam parameters need to be chosen, such as the distance from target, the beam shape and the repetition rate. Each one affects the average neutron flux and then the exposure time and the acceleration factor. In fact, the neutron beam arrives in the user area through a cylindrical opening in a 1 m iron wall and diverges as a cone: thus the samples intercept a lower amount of neutrons with increasing distances. The divergence depends upon the aperture diameter. The repetition rate refers to the temporal structure of the proton primary beam, which generates neutrons as described in the section 2.4.1. The control signal of the proton beam is a train of pulses, having the same amplitude and width. The emission of neutrons occurs during the on period of each pulse, then the average neutron flux is linked to the frequency of this signal, i.e. the repetition rate. In particular, the higher is the repetition rate, the higher is the flux.

As the distance from the target we started with the SUP (250 cm): considering the physical size of the DUT board and the beam uniformity requirement (less than 5%), we used a cylindrical collimator, with a diameter of 10.2 cm. To validate this solution, we requested a beam profile measurement (see figure), obtaining a plateau region diameter of 12.6 cm. This measurement was performed with a Thin Film Breakdown Counter (TFBC) having a fissile target of ^{238}U . The repetition rate was chosen so that the pre set fluence, could be achieved at the SUP in a few minutes: for the verification runs it was 18 Hz, while for the preliminary runs it was 2 Hz (for the lower fluence exposure) and 18 Hz (for the higher fluence exposure). Finally, we tested another two situations:

- increasing the distance from the target (from 250 cm to 700 cm), compensating the repetition rate (from 18 Hz to 160 Hz) to maintain approximately the same average flux;
- increasing the distance to the target and the exposure time, with a repetition rate of 40 Hz.

We requested the beam profile characterization in the new position too: in this case, the plateau region had a diameter of 29.8 cm. The experimental beam conditions are listed in table 3.2, while the run list is in table 3.3.

3.1.3 Results and discussion

Several failures were observed during the experiments. In the failed DUTs, post irradiation electrical characterizations evidenced a strong increase in both I_{dss} and I_{gss} leakage currents, as their drain and source contacts were practically shorted. On the other side, no significant variations were noticed into electrical parameters of survived DUTs. For each experiment, we recorded the failure times, calculate the cumulative empirical functions and performed a curve fitting (see figures 3.1-3.11), as described into section 2.7.3, in order to evaluate the β and τ parameters of the Weibull model. For some runs, this was not possible because of less than 3 failures, i.e. the minimum number of failures required to have at least 1 degree or freedom, defined as the difference between the number of experimental points to be fitted and the number of parameters of the fitting function. Despite the β values are different from 1, this does not mean that the experiments are not characterized by a constant failure rate: the β variability can be explained with a quite big uncertainty due the small sample size. The experiments with β values outside the uncertainty range were rejected. Furthermore, for the accepted experiments we compute the MTTF and the failure rate as if they have a β equal to 1.

SEB threshold voltages were determined by computing the arithmetic average between the highest test voltage with no failures and the lowest test

#	Device	V_t ($\%BV_{dss}$)	N_{failed}	BC	β	MTTF (y)	λ (FIT)
1	2M6L	70	0	2	n/d	n/d	n/d
2	2M6L	80	4	3	1.2	247.5	4.6×10^2
3	2M6L	80	4	4	0.7	157.0	7.2×10^2
4	2M6L	80	5	5	0.7	187.6	6.8×10^2
5	2F6L	70	0	1	n/d	n/d	n/d
6	2F6L	80	6	3	1.2	95.9	1.2×10^3
7	2F6L	80	4	4	1.5	111.6	1.0×10^3
8	M5F9	60	0	1	n/d	n/d	n/d
9	M5F9	70	5	3	0.4	32.3	3.5×10^3
10	M5F9	80	8	2	1.0	7.4	1.5×10^4
11	VJ8L	70	0	1	n/d	n/d	n/d
12	VJ8L	75	5	2	1.1	25.1	4.5×10^3
13	VJ8L	75	2	4	n/d	n/d	n/d
14	VJ8L	75	4	4	0.8	289.9	3.9×10^2
15	VJ8L	80	8	3	0.7	35.2	3.2×10^3
16	VJLL	60	0	1	n/d	n/d	n/d
17	VJLL	70	2	3	n/d	n/d	n/d
18	VJLL	80	7	2	1.9	26.8	4.2×10^3
19	VJLL	82.5	7	3	1.7	23.2	4.9×10^3
20	EIF7	70	0	3	n/d	n/d	n/d
21	EIF7	80	0	3	n/d	n/d	n/d
22	EIF7	90	6	3	1.4	30.0	3.8×10^3
23	EIF7	100	5	2	1.7	2.4	4.8×10^4
24	EIJ7	60	0	1	n/d	n/d	n/d
25	EIJ7	70	2	3	n/d	n/d	n/d
26	EIJ7	80	8	2	1.3	38.7	2.9×10^3

Table 3.3: Run list. V_t is the test voltage expressed in percentage with respect the DUT breakdown voltage, N_{failed} is the number of failures, BC is the beam condition (refer to table 3.2), β is the shape parameter of the Weibull function, λ is the failure rate in FIT

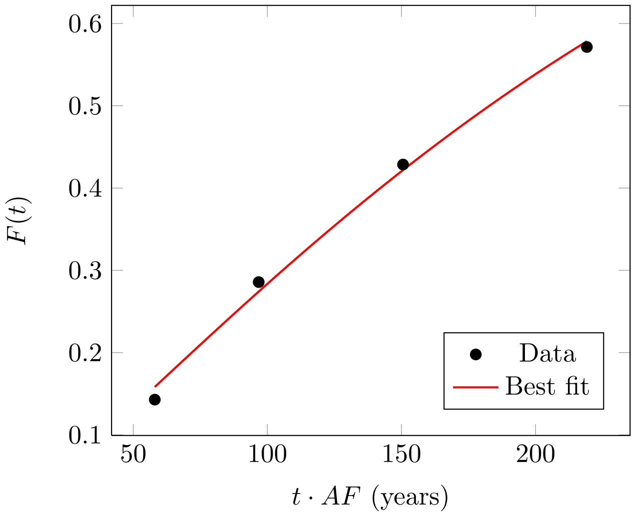

Figure 3.1: Weibull fit with the experimental data of the run 2. See table 3.3 for further details

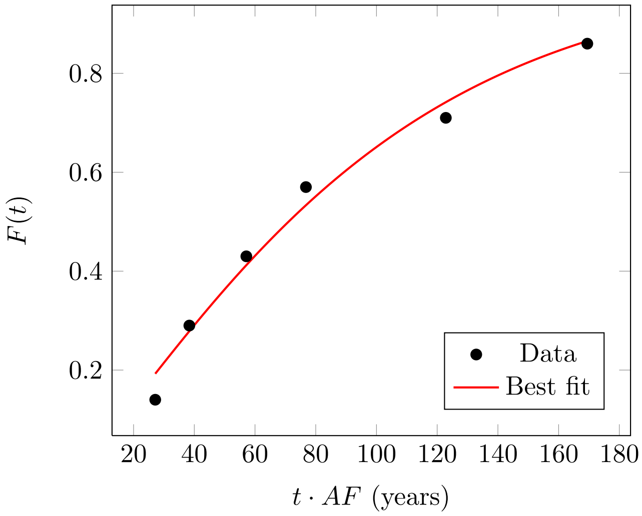

Figure 3.2: Weibull fit with the experimental data of the run 6. See table 3.3 for further details

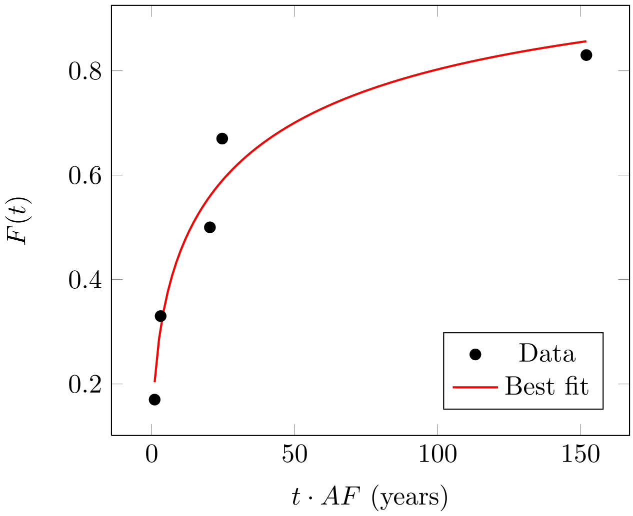

Figure 3.3: Weibull fit with the experimental data of the run 9. See table 3.3 for further details

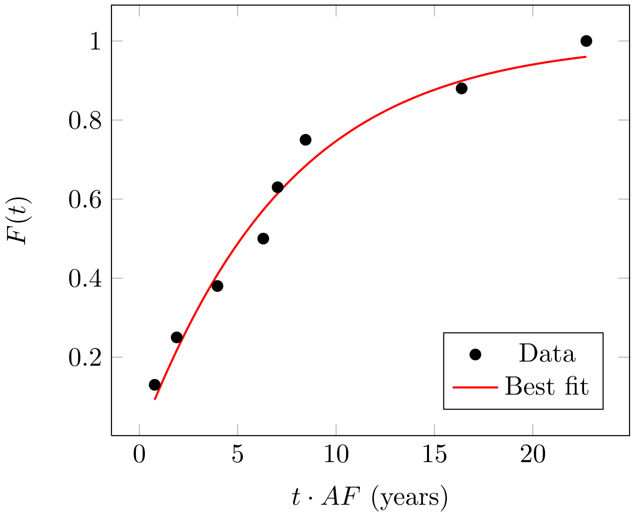

Figure 3.4: Weibull fit with the experimental data of the run 10. See table 3.3 for further details

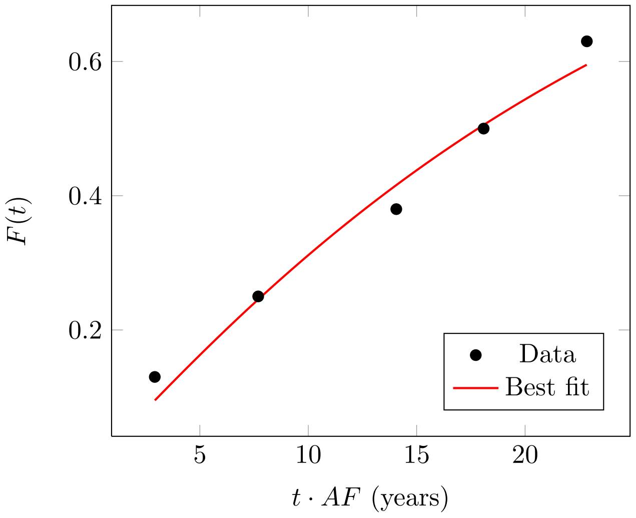

Figure 3.5: Weibull fit with the experimental data of the run 12. See table 3.3 for further details

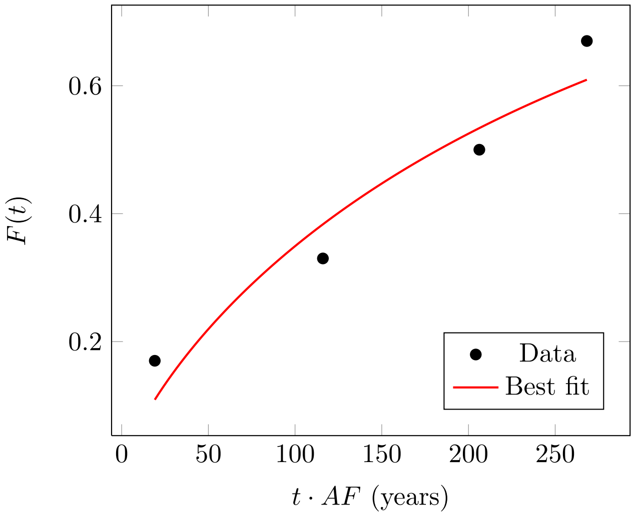

Figure 3.6: Weibull fit with the experimental data of the run 14. See table 3.3 for further details

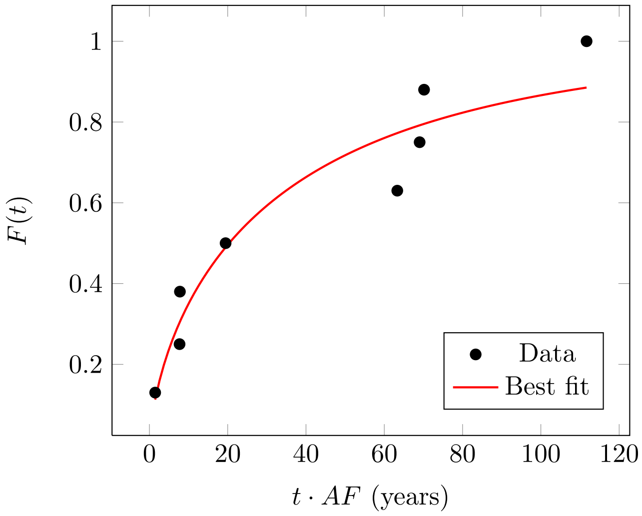

Figure 3.7: Weibull fit with the experimental data of the run 15. See table 3.3 for further details

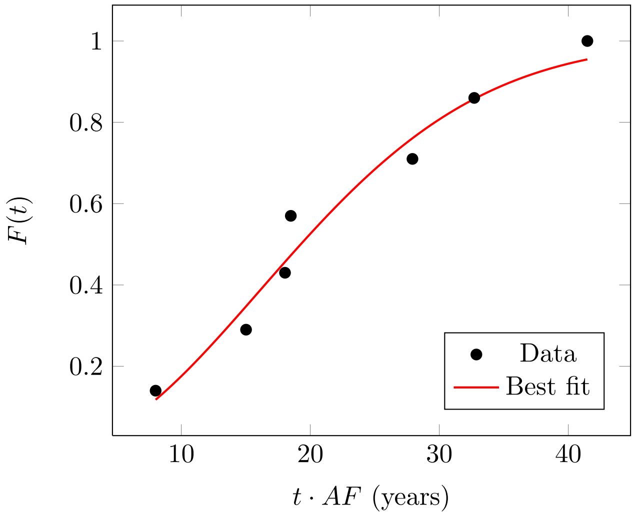

Figure 3.8: Weibull fit with the experimental data of the run 18. See table 3.3 for further details

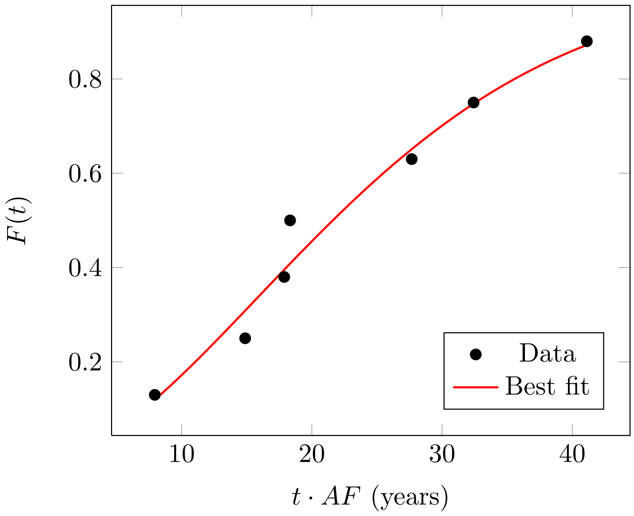

Figure 3.9: Weibull fit with the experimental data of the run 19. See table 3.3 for further details

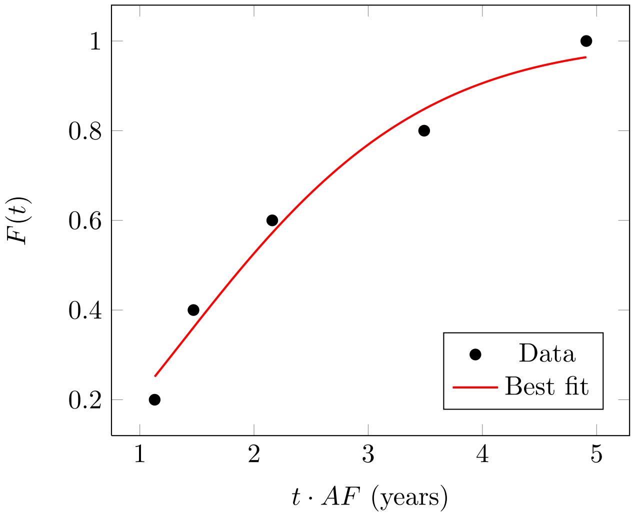

Figure 3.10: Weibull fit with the experimental data of the run 23. See table 3.3 for further details

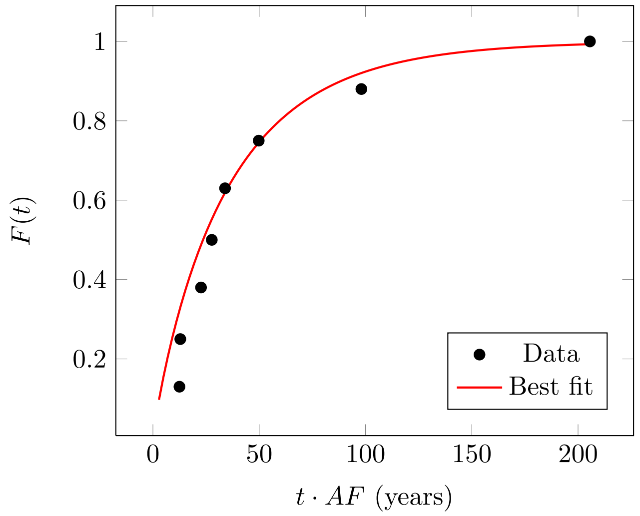

Figure 3.11: Weibull fit with the experimental data of the run 26. See table 3.3 for further details

voltage with failures. In order to make a qualitative comparison between the different DUT, we expressed their SEB thresholds in breakdown voltages percentages, as in figure 3.12. The most reliable device is the EIF7, with a percentage threshold of 85%; among the power MOSFETs we have the 2M6L and 2F6L (the fast diode inclusion seems not to be relevant), with a percentage threshold of 72.5%. However, to ensure the SEB immunity for voltages up to 600 V, we have to choose higher breakdown voltage devices such as the VJLL or EIJ7, with a resulting performance worsening in terms of on-resistance, although they have a lower SEB threshold percentage.

We also compared the failure rate of the different DUT, considering the same beam conditions and a test voltage equal to the 15% more than the SEB threshold percentage (see figure 3.13). Also in this case, the most performing device is the EIF7.

Finally, failure rate comparison among the experiment performed with the same DUT, the same test voltage, but different beam conditions (e.g. run 2,3 and 4, with beam conditions 3,4 and 5 and run 6,7 with beam conditions 3 and 4), indicate that the beam position and the repetition rate variations don't affect the previous results.

3.1.4 Post-failure analysis

The post-failure analysis was carried out by the characterization laboratory of ST Microelectronics in Catania. The microscope inspection clearly evidenced burnout point sites, with a random distribution over the entire active area of the devices, as it is possible to see in figures 3.14-3.19. Parallel

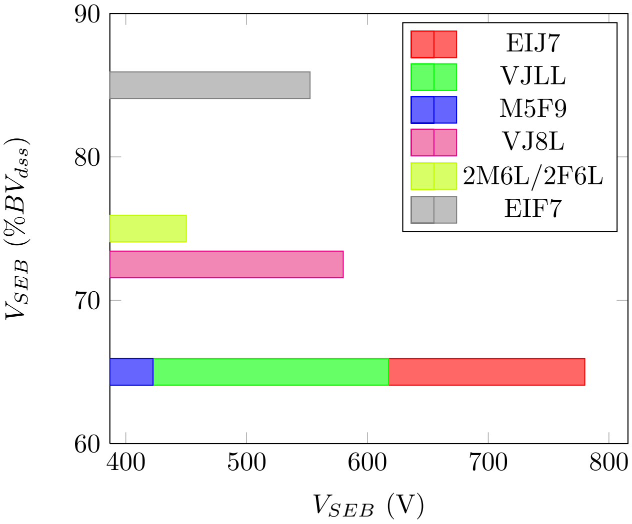

Figure 3.12: SEB percentage thresholds versus their corresponding absolute values. Note that, due the different breakdown voltages, the same threshold percentage of 2 different DUT gives 2 different absolute values

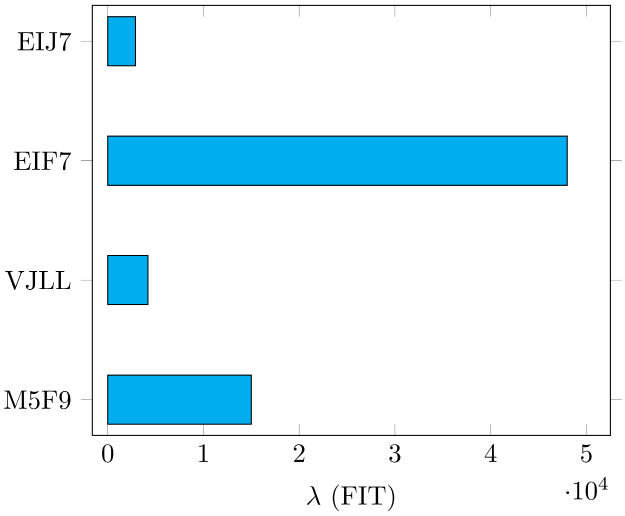

Figure 3.13: Failure rate comparison among several DUT (run 10, 18, 23 and 26)

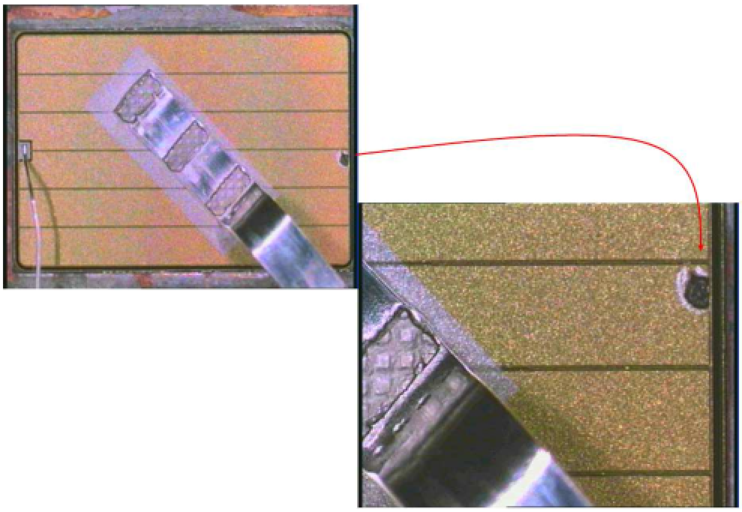

Figure 3.14: Microscope view of a failed sample of M5F9

capacitors (see section 2.5.2) were suited to induce SEB traces large enough to be identified with a simple visual inspection, without resorting to more sophisticated techniques, such as the liquid crystal treatment, or the Focused Ion Beam (FIB). The typical diameter of SEB trace is about 100 µm.

3.2 UniPA experiment

The purpose of this experiment was to verify the possibility of using Am-Be neutron sources for engineering tests of radiation hardness evaluation. In the ANITA experiment, we observed several SEB events with test voltage well below the maximum rated breakdown; we wanted to see whether the same phenomena could be observed with a less energetic neutron source, such as the UniPA, as well. In fact, even though the spallation sources can replicate the terrestrial neutron spectrum for energies higher than 1 MeV (thus providing a greater trustworthiness for test results), they are quite expensive in terms of beam time fee, because of the proton accelerator usage. Moreover, there is only another neutron spallation facility in Europe, aside ANITA, i.e. ISIS at Rutherford Appleton Laboratory in Oxfordshire (United Kingdom). On the contrary, the Am-Be neutron sources are quite cheap and can be also installed in small laboratories, provided an adequate radiation shielding.

With regard to the UniPA facility, the maximum neutron energy is 11 MeV, i.e. one order of magnitude lower than ANITA. Nevertheless, the 1 to 11 MeV range, represents about 40% of the total flux of fast terrestrial neutrons, according to the standard JESD89A. The UniPA source has also an important component of thermal neutrons.

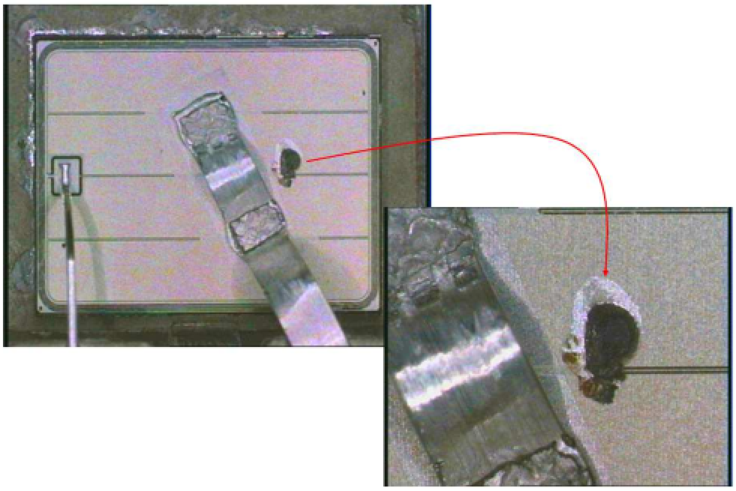

Figure 3.15: Microscope view of a failed sample of VJLL

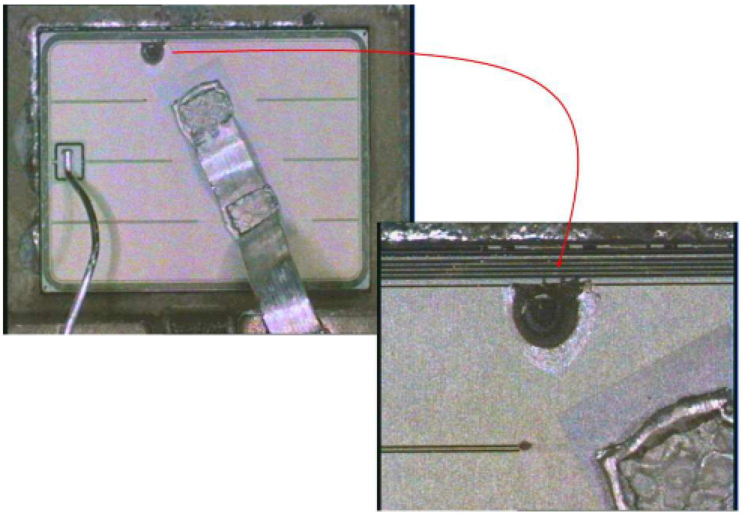

Figure 3.16: Another microscope view of a failed sample of VJLL

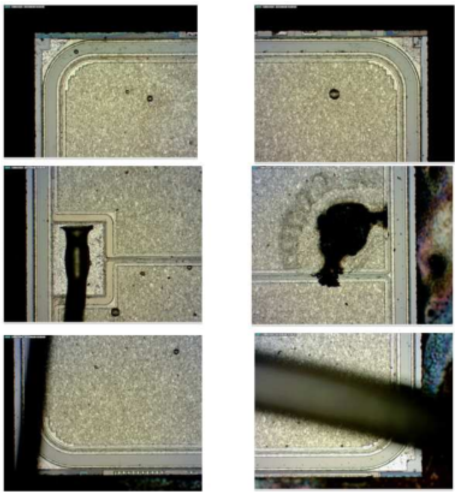

Figure 3.17: Microscope view of a failed sample of EIF7

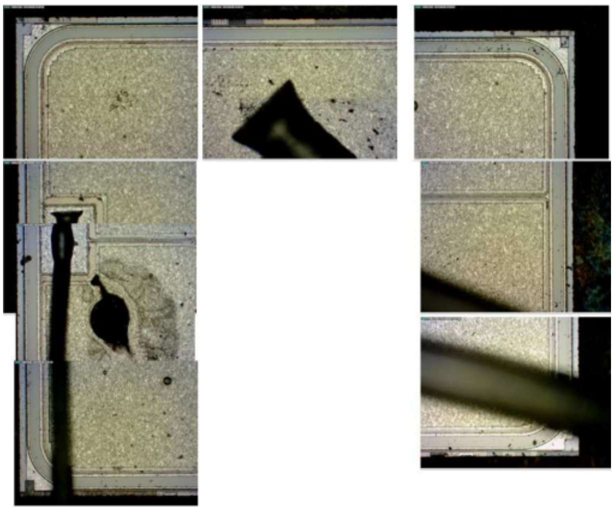

Figure 3.18: Another microscope view of a failed sample of EIF7

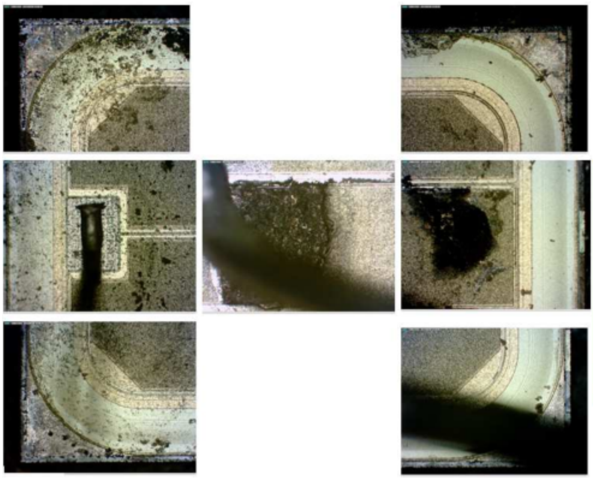

Figure 3.19: Microscope view of a failed sample of EIJ7

#	V_t ($\%BV_{dss}$)	N_{failed}	β	MTTF (y)	λ (FIT)
1	80	0	n/d	n/d	n/d
2	85	0	n/d	n/d	n/d
3	95	7	1.4	14.6	7.8×10^3
4	100	16	0.9	3.8	3.0×10^4

Table 3.4: Run list. V_t is the test voltage expressed in percentage with respect the DUT breakdown voltage, N_{failed} is the number of failures, β is the shape parameter of the Weibull function, λ is the failure rate in FIT

3.2.1 Test plan

Tests were carried out exclusively on the VJLL device, because it resulted, from the ANITA experiment, one of the best candidates for photovoltaic applications. Samples were mounted on the DUT board described in section 2.5.3, capable to accommodate up to 8 DUTs.

Being a continuous neutron source, the UniPA switching on and off is not automatic or remotely controlled. Once inserted the DUT inside the irradiator, the experiment started and finished respectively with the bias ramp up and ramp down. Also for this reason we didn't choose a set point fluence as in the ANITA experiment. The experiments lasted as long as all DUTs failed. In same cases we didn't observe any failure even after 1 hour of exposure, so we ended the experiment and started a new one with a higher test voltage. The complete run list is in table 3.4.

Despite the small sample size, we tried to estimate the MTTF and the failure rate. In particular, in the run 3, 8 samples were used (percentage standard deviation of β around 30%), while in the run 4, we combined 2

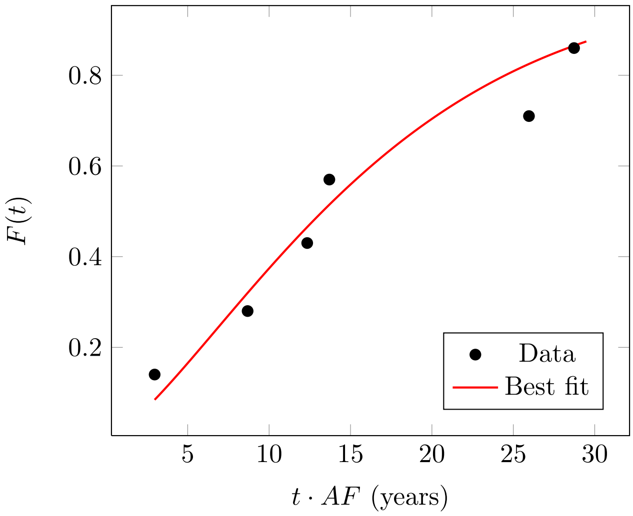

Figure 3.20: Weibull fit with the experimental data of the run 3. See table 3.4 for further details

independent experiments, each one with 8 samples, to get 16 failures (percentage standard deviation of β around 25%).

As regards the acceleration factor, we calculated the ratio between the total UniPA flux for energies higher than 2 MeV and the integral of the JESD89A reference spectrum, obtaining 1.89×10^6.

3.2.2 Results and discussion

The SEB threshold is around the 90% of the breakdown voltage, therefore it is higher than the value obtained with the ANITA source. This discrepancy is due to the neutrons with energies higher than 11 MeV: they can trigger more energetic secondary charged particles which in turn can induce a SEB at a lower test voltage.

Some curve fitting of experimental data are showed in figures 3.20 and 3.21.

Finally, we verified whether any radioactive decay products (such as α particles) could induce SEB. In fact, in the ANITA experiment, we observed some anomalous failures during the bias ramp up, especially in the preliminary runs. This type of emission is asynchronous or delayed with respect to the neutron source and in some way can lead to misjudgements. For this purpose we have irradiated the DUT without polarization for one hour, in order to bring them in a saturation condition (the production rate of radionuclides equalizes the radioactive decay rate). Afterwards, we extracted the DUT and polarized them for another hour, monitoring the drain voltages, but we didn't observe any SEB.

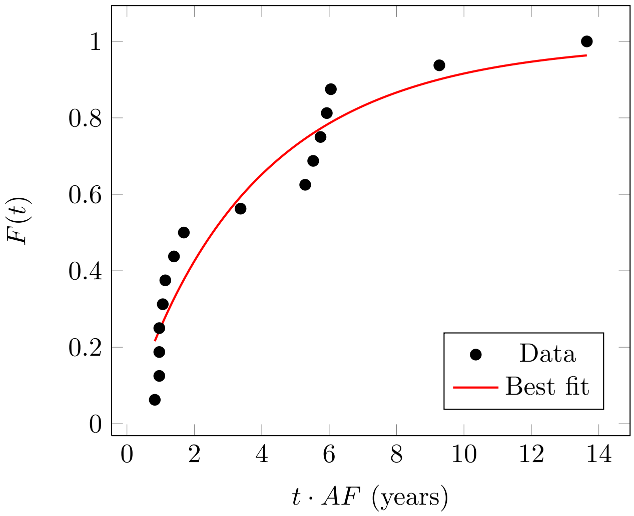

Figure 3.21: Weibull fit with the experimental data of the run 4. See table 3.4 for further details

Bibliography chapter 3

[1] H. Asai et al. "Terrestrial Neutron-Induced Single-Event Burnout in SiC Power Diodes". In: *Nuclear Science, IEEE Transactions on* 59.4 (Aug. 2012), pp. 880–885. ISSN: 0018-9499. DOI: `10.1109/TNS.2012.2203145`.

[2] E.W. Cascio et al. "Single Event Effects in Power MOSFETs Due to the Secondary Neutron Environment in a Proton Therapy Center". In: *Nuclear Science, IEEE Transactions on* 59.6 (Dec. 2012), pp. 3154–3159. ISSN: 0018-9499. DOI: `10.1109/TNS.2012.2221741`.

[3] G. Consentino et al. "Dangerous effects induced on power MOSFETs by terrestrial neutrons: A theoretical study and an empirical approach based on accelerated experimental analysis". In: *AEIT Annual Conference, 2013*. Oct. 2013, pp. 1–6. DOI: `10.1109/AEIT.2013.6666813`.

[4] G. Consentino et al. "Effects on power transistors of Terrestrial Cosmic Rays: Study, experimental results and analysis". In: *Applied Power Electronics Conference and Exposition (APEC), 2014 Twenty-Ninth Annual IEEE*. Mar. 2014, pp. 2582–2587. DOI: `10.1109/APEC.2014.6803667`.

[5] C.D. Davidson, E.W. Blackmore, and J.I Hess. "Failures of MOSFETs in terrestrial power electronics due to single event burnout". In: *Telecommunications Energy Conference, 2004. INTELEC 2004. 26th Annual International*. Sept. 2004, pp. 503–507. DOI: `10.1109/INTLEC.2004.1401516`.

[6] J. van Duivenbode and B. Smet. “An empiric approach to establishing MOSFET failure rate induced by Single-Event Burnout”. In: *Power Electronics and Motion Control Conference, 2008. EPE-PEMC 2008. 13th.* Sept. 2008, pp. 102–107. DOI: `10.1109/EPEPEMC.2008.4635251`.

[7] R. Edwards and J. Woodhouse. “Determination of High Energy Neutron Voltage Stress Margins for High Voltage IGBT and Diode Pairs from Two Manufacturers using Energetic Particle Induced Charge Spectroscopy, EPICS”. In: *Radiation Effects Data Workshop, 2006 IEEE.* July 2006, pp. 172–176. DOI: `10.1109/REDW.2006.295488`.

[8] A Griffoni et al. “Neutron-Induced Failure in Silicon IGBTs, Silicon Super-Junction and SiC MOSFETs”. In: *Nuclear Science, IEEE Transactions on* 59.4 (Aug. 2012), pp. 866–871. ISSN: 0018-9499. DOI: `10.1109/TNS.2011.2180924`.

[9] A Hands et al. “Single Event Effects in Power MOSFETs and SRAMs Due to 3 MeV, 14 MeV and Fission Neutrons”. In: *Nuclear Science, IEEE Transactions on* 58.3 (June 2011), pp. 952–959. ISSN: 0018-9499. DOI: `10.1109/TNS.2011.2106142`.

[10] A Hands et al. “Single Event Effects in Power MOSFETs Due to Atmospheric and Thermal Neutrons”. In: *Nuclear Science, IEEE Transactions on* 58.6 (Dec. 2011), pp. 2687–2694. ISSN: 0018-9499. DOI: `10.1109/TNS.2011.2168540`.

[11] *JESD89A: Measurement and reporting of alpha particle and terrestrial cosmic ray induced soft errors in semiconductor device.* Standard Rev. A. JEDEC Solid State Technology Association, 2006.

[12] S. Nishida et al. “Cosmic ray ruggedness of IGBTs for hybrid vehicles”. In: *Power Semiconductor Devices IC’s (ISPSD), 2010 22nd International Symposium on.* June 2010, pp. 129–132.

[13] E. Normand et al. “Neutron-induced single event burnout in high voltage electronics”. In: *Nuclear Science, IEEE Transactions on* 44.6 (Dec. 1997), pp. 2358–2366. ISSN: 0018-9499. DOI: `10.1109/23.659062`.

[14] D.L. Oberg et al. “First observations of power MOSFET burnout with high energy neutrons”. In: *Nuclear Science, IEEE Transactions on* 43.6 (Dec. 1996), pp. 2913–2920. ISSN: 0018-9499. DOI: `10.1109/23.556885`.

[15] AV. Prokofiev et al. “Characterization of the ANITA Neutron Source for Accelerated SEE Testing at The Svedberg Laboratory”. In: *Radiation Effects Data Workshop, 2009 IEEE.* July 2009, pp. 166–173. DOI: `10.1109/REDW.2009.5336295`.

[16] T. Shoji et al. “Neutron induced single-event burnout of IGBT”. In: *Power Electronics Conference (IPEC), 2010 International.* June 2010, pp. 142–148. DOI: `10.1109/IPEC.2010.5543845`.

[17] *STD MIL 750 E: Test methods for semiconductor devices.* method 1080. USA Department of Defence, 2011.

[18] A.D. Touboul et al. "Neutrons-Induced IGBT Failure: Effects of the Number of Tested Devices on the Cross Section Calculation". In: *Nuclear Science, IEEE Transactions on* 60.4 (Aug. 2013), pp. 2392–2396. ISSN: 0018-9499. DOI: `10.1109/TNS.2013.2248747`.

[19] A.D. Touboul et al. "On the reliability assessment of trench fieldstop IGBT under atmospheric neutron spectrum". In: *Microelectronics Reliability* 52.1 (2012). 2011 Reliability of Compound Semiconductors (ROCS) Workshop, pp. 124–129. ISSN: 0026-2714. DOI: `http://dx.doi.org/10.1016/j.microrel.2011.08.023`. URL: `http://www.sciencedirect.com/science/article/pii/S0026271411004185`.

Chapter 4

TCAD simulations

Contents

TCAD simulators represent a powerful tool for SEE investigation. Experimental tests can be quite expensive, requiring to access to particle accelerator facilities while TCAD simulations offer a way to perform virtual experiments that could be used to gain preliminary insights. Furthermore they provide not only device currents and voltages, but also relevant quantities, like carrier density, electric field, lattice temperature. In this chapter SEB simulations will be overviewed.

4.1 TCAD overview

Technology Computer Aided Design is a branch of electronic design automation that models semiconductor fabrication and semiconductor device operation. They are used to accelerate the development of new semiconductor technologies, thus differing from Electronic Computer Aided Design (ECAD), which are used to design new product with an existing technology.

The core tools of TCAD are process and device simulators. Process simulators incorporate physical models for phenomena such as diffusion, oxidation, ion implantation, deposition and etching and predict the structures that result from applying a sequence of these processes to an initial structure. On the other hand, device simulators solve equations that express charge continuity and the dependency of the electrostatic potential on the distribution of charge. In order to solve the charge continuity equations, device simulators need models for charge transport (such drift-diffusion and hydrodynamic models) and for generation and recombination of charge carriers.

Process and device simulators use numerical techniques to integrate coupled non-linear differential equations that describe the underlying physics of an experiment. In principle, they are able to predict the result of experiments, without requiring the experiments to be run. A predictive simulation is useful whenever it is time consuming, expensive, dangerous, or otherwise difficult to run real experiments. In the case of microelectronics development, it is both consuming and expensive to run real experiments in a semiconductor fab. As a result, it can be cost effective to substitute simulated experiments for some of the real experiments that would otherwise be required by purely empirical development procedure. Furthermore, simulations can predict non only all the quantities that are measured routinely, but also those one that are either very difficult or impossible to measure. Examples of such quantities are the doping profiles, carrier profiles and electrostatic potential distributions within a semiconductor device. By examining these quantities, engineers gain insight into the subtleties of device operation. This insight can guide the direction of future development and it can lead to the development of simple analytic theories that capture the essence of device operation.

Obviously, TCAD simulations have several limitations, especially regarding the result accuracy. Obtaining fully predictive simulations is still a challenging task, however, you cannot expect the same accuracy for physics-based simulators and data modelling. The agreement between modelled and experimental data is normally very good, but data models are used to interpolate and not to extrapolate. The agreement between simulated and experimental data is subjected to several sources of uncertainty that can lead to significant discrepancies between simulated data and experimental data. First of all, the underlying physics for some technology nodes is not fully well defined yet. For each physical phenomenon there is a hierarchy of models, with increasing complexity. All of these introduce approximations. In general, the more complicated models provide a more complete description, but are more difficult to implement and involve longer computation time. The need to select appropriate accuracy-efficiency trade-off can make it difficult for non experts to utilize TCAD effectively. Furthermore, numerical techniques provide an approximate solution that is defined on a discrete mesh of points. The choice of mesh and numerical techniques has a major impact on the accuracy and efficiency with which solutions are obtained. Using a finer mesh provides solutions that have higher accuracy but are calculated more slowly. Numerical techniques for solving non linear equations employ sequences of approximations that are expected to converge to a solution. In some cases the sequence of approximations fails to converge. Because of these issues, TCAD users need some expertise in defining meshes and numerical techniques that provide acceptable trade-offs between accuracy, efficiency and stability. In some cases it is possible to reduce these errors by adjusting the values of the model parameters used by the simulators.

Anyway, from the foregoing, TCAD tools are particularly suited for power device radiation hardness assessments because:

- experimental tests are quite expensive, requiring a large amount of samples for destructive technique characterizations and the access to particle accelerator facilities;
- device simulations provides not measurable quantities such as carrier and current densities, voltage profiles and so on that could help gaining insight and capture basic physical phenomena involved in SEB and SEGR;
- process simulation can be used to try new rad-hard techniques at process or layout levels.

In this work we used the Sentaurus TCAD suite by Synopsys. Following, a brief description of the used tools.

4.1.1 Sentaurus TCAD

Sentaurus is a comprehensive suite of TCAD tools for process and device simulations. Our main focus was on device simulation, therefore we will mainly describe the sdevice tool. It simulates 1D, 2D, and 3D device behaviour over a wide range of operating conditions, including mixed-mode circuit simulation, combining numerically simulated devices with their compact modelling, which is performed on a SPICE-based circuit simulation level. The typical device tool flow is as follows. The first step is the device structure creation. This can be accomplished either by process simulation (with the sprocess tool) or by a structure editor. In this case, 2D and 3D device models are created geometrically, using 2D or 3D primitives, such as rectangles, polygons, cuboids, cylinders, and spheres. The GUI of Sentaurus structure editor features a command-line window, in which Sentaurus structure editor prints script commands corresponding to the GUI operations. Beside the command file, other 2 input files are required: the boundary _bnd.tdr file, which includes the region and material specifications, plus the electrical and thermal contacts and the command _msh.cmd file, which include the doping profile definitions and the mesh strategy.

In order to build a sdevice-ready structure, we need to generate a mesh. At the end of this step, we obtain a log file (_msh.log) and a _msh.tdr file which can be used in the following device simulation. In addition, sdevice requires a command file (_des.cmd), having its own syntax and an optional parameter file (with .par extension) with the specification of the material parameters and user-defined model parameter. The main sections of the sdevice command are as follows. The *file* section define the input and output files for simulation. The input files have already been mentioned; the output files are the current file (_des.plt), which contains the voltages, currents and charges at the electrodes, and the field quantities defined in the optional CurrentPlot section and the plot file (_des.tdr) which contains all the field data, such as the current and carrier densities within the device structure. The electrical device contacts are declared in the *electrode* section together with the initial boundary conditions (bias) and other optional specifications. In the *physics* section you declare the physical models to be used in the simulation. The physical models can be defined globally, material-wise or region-wise. The *math* section is used to control the simulator numerics. The *solve* section consists of a series of simulation commands to be performed that are activated sequentially. The specified command sequence instructs the simulator as to which task must be solved and how. Typically, 2 solve statements are used in SEE simulations: the quasi-stationary command, used to ramp a device from one solution to another through the modification of its boundary conditions (such as contact voltages) or parameter values and the transient command, used to perform a transient time simulation.

Sentaurus also provides 2 different tool for graphical visualization of the simulation results: inspect and svisual. Finally, sdevice can be launched in stand-alone mode or inside the workbench tool, a primary graphical front-end that integrates TCAD sentaurus simulation tools into one environment. It is used throughout the semiconductor industry to design, organize and run simulations. Sentaurus workbench automatically manages the information flow, which includes pre-processing user input files, parametrizing projects, setting up and executing tool instances and visualizing results. It also allows you to define parameters and variables to run comprehensive parametric analyses.

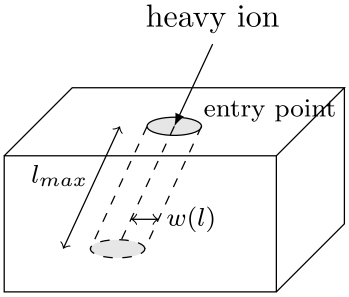

Figure 4.1: Heavy ion track modelling

4.2 Literature overview

4.2.1 Heavy ion track modelling

Historically, early research about SEE on power transistors date back the late 80s and were conducted in the aerospace industry to explain anomalous failures caused by heavy ions. Although the neutron ionization mechanisms are totally different, our discussion can not be separated from the simulation paradigm of the heavy ion induced SEE.

When a heavy ion penetrates a device structure, it loses energy and creates a trail of electron hole pairs. Important factors are:

- the energy and type of the ion;
- the angle of penetration of the ion
- the relation between the lost energy or LET and the number of pairs created.

Charge production around the path of an incident ion is accomplished by the release of energetic electrons (also referred to as delta rays) along the track, which subsequently travel away from the path and produce further electron hole pairs. The higher the energy of the incident particle, the higher the energy of the delta rays and the larger the radial extent of the induced charge distribution. As it passes through the silicon device, the particle loses energy and hence the delta rays also become less energetic, releasing charge nearer the center of the path as the particle nears the end of its range. Incident particles therefore generate a characteristic cone-shaped charge plasma in the silicon device. For a given ion strike, there is also the more fundamental issue of variation of charge density along the path (i.e., LET is not constant as a function of depth).

Ion track charge generation occurs as a result of adding a generation term in the continuity equations for electrons and holes. In particular, it is usually expressed as the product of 3 terms:

$$G_{ion}(x,y,z,t) = G_{LET}(x,y,z) \cdot R(x,y,z) \cdot T(t) \tag{4.1}$$

where G_{LET} takes into account the charge variations along the longitudinal direction (according to the ion LET); R takes into account the charge variations along the transverse direction and T is a temporal envelope. Sometimes, it is convenient to express G_{ion} as a function of other spatial coordinates, the ion longitudinal length l and the transverse length $w(l)$:

$$G_{ion}(l,w,t) = G_{LET}(l) \cdot R(l,w) \cdot T(t) \tag{4.2}$$

Regarding the G_{LET} term, a simple first-order analysis, the LET is multiplied by the mass density of the target material (Si) to obtain the energy deposited per unit track length (typical units of MeV µm^{-1}). It takes 3.6 eV to create one electron hole pair in silicon, so the energy deposited per unit track length is divided by 3.6 eV to obtain the number of electron hole pairs per track length (units of µm^{-1}). In order to obtain a quantity having units more applicable to device operation (e.g., cm^{-3}), the number of electron hole pairs per track length is divided by an assumed value of the initial cross-sectional area of the charge filament. This value corresponds to the characteristic radius w_t of the R term, modelled as a Gaussian function:

$$R(w,l) = \exp\left[-\left(\frac{w}{w_t(l)}\right)^2\right] \tag{4.3}$$

As a first-order approximation, w_t is constant and have a typical value of fractions of µm. The temporal envelope is also modelled as Gaussian-shaped function with peak (t_0) and characteristic length (t_c):

$$T(t) = \frac{1}{\sqrt{2\pi}t_c} \exp\left[-\frac{(t-t_0)^2}{2{t_c}^2}\right] \tag{4.4}$$

Finally, the ion track is described as straight line with a completely arbitrary spatial orientation, specified by an origin coordinate (x,y,z) and either an end coordinate (x,y,z) or a track length together with angles to the yz and xz planes.

4.2.2 Simulation domain and meshing issues

Power transistors are made up several elementary cells, all connected in parallel. In the standard electrical current-voltage simulations of a power device, only one elementary cell is considered in the simulation domain, because of the intrinsic symmetry. In fact, the contact current values can be multiplied by a proportional factor to take into account the remaining cell contributions. The same does not apply for SEE simulations, because SEB involve filamentary current, i.e. the current is not uniformly distributed: so the simulation domain has to embrace the neigh boring cells. It is important to include sufficient simulation volume around the region of a particle strike to avoid non-physical results at the boundaries. With the exception of contact regions, most boundaries in a device simulation are modelled using reflective boundary conditions. If the ion strike being simulated is located too close to such a reflective boundary, it results in charge being reflected at the boundary rather than continuing to diffuse away from the strike. Physically, this is equivalent to another ion strike being located the same distance away on the other side of the boundary.

Furthermore, the inherently 3D nature of an ion passing through a microelectronic device is difficult to address with the 2D simulation programs that are routinely used in the semiconductor industry for device analysis. In a 2D rectangular simulation, all quantities are assumed to be extruded into the third dimension, and hence either the correct generated charge density or the correct total charge can be simulated, not both. Another method is to use quasi 3D structures based on cylindrical symmetry and coordinate transformations. Unfortunately, there are few devices that exhibit circular symmetry, and full 3D device codes are necessary to model the effects of angled ion strikes. The implication of these results is that while 2D simulations may provide basic insight, 3D simulation is necessary if truly predictive results are to be obtained.

The correct allocation of the mesh grid is also very important for predictive modelling of SEE phenomena as it determines the integration accuracy of heavy ion generation rates. In fact, the integration of the generation rate over the control volume associated with each vertex in the mesh is performed under the assumption that the generation rate is constant inside the vertex control volume and equal to the generation rate value at the vertex. As heavy ion generation rates can change very rapidly in space, the approximation error with such an approach may lead to large errors on a coarse mesh (in particular, the method does not guarantee charge conservation). A compromise solution is to tighten the mesh in the region where high concentration gradient are expected.

Moreover, the movement of ion strike induced carriers under the influence of drift and diffusion presents another challenge to grid specification. Immediately after an ion strike, a high grid density in the strike region is required to resolve the ion induced carrier generation. After several nanoseconds, the ion induced carriers have diffused widely throughout the device, and a high grid density in the strike region is no longer desirable. The TCAD user thus seeks a grid algorithm capable of dynamically adapting as the single event transient progresses. Grid refinement based on heavy ion generation rate or excess carrier concentrations has been implemented in some device simulation tools but often leads to excess mesh generation due to the numerical difficulty of removing unnecessary grid points. This situation is exacerbated for 3D simulations. In some cases, it remains more efficient to design by hand a grid that accurately resolves all regions of interest.

4.2.3 Transient analysis

Once defined the heavy ion model, SEB simulations can be performed into 2 steps: a pre-strike quasi-stationary voltage sweep in order to set the bias voltages and a following transient domain analysis with the heavy ion generation activated. Basic physical models very often taken into account are:

- mobility models, with doping, lattice temperature and carrier-carrier related scattering, plus normal field dependence[1];
- carrier velocity overshoot (high field mobility saturation);
- Shockley–Read–Hall for generation–recombination processes description;
- Auger recombination and bandgap narrowing for heavily doped regions;
- impact ionization and Fermi statistic.

Moreover, several authors indicated that the temperature is a key parameter for modeling radiation-induced power devices failure. The lower computational burden compared to the drift-diffusion model is offered by the thermodynamic model, where thermal effects are incorporated into device by solving heat flow equation: carrier temperatures are equal to the lattice temperature, that is no longer a constant. In addition, thermal boundary conditions need to be specified either by a thermal contact, which may coincide with an existing electrical one or by a thermal insulating condition. In vertical power MOSFETs, the drain contact is common to all cells, therefore it may be reasonably considered as a thermal contact, having a fixed temperature value equal to the room temperature.

As well as in the experimental tests, a SEB event can be also detected in a transient simulation, monitoring the drain current versus time. Two different behaviours were observed: cases in which the drain-source current was self-sustaining (SEB) and cases in which the simulated current rises to a peak value and subsequently decays to zero (no SEB). Also the lattice temperature trend can reveal a SEB triggering. In fact, the parasitic BJT turn on brings the device into secondary breakdown regime, i.e. a thermal runaway condition. The heavy ion produce a filamentary current so that the

---

[1] unified mobility models (Philipps, Klaasen) can also be used

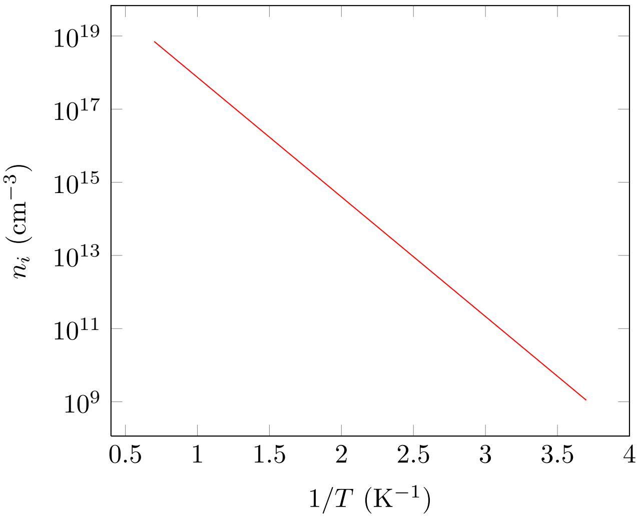

Figure 4.2: Silicon intrinsic density versus temperature reciprocal

device become locally heated due the Joule effect, in turn increasing the thermally generated carrier concentration, which leads to the a current increase flowing through the overheated regions and more heating yet. The overall process become unstable if the thermally generated carrier concentration exceeds the background doping concentration, i.e. the lattice temperature overcome a critical value T_c, that can be calculated from the background doping concentration N as:

$$n_i = 9.38 \times 10^9 \cdot (T_c/300) \cdot \exp(-6884/T_c) = N \tag{4.5}$$

From a simulation perspective, this critical temperature would be the criterion to define the destruction of the device to generate excess carriers.

Transient domain simulations were used to investigate the effect of the heavy ion impact location showing that the device sensitivity to SEB is highest if the ion is incident in the neck region close to the channel. Transient simulations were also used to test device structures with increased radiation tolerance. Effectiveness of decreasing emitter doping, increasing the base recombination, and increasing $p+$ plug size were verified. These modifications reduce the injection efficiency and overall gain of the parasitic BJT, thus reducing the SEB susceptibility.

Transient domains simulations were also used to capture the basic features of a SEB event triggering. However, they strongly depends upon the device's technology and the heavy ion's track: in fact, some authors have postulated the energy dependence on the SEB susceptibility. Moreover, almost all simulations studies with the transient domain approach are 2D, with all the consequences described in the previous section.

4.2.4 Avalanche curve

In 2006, Liu et al. proposed a new approach for SEB simulation, no longer based on the transient domain analysis. In the authors' opinion, the difficulties in achieving accurate or very meaningful SEE simulation results with the inclusion of an ion track are due to lack of a proper ion track definition and a valid or practical simulation models available (e.g. charge generation and transport). Therefore, their study focuses on the inherent limitations of a power MOSFETs in the off condition, over the breakdown regime. This can be accomplished performing quasi-stationary simulation in order to trace the device's avalanche curve, i.e. a i_{ds}/V_{ds} characteristic, with very high drain-source leakage current. Some common features were noticed: a negative differential resistance region appeared for very high drain current densities, delimited by 2 snap-back points: the first, with lower drain current, where the negative differential resistance region initiates, corresponds to the parasitic BJT activation and the second, where the negative differential resistance region finishes, corresponds to the second breakdown onset. Furthermore, this second point has a voltage value (V_{sb}) lower than the nominal breakdown and it is associated with the SEB threshold. Electric field cut-lines in these 2 snap-back points, revealed a gradual slope inversion, with the peak shifting from the body-epi to the epi-drain junction. This situation is in agreement with the theoretical model of the Current Induced Avalanche and seemed to indicate a great impact in the doping design of the epi-drain junction. The authors also suggested an additional epi-layer, with an intermediate doping concentration, as a radiation hardening technique.

It was also demonstrated the avalanche curves utility as a SEB prediction tool with some experiments. However there are some critical aspects:

- numerical issues about non convergence: the authors separated the source and body contacts and inserted 2 contact resistances whose values strongly affected the SEB threshold and the general convergence;
- self heating effects were ignored, notwithstanding the high drain-source currents;
- SEB depends upon a non uniformly distributed current, while in a quasi-stationary simulation the current is uniformly distributed over the entire simulation domain.

Also in these case, the avalanche curves are strictly tied to the power device's technology.

4.2.5 Neutron induced SEB simulations

What has been discussed so far concerns the simulation of heavy ion induced SEB. The extension of the transient domain approach to the neutron

Region	Doping	Concentration [cm^{-3}]
Source	$n+$	1×10^{20}
Body	$p+$	1×10^{19}
Drain	$n+$	1×10^{19}
N-pillar	n	1×10^{15}
P-pillar	p	3×10^{15}

Table 4.1: Dopant concentration list

case is not immediate. In fact, being a charged particle, the heavy ion directly ionizes through the Coulomb scattering; conversely, the neutron ionizes in a indirect manner, inducing the emission of secondary charged particles, as in a nuclear reaction, radioactive decay or spallation. Each of these processes can take place with a given probability. Furthermore, having 2 or more charged recoils, it should be included a ionizing track for each of them, starting from the interaction point, which can be not only in the silicon area, but also in the other material layers (e.g. metal, passivation). To properly describe each ionizing track, the neutron energy distribution among the several products needs to be calculated. Being a N-bodies problem, this kinematic calculation can be very complex.

On the other hand, the avalanche curves technique does not consider the ionization effects, so it cannot distinguish the heavy ion and the neutron related SEB thresholds.

Our approach was to performed transient domain TCAD simulations in order to evaluate the SEB threshold of a commercially available power MOSFET (the VJLL, see table 3.1). We took as reference the experimental results of the UniPA experiment. The nuclear interaction analysis was carried out, considering the facility spectrum. Because of the maximum neutron energy of this facility is around 11 MeV, we focused on nuclear reactions and the related radioactive decays, analysing the nuclear reaction cross-sections from the ENDF.

4.3 DUT details

The DUT has a stripe-line layout, i.e. the whole die area is covered by the repetition of several elementary stripes. A cross sectional view of a single strip is showed in figure 4.3. From the bottom to the top, there are the following layers: the backside metal, with a thickness of 0.5 µm, realized with a metal alloy of titanium, nickel and silver; the silicon substrate, with a thickness of 192 µm; the silicon active area, with a thickness of 81 µm, which also includes the gate oxide; the front metal, realized with a metal alloy of aluminium and silicon and the passivation layer, with a thickness of 2 µm,

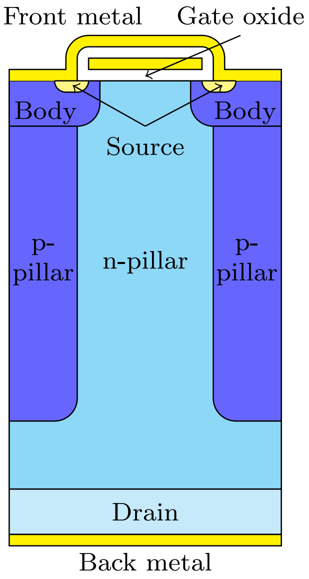

Figure 4.3: Cross-sectional view of a single elementary DUT strip

realized with silicon nitride and TetraEthyl OrthoSilicate (TEOS). Dopant species and their concentrations are listed in table 4.1.

The device structure was generated with the process simulation tool, in accordance with the actual design and the process details. Exploiting the intrinsic symmetry, we optimized the mesh point's allocation upon only one elementary 2D strip. However, for device simulations, we added other 6 elementary stripes, in order to prevent non physical effects due the reflective lateral boundaries. In particular, we extended the simulation domain in order to cover the average burnout diameter, observed during the post-failure microscope analysis on the failed DUTs. This modification was realized with sde, mirroring to the left and to the right the elementary 2D stripe.

We included only a small portion (about 5 microns) of the substrate layer into the simulation domain, because it is so heavily doped to be considered as a drain ohmic contact extension.

Regarding the mesh, we set the following constraints: maximum and minimum element sizes of 1 µm and 0.25 µm and grid refinement according the doping concentration gradient: the resulting grid has almost 42 000 points.

3D device structure was obtained by the extrusion of the correspondent 2D domain. However, we limited the extension along the x and z axis to 36 µm (2 equivalent elementary stripes) in order to obtain a reasonable trade-off between accuracy and elaboration times. Compared to the 2D case, we changed the mesh strategy, allocating the highest number of points in the neighbourhood of the z-coordinate of ionizing track start point the point of incidence of the ion

4.4 Nuclear analysis

The transient approach for SEB simulations requires to place the ionizing tracks within the active area, so the input parameters for the heavy ion model (such as the input and output points, the LCD and ranges) are to be known. However none of these parameters is known in principle, because we do not know which nuclear interactions caused the failures in the UniPA experiment. This situation differs significantly from heavy ion experiments. In fact, the DUTs are delidded and then irradiated from the front or back (possibly with a tilt angle): in simulation, the heavy ion track starts from the points immediately adjacent to the source/drain contacts or below the gate. Moreover, the ion energy in the impact point is known because the particle accelerators produces mono-energetic ions and the DUT exposures are carried out in vacuum conditions. In our case, the unique experimental evidence is that SEB are not caused by radioactive decays. Of course, the possible nuclear interactions which may result in charged recoils emissions with the UniPA spectrum and the DUT target materials are manifold. It would be impossible, even if unnecessary, to simulate all of them. A more practical approach is to select a limited set of significant interactions. In our case, we considered the nuclear reactions with 2 charged products for the following reasons:

- the distribution of the energy of the incident neutron over the charged products depends on only one additional parameter, that is the angle of emission;
- many cross-section data, related to this kind of nuclear reactions, are available in the ENDF database. In particular, we have the (n, α), (n, d), $(\mathrm{n}, {}^3\mathrm{He})$, (n, p) and (n, t) reactions cross-sections, not only for different materials, but also for their common isotopes.

In order to identify the most significant reactions to be simulated, we calculated the reaction rates for each of the reactions listed above, having as the target, the most common isotopes of the elements in the DUT. The reaction rate of a generic nuclear reaction x with a target is given by the following expression:

$$r_x(E) = \phi(E) \cdot \sigma_x(E) \cdot n \cdot V \tag{4.6}$$

where:

- $r_x(E)$ is the number of reactions of type x, per time unit (s^{-1});
- $\phi(E)$ is the neutron beam flux ($\mathrm{cm}^{-2}\,\mathrm{s}^{-1}$);
- $\sigma_x(E)$ is the microscopic cross section for reaction x;

Target	Isotope	Region	A [cm^2]	n [cm^{-3}]
Al	^{27}Al	Front metal	8.1×10^{-7}	6.0×10^{21}
As	^{75}As	Drain, active area	3.4×10^{-5}	1.0×10^{19}
B	^{11}As	Body, active area	4.5×10^{-7}	1.0×10^{19}
C	^{12}C	TEOS, passivation	1.8×10^{-7}	2.2×10^{22}
N	^{14}N	Nitride, passivation	1.8×10^{-7}	5.4×10^{22}
O	^{16}O	Gate oxide, active area	1.0×10^{-7}	5.3×10^{22}
O	^{16}O	TEOS, passivation	1.8×10^{-7}	1.1×10^{22}
P	^{31}P	Source, active area	3.6×10^{-9}	1.0×10^{20}
Si	^{28}Si	Active area	4.9×10^{-5}	5.0×10^{22}
Si	^{28}Si	Gate oxide, active area	1.0×10^{-7}	2.6×10^{22}
Si	^{28}Si	Nitride, passivation	1.8×10^{-7}	4.1×10^{22}
Si	^{28}Si	TEOS, passivation	1.8×10^{-7}	2.7×10^{22}
Ti	^{48}Ti	Back metal	9.0×10^{-8}	5.6×10^{21}

Table 4.2: Calculated values for reaction rate computations

- n is the atomic density of the target (cm^{-3});
- V is the target volume (cm^3).

If the target is a pure material, its atomic density n can be calculated using the Avogadro's number N_{av} and the molar weight M:

$$n = \frac{\rho \cdot N_{av}}{M} \tag{4.7}$$

For a chemical compound with p atoms of X and q atoms of Y, the atomic density of its constituents is calculated multiplying the atomic density of the compound (calculated with the equation 4.7), by the relative number of atoms p and q.

As for the volume, the intrinsic symmetry of the DUT can be exploited. Being formed by the repetition of many elementary stripes, the volume of a generic target is given by multiplying the surface occupied on a single cell, its depth and the number of cells. The product of these two last terms is equal to 1.38×10^6 cm.

The data used for the reaction rate calculations are listed into table 4.2.

4.4.1 Nuclear reaction rates

The most likely reaction occurs in the passivation layer and consists in the thermal neutron capture by nitrogen, which determines the emission of a proton. The reaction rates peak is $23\,008\,\mathrm{s}^{-1}$ at the energy of 1×10^{-5} eV. Furthermore, this reaction has a positive Q-value, so it occurs spontaneously with a substantial net release of energy, despite the very low energy of the

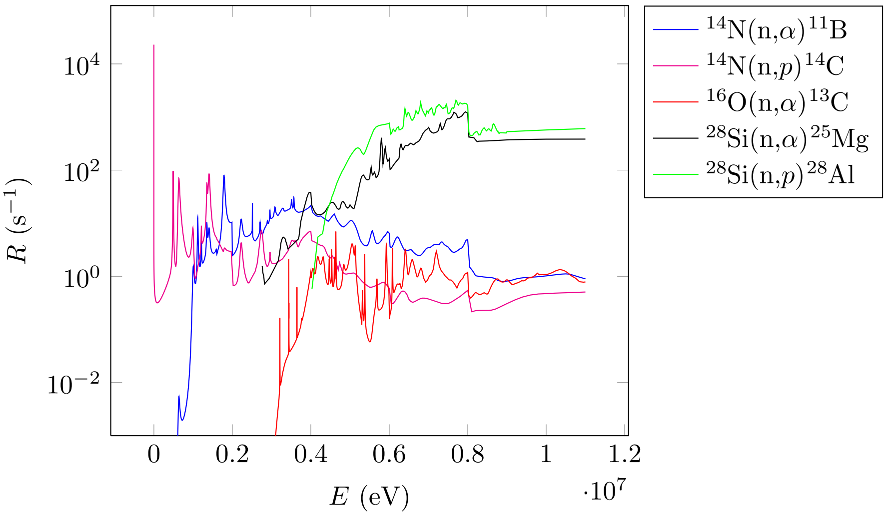

Figure 4.4: Most significant reaction rate curves versus energy

incident neutron. The same reaction may have place at higher energies, but with lower rates ($95\,\mathrm{s}^{-1}$ at 0.49 MeV and $58\,\mathrm{s}^{-1}$ at 1.35 MeV). The emitted proton may trigger SEB, if it crosses the metal layer and reaches the high electric field areas of the active region. All other reactions are characterized by peak values of reaction rates lower than 2-3 orders of magnitude. In the active area and in the substrate, the most likely reactions are related to the silicon, respectively, with a proton ($2063\,\mathrm{s}^{-1}$ at 7.7 MeV) and an alpha particle ($1176\,\mathrm{s}^{-1}$ at 7.9 MeV) emission. These reactions are probably the most dangerous, because the ionizing secondary particles are emitted directly into the most sensitive area of the device. Then we have another reaction with the nitrogen in the passivation layer, with an alpha particle as a product ($72\,\mathrm{s}^{-1}$ at 1.8 MeV). A detailed report is in table 4.3, while a graphical comparison is in figure 4.4. It should be noted that the products of the reactions listed above are all either stable or unstable with a half-life time far beyond the duration of the experiments, or unstable with beta emissions, which do not trigger SEB.

4.4.2 Recoils kinematics

The scheme of a generic 2 products nuclear reaction is represented in figure 4.5. The projectile n (in our case the neutron), hits, along the y-axis of our reference system, the target T; the light particle l and the heavy particle h are emitted with the angles θ and ξ, with respect to the neutron direction. The target is assumed in rest and therefore has no momentum. Applying the energy balance in the non-relativistic approximation, we obtain

Reaction	Layer	E [eV]	r [s^{-1}]	Q-value [eV]	Decay	Half life	Decay product
^{14}N(n, α)^{11}B	Passivation	1.8×10^{6}	72	-1.6×10^{5}	-	Stable	-
^{14}N(n, p)^{14}C	Passivation	1.0×10^{-5}	23 008	6.3×10^{5}	β^{-}	5.7×10^{5} years	^{14}N (stable)
^{14}N(n, p)^{14}C	Passivation	4.9×10^{5}	95	6.3×10^{5}	β^{-}	5.7×10^{5} years	^{14}N (stable)
^{14}N(n, p)^{14}C	Passivation	1.3×10^{6}	58	6.3×10^{5}	β^{-}	5.7×10^{5} years	^{14}N (stable)
^{28}Si(n, α)^{25}Mg	Active area	7.9×10^{6}	1176	-2.6×10^{6}	-	Stable	-
^{14}N(n, p)^{14}C	Active area	7.7×10^{6}	2063	-3.9×10^{6}	β^{-}	2.2 minutes	^{28}N (stable)

Table 4.3: Selected nuclear reactions and related peak reaction rates, energies, Q-values and decay models

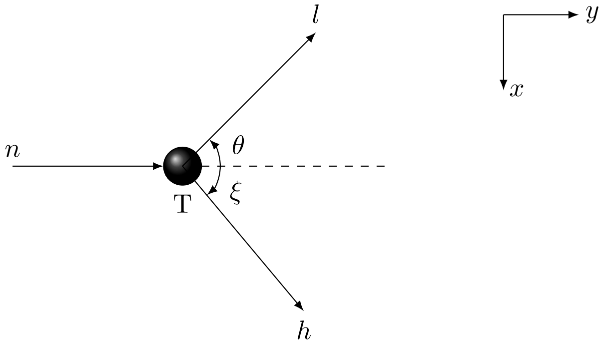

Figure 4.5: Pictorial view of a 2 products nuclear reaction

the kinetic energy of the particle l:

$$\begin{aligned} T_l^{1/2} = & \frac{(m_n m_l T_n)^{1/2} \cos\theta}{m_h + m_l} \\ & \pm \frac{\left\{ m_n m_l T_n \cos^2\theta + (m_h + m_l)\left[m_h Q + (m_h - m_n) T_n\right]\right\}}{m_h + m_l} \end{aligned} \tag{4.8}$$

where m_n, m_l, and m_h are the masses, T_n is the neutron energy and Q is the Q value of the selected reaction (see table 4.3). Once obtained T_l, we calculated the heavy particle energy as:

$$T_h = Q - T_l + T_n \tag{4.9}$$

Finally, we obtain the emission angle of the heavy particle ξ:

$$\sin\xi = \left(\frac{p_l}{p_h}\right) \sin\theta \tag{4.10}$$

where p_l and p_h are the light and heavy particle momenti.

As mentioned in section 4.4, there is a free parameter, i.e. the angle θ. To reduce the number of parameters in the TCAD simulations (we already have the test voltage, the nuclear reaction and the interaction point), we fixed the value of θ to 5°. This would represent the worst case, because, with small angles, there is a lower charge dispersion in the simulation domain. Recoil products energies are listed in table 4.4.

4.4.3 Recoils' Bragg curves

In order to describe the charge tracks induced by the reaction products into TCAD framework, we have to characterize their Bragg curves in the silicon. We computed these quantities with the SRIM/TRIM code (see figures 4.6 and 4.7). LCD peaks and ranges are listed in table 4.5. In the

Reaction	T_n [MeV]	T_l [MeV]	T_h [MeV]	θ [°]	ξ [°]
$^{14}\mathrm{N}(\mathrm{n},\alpha)^{11}\mathrm{B}$	1.8	1.5	1.2×10^{-1}	5	11
$^{14}\mathrm{N}(\mathrm{n},\mathrm{p})^{14}\mathrm{C}$	1.0×10^{-11}	6.0×10^{-1}	4.2×10^{-2}	5	5
$^{14}\mathrm{N}(\mathrm{n},\mathrm{p})^{14}\mathrm{C}$	5.0×10^{-1}	1.1	9.3×10^{-3}	5	15
$^{14}\mathrm{N}(\mathrm{n},\mathrm{p})^{14}\mathrm{C}$	1.3	2.0	5.1×10^{-3}	5	27
$^{28}\mathrm{Si}(\mathrm{n},\alpha)^{25}\mathrm{Mg}$	7.9	5.2	1.2×10^{-1}	5	13
$^{28}\mathrm{Si}(\mathrm{n},\mathrm{p})^{28}\mathrm{Al}$	7.7	3.8	2.6×10^{-2}	5	12

Table 4.4: Secondary products energies

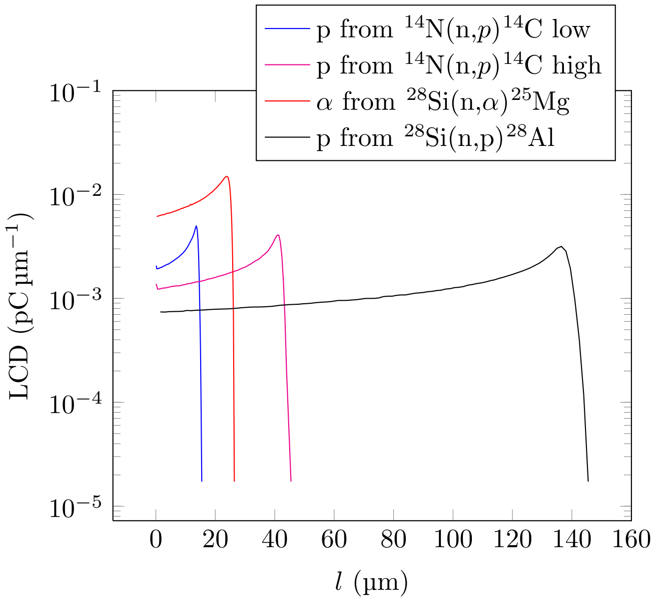

Figure 4.6: Bragg curves of long range recoils into the active area

active area, ionizing tracks can start from everywhere into the domain while for the reactions occurring in the other layers, the ionizing tracks start from the metal/silicon boundary. In the active area, the heavy reaction products (^{25}Mg and ^{28}Al) lose all their energy into fractions of microns. Regarding the passivation layer, only the proton has a significant range into the active area, while all the other products are stopped by the upper layers or, in the case of the alpha particle, stopped in fractions of microns.

4.5 2D simulations

We chose the thermodynamic model (drift-diffusion plus self-heating effect) as the basic equation set and, in addition, we selected the following

Reaction	Light recoil	Heavy recoil	LCD$_l$ [pC µm^{-1}]	LCD$_h$ [pC µm^{-1}]	r_l [µm]	r_h [µm]
^{14}N(n, α)^{11}B	α	^{11}B	8.2×10^{-3}	-	0.8	-
^{14}N(n, p)^{14}C[a]	p	^{14}C	5.4×10^{-3}	-	3.0	-
^{14}N(n, p)^{14}C[b]	p	^{14}C	4.9×10^{-3}	-	15.4	-
^{14}N(n, p)^{14}C[c]	p	^{14}C	4.1×10^{-3}	-	45.5	-
^{28}Si(n, α)^{25}Mg	α	^{25}Mg	1.5×10^{-2}	1.4×10^{-2}	26.7	0.4
^{28}Si(n, p)^{28}Al	p	^{28}Al	3.2×10^{-3}	1.0×10^{-2}	145.5	0.1

Table 4.5: Recoil LCD and ranges. All values are related to the silicon in the active area.

---

[a] Reaction with a neutron energy of 1.0×10^{-11} MeV

[b] Reaction with a neutron energy of 5.0×10^{-1} MeV

[c] Reaction with a neutron energy of 1.3 MeV

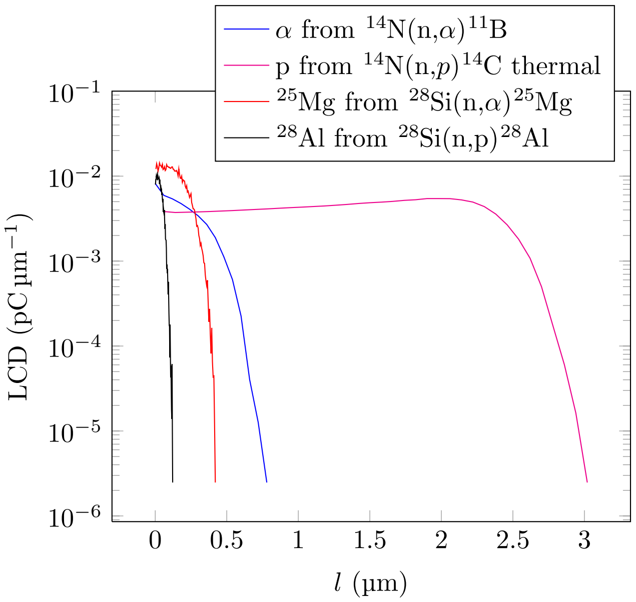

Figure 4.7: Bragg curves of short range recoils into the active area

physical models: Philips unified model, with high field saturation and Enormal as driving force for the mobility; Auger and Shockley-Reed-Hall with doping and electric field dependent minority lifetimes; Van Overstraeten model for impact ionization; Fermi statistics; Slotboom model for bandgap narrowing.

As for the thermal boundary condition, we attached a thermal surface resistance of $1.3 \times 10^{-2}\,\mathrm{K\,W^{-1}\,cm^{-2}}$ to the drain, in order to model the remaining substrate layer, and fixed the ambient temperature to 300 K.

4.5.1 Calibration

Some parameters of the physical models need to be tuned, changing their default values. For SEB simulations, the most crucial physical models are the impact ionization rate and the minority carrier lifetimes. In fact, SEB phenomena are characterized by a localized electro-thermal instability. SEB are initiated by filamentary currents, which evolves arises from electron-hole pairs generated by ionization: impact ionization multiplies the initial charge, so it enhances the current filament, while diffusion (due to high carrier density gradient into the depletion region) distributes the carrier concentration over a larger volume, and then perform a stabilizing action. How effective it is, depends on the minority carrier lifetimes.

Van Overstraeten model for the impact ionization rate is based on the

Parameter	Default value	Tuned value
τ_{max} (electron)	1.00×10^{-5} s	8.50×10^{-5} s
τ_{max} (hole)	3.00×10^{-6} s	2.55×10^{-5} s
b (electron)	1.23×10^{6} V cm^{-1}	1.17×10^{6} V cm^{-1}
b (hole)	2.04×10^{6} V cm^{-1}	1.93×10^{6} V cm^{-1}

Table 4.6: Calibrated values of physical model parameters

Chynoweth law:

$$\alpha(F_{ava}) = \gamma a \exp\left(-\frac{b}{F_{ava}}\right) \tag{4.11}$$

where α is the reciprocal of the mean free path for electrons and holes, F_{ava} is the electric field, a, and b are empirical parameters. The doping dependence of the minority lifetimes is modelled with the Scharfetter relation:

$$\tau_{dop}(N_i) = \tau_{min} + \frac{\tau_{max} - \tau_{min}}{1 + \left(\frac{N_i}{N_{ref}}\right)^{\gamma}} \tag{4.12}$$

where t_{min} and τ_{max} are the minimum and maximum minority lifetimes, N_{ref} is a reference doping level equal to $1 \times 10^{16}\,\mathrm{cm}^{-3}$, N_i is the actual doping level and γ is an empirical factor with a default value equal to 1.

A quick calibration was made comparing the simulated reverse I/V curve and the experimental data, averaged over 26 samples (breakdown voltage can have large variations between different samples of the same device). In fact, the minority carrier lifetimes affect the leakage current of the reverse biased body-drain junction, while the impact ionization rates affect the breakdown voltage, defined as the potential to be applied to drain (with gate and source shorted) for a leakage current of 1 mA. For this simulation we used an area factor of 1.38×10^{6} cm. Tuned values are finally reported in table 4.6, while the calibrated I/V curve is in figure 4.8. The resulting breakdown voltage is 1000 V, i.e. a 5% greater than the nominal value. This is a realistic situation, because the effective breakdown voltage a power MOSFET is usually greater than the reported value on its datasheet.

4.5.2 SEB simulations and results

We arranged SEB simulation into 2 steps: a quasi-stationary simulation to set the test voltage and a subsequent transient analysis, in which we enable the generation rate models for the ionizing reaction products. The simulation parameters are: test voltage, set as in the experiment, at 85%, 95% and 100% of BV_{dss}, the nuclear reaction as in table 4.4 and the interaction point inside the active area. Moreover, we considered an interaction

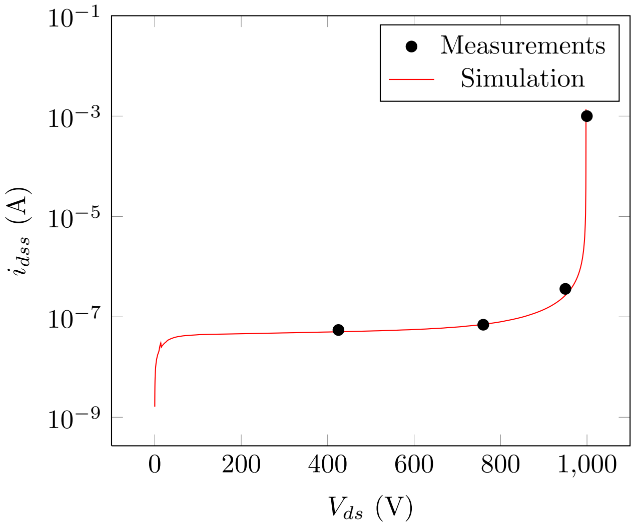

Figure 4.8: Calibrated reverse I/V curve

point grid with 3 significant abscissa values, corresponding to the neck region ($x = 9\,\mu\text{m}$), channel ($x = 12\,\mu\text{m}$) and body ($x = 18\,\mu\text{m}$) and 4 different depths in the epitaxial region ($y = -82.5\,\mu\text{m}$, $y = -62.5\,\mu\text{m}$, $y = -42.5\,\mu\text{m}$, $y = -22.5\,\mu\text{m}$). Not all reaction/interaction point combinations were simulated: in fact, for the passivation layer reactions, recoils tracks start from the silicon/metal boundary ($y = -82.5\,\mu\text{m}$).

A typical SEB event has the following features (see figures 4.10, 4.12, 4.13): the drain leakage current diverges, as well as the lattice temperature, exceeding the conventional thermal break criteria of 1000 K. Actually the thermal runaway already occurs at about 600 K: in this condition, silicon intrinsic carrier density, due to thermal generation effect, becomes as high as the n-pillar doping concentration, i.e. $1 \times 10^{15}\,\text{cm}^{-3}$ (see figures 4.20, 4.22).

As in the experiment, we found a SEB threshold voltage of 902.5 V, i.e. the 95% of the nominal breakdown voltage. SEB events are caused by the $^{28}\text{Si}(\text{n}, \alpha)^{25}\text{Mg}$ reaction in the active area; the other reactions involving a proton as the light recoil, both in the active area, both in the passivation layer, did not induce failures. Moreover, only few interaction points are really effective, even for drain voltages higher than the SEB threshold: the most sensitive regions are the neck and the channel, in the first $30\,\mu\text{m}$ from the silicon/metal boundary.

Observing the structure files (figures 4.15-4.18), it can be observed that the pillar restrict the lateral diffusion of the charge carriers in excess. On the contrary, near the drain, i.e. a common region to all strips, the current density spread is much higher. This could explain why the points B, C, E, F, H and I are less sensitive to SEB.

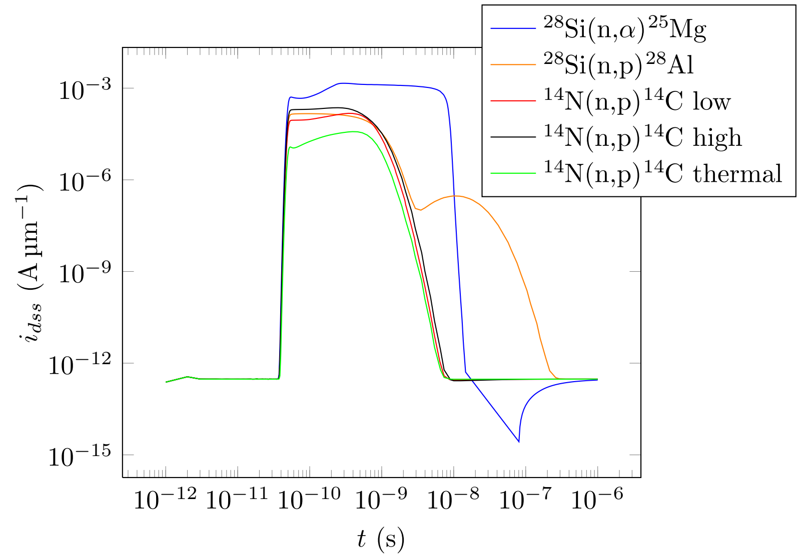

(a)

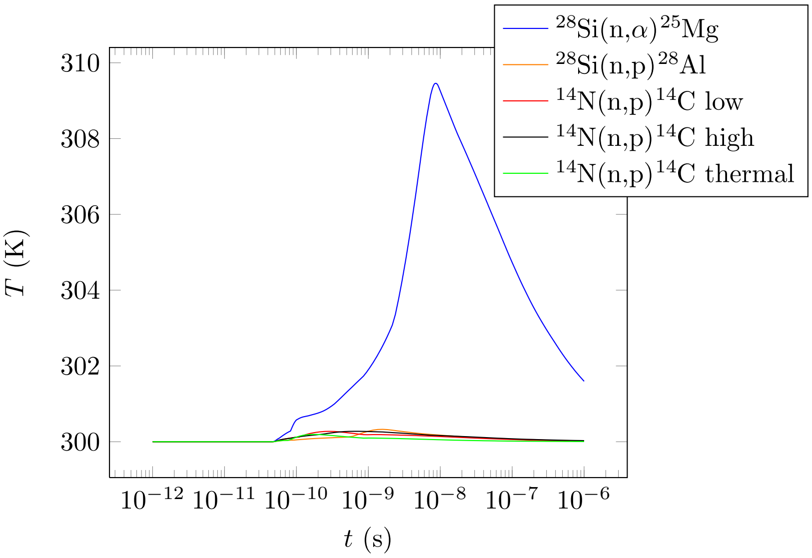

(b)

Figure 4.9: Simulation results with the 85% of BV_{dss} as test voltage, for different reactions in the interaction point A. The drain currents are in figure 4.9(a), while lattice temperatures are in figure 4.9(b)

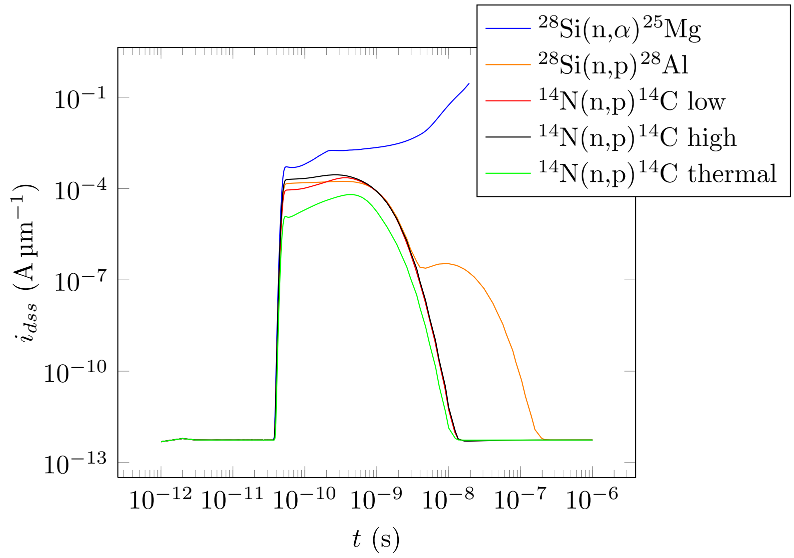

(a)

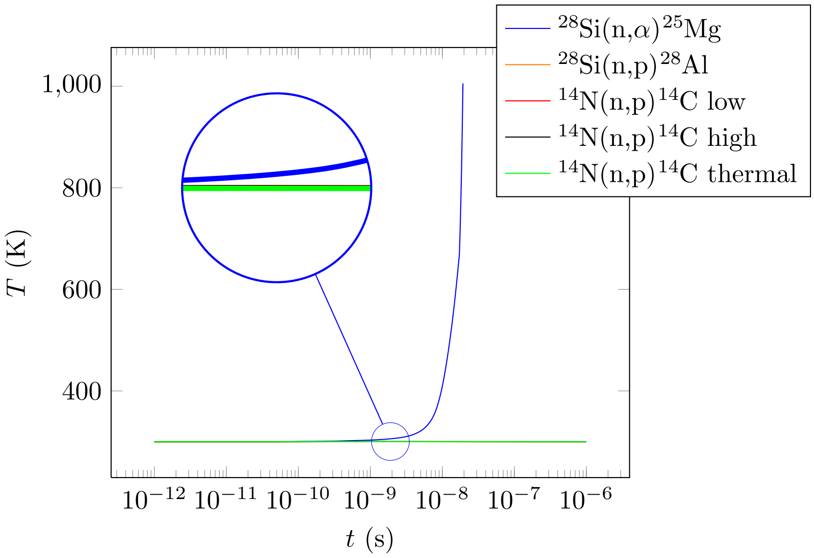

(b)

Figure 4.10: Simulation results with the 95% of BV_{dss} as test voltage, for different reactions in the interaction point A. The drain currents are in figure 4.10(a), while lattice temperatures are in figure 4.10(b)

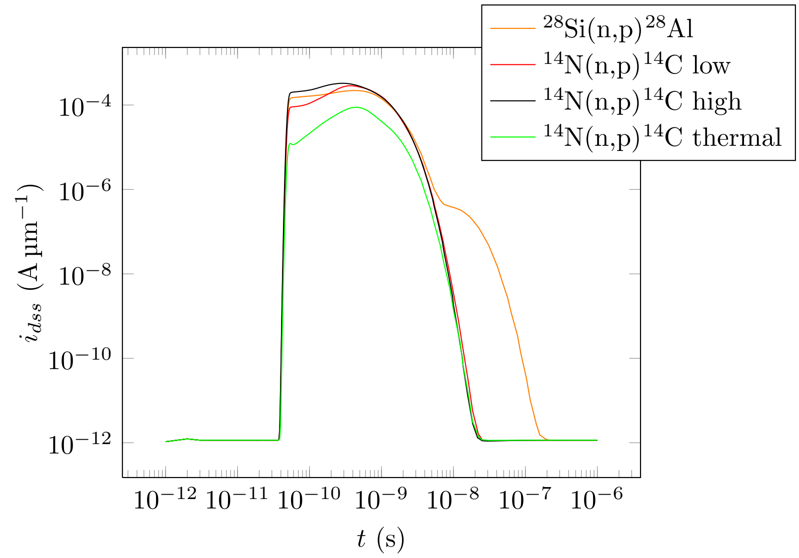

(a)

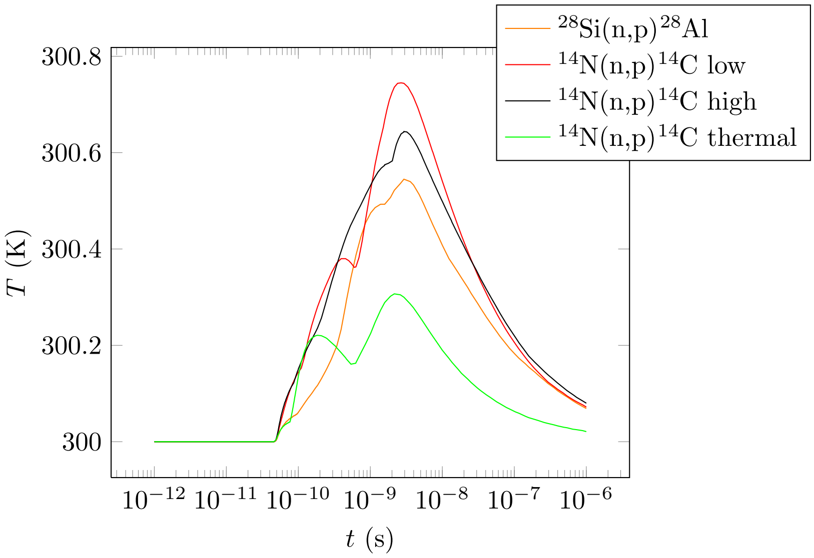

(b)

Figure 4.11: Simulation results with the 100% of BV_{dss} as test voltage, for different reactions in the interaction point A. The drain currents are in figure 4.11(a), while lattice temperatures are in figure 4.11(b)

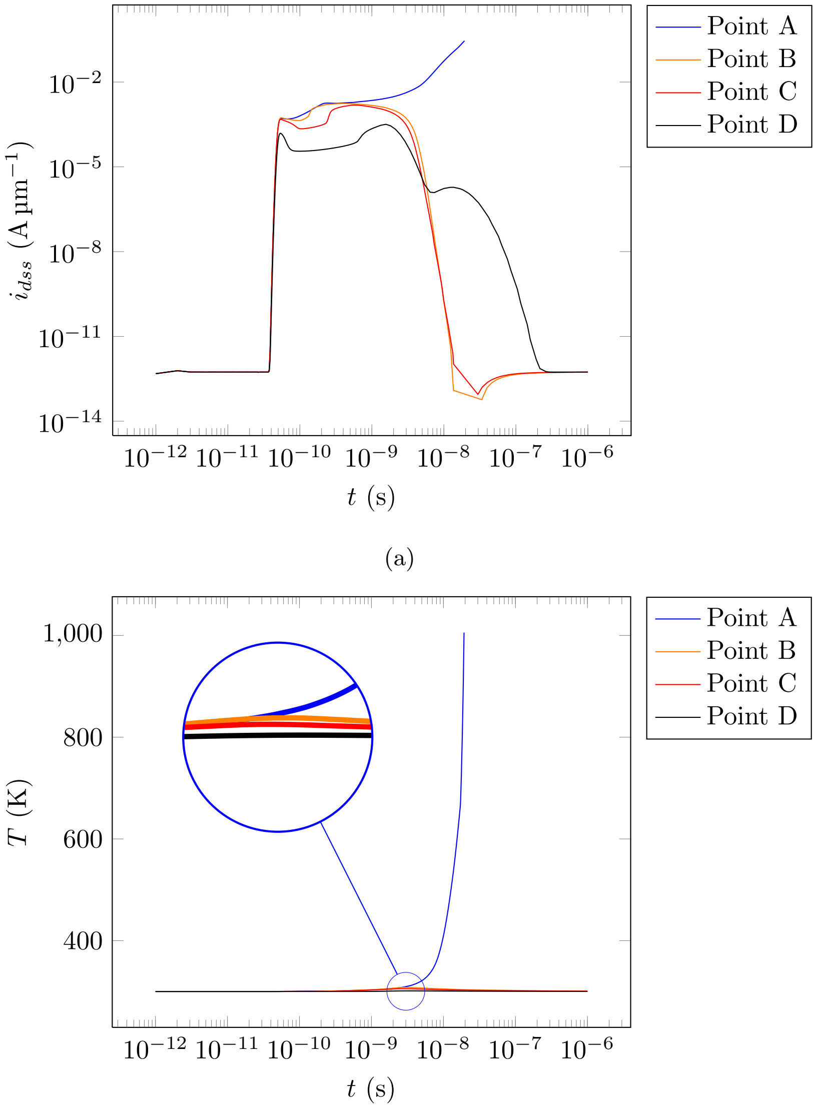

(a)

(b)

Figure 4.12: Simulation results with the $^{28}\mathrm{Si}(\mathrm{n}, \alpha)^{25}\mathrm{Mg}$ reaction, the 95% of BV_{dss} as test voltage and neck region (at different depths) as interaction point. The drain currents are in figure 4.12(a), while lattice temperatures are in figure 4.12(b)

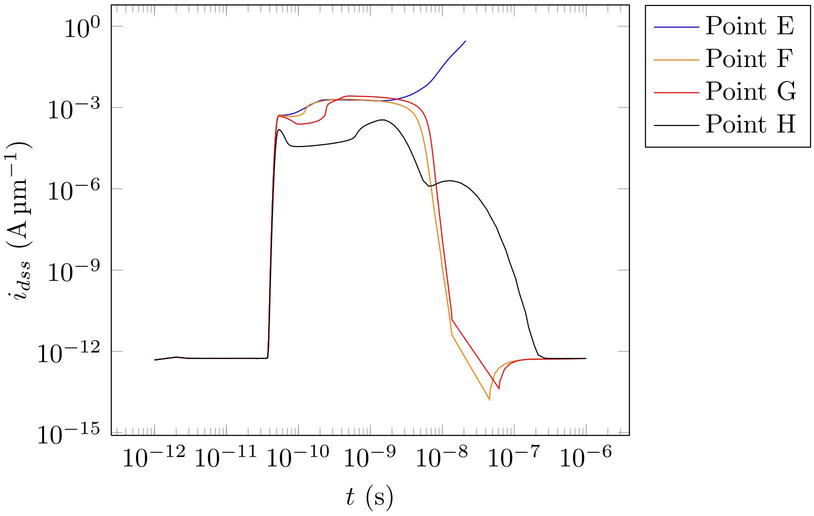

(a)

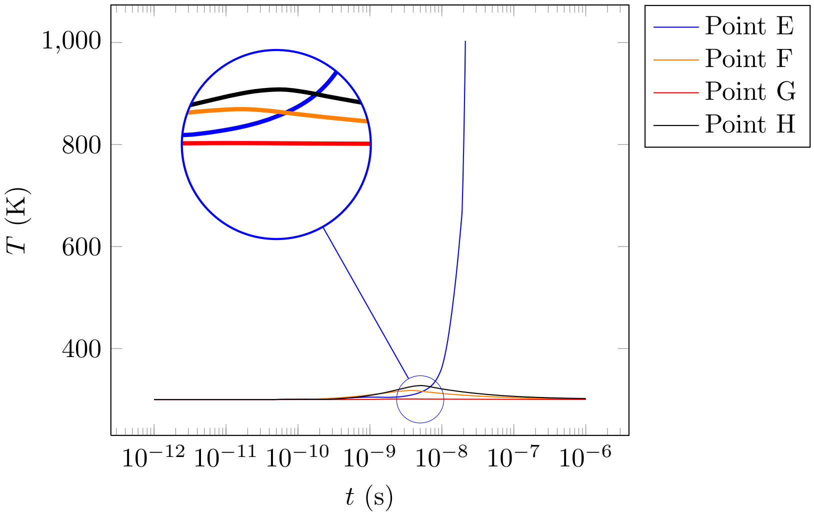

(b)

Figure 4.13: Simulation results with the ^{28}Si(n, α)^{25}Mg reaction, the 95% of BV_{dss} as test voltage and channel region (at different depths) as interaction point. The drain currents are in figure 4.13(a), while lattice temperatures are in figure 4.13(b)

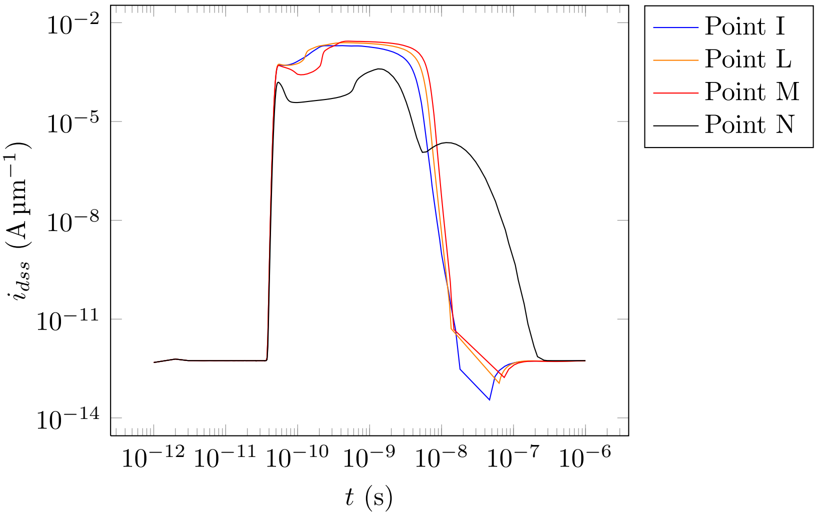

(a)

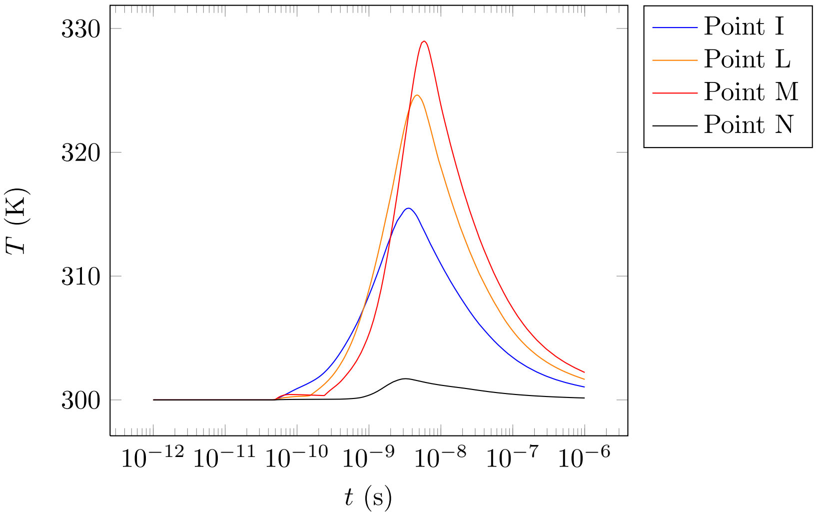

(b)

Figure 4.14: Simulation results with the $^{28}\mathrm{Si}(\mathrm{n},\alpha)^{25}\mathrm{Mg}$ reaction, the 95% of BV_{dss} as test voltage and body region (at different depths) as interaction point. The drain currents are in figure 4.14(a), while lattice temperatures are in figure 4.14(b)

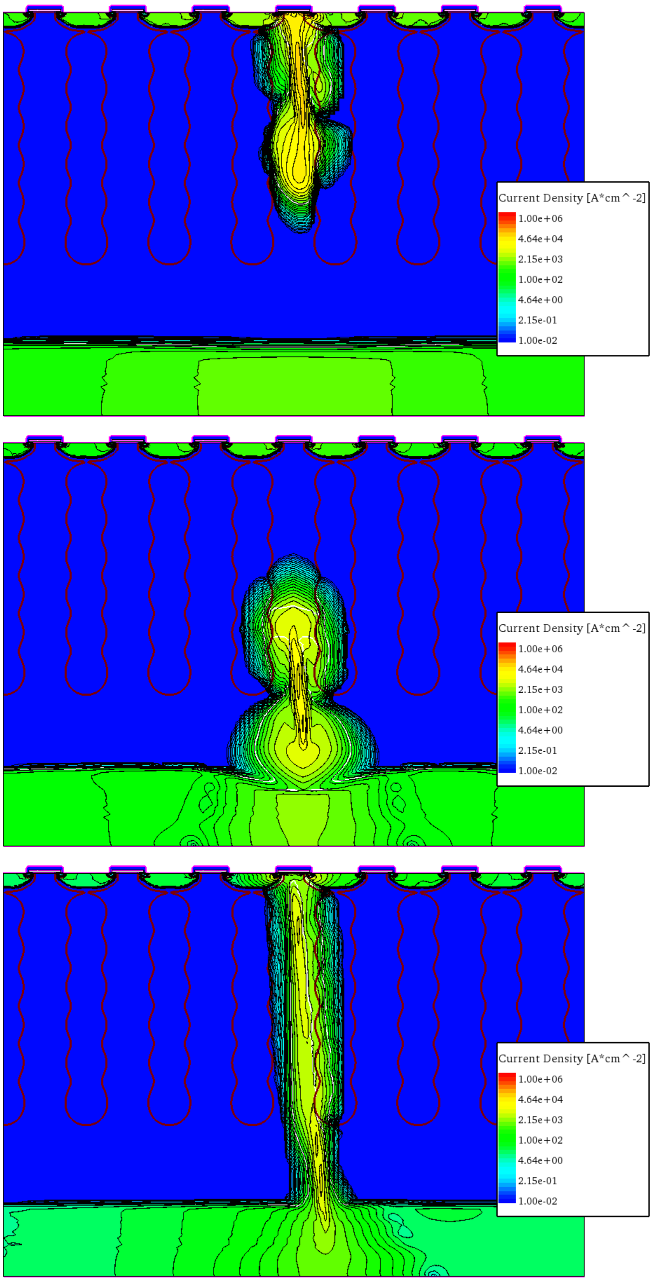

Figure 4.15: Current density distribution in the following conditions: $V_{ds} = 95\% BV_{dss}$, $t = 1.0 \times 10^{-10}\,\mathrm{s}$, $^{28}\mathrm{Si}(\mathrm{n}, \alpha)^{25}\mathrm{Mg}$ reaction in points A (upper figure) and C (intermediate figure) and $^{28}\mathrm{Si}(\mathrm{n}, \mathrm{p})^{28}\mathrm{Al}$ reaction in point A (lower figure)

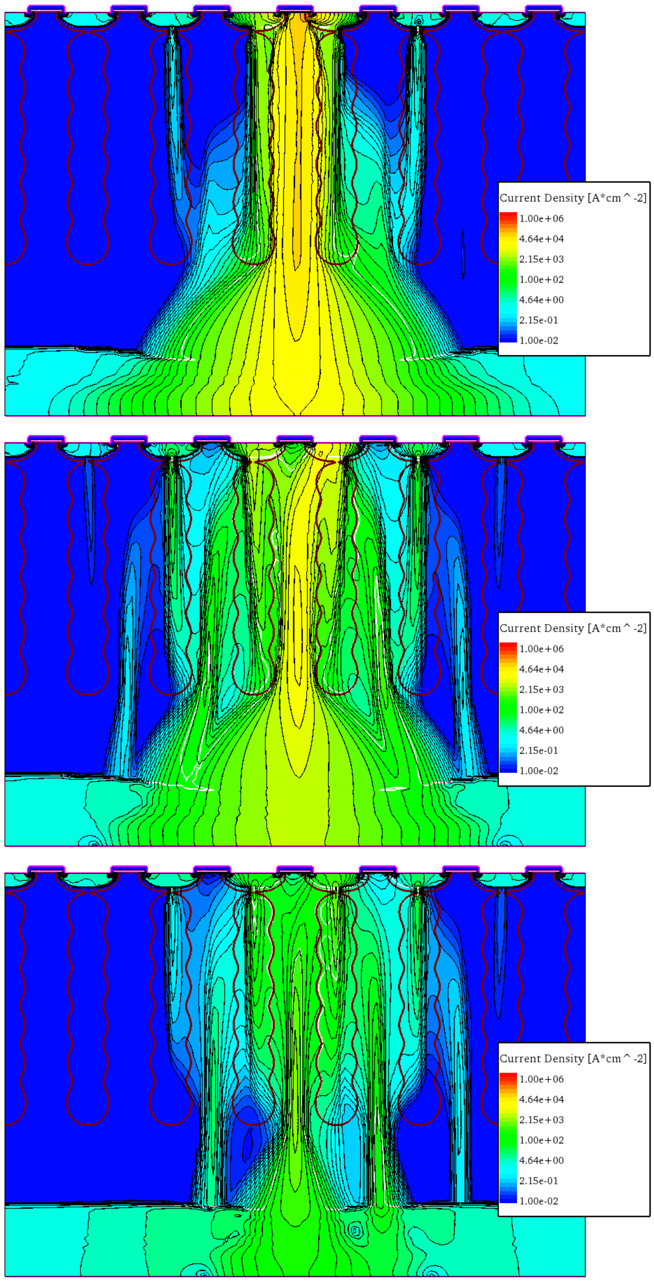

Figure 4.16: Current density distribution in the following conditions: $V_{ds} = 95\% BV_{dss}$, $t = 3.5 \times 10^{-9}$ s, $^{28}\mathrm{Si}(\mathrm{n}, \alpha)^{25}\mathrm{Mg}$ reaction in points A (upper figure) and C (intermediate figure) and $^{28}\mathrm{Si}(\mathrm{n}, \mathrm{p})^{28}\mathrm{Al}$ reaction in point A (lower figure)

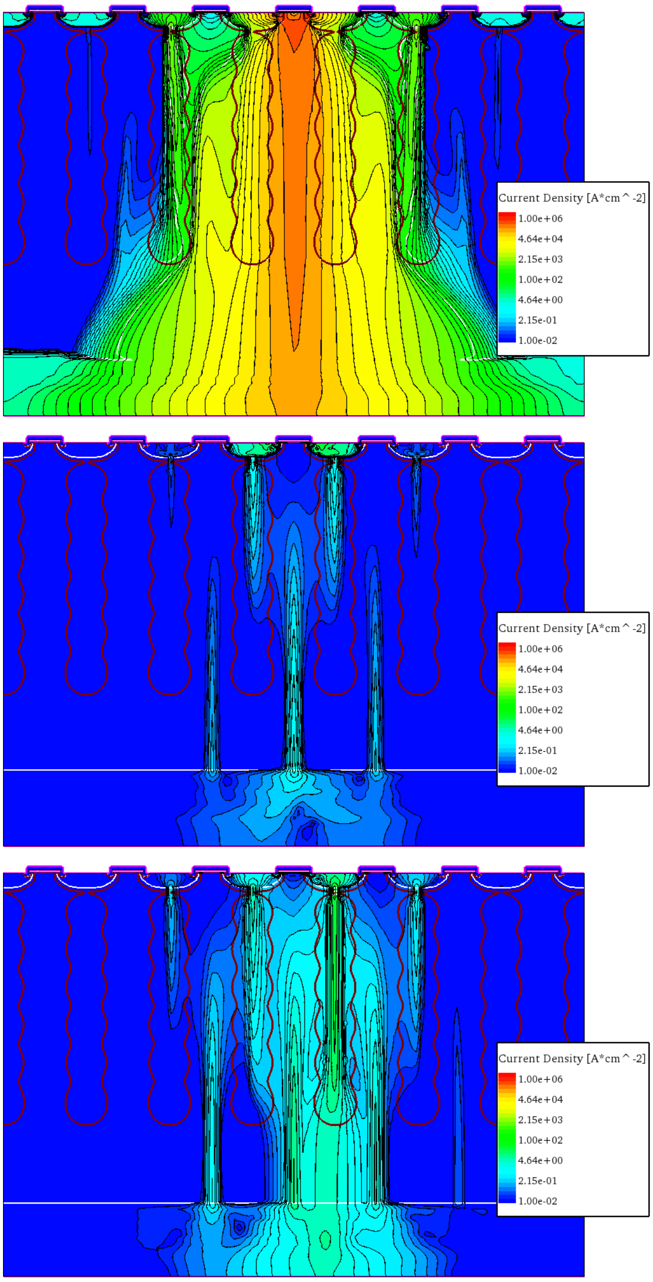

Figure 4.17: Current density distribution in the following conditions: $V_{ds} = 95\% BV_{dss}$, $t = 8.5 \times 10^{-9}$ s, $^{28}\mathrm{Si}(\mathrm{n},\alpha)^{25}\mathrm{Mg}$ reaction in points A (upper figure) and C (intermediate figure) and $^{28}\mathrm{Si}(\mathrm{n},\mathrm{p})^{28}\mathrm{Al}$ reaction in point A (lower figure)

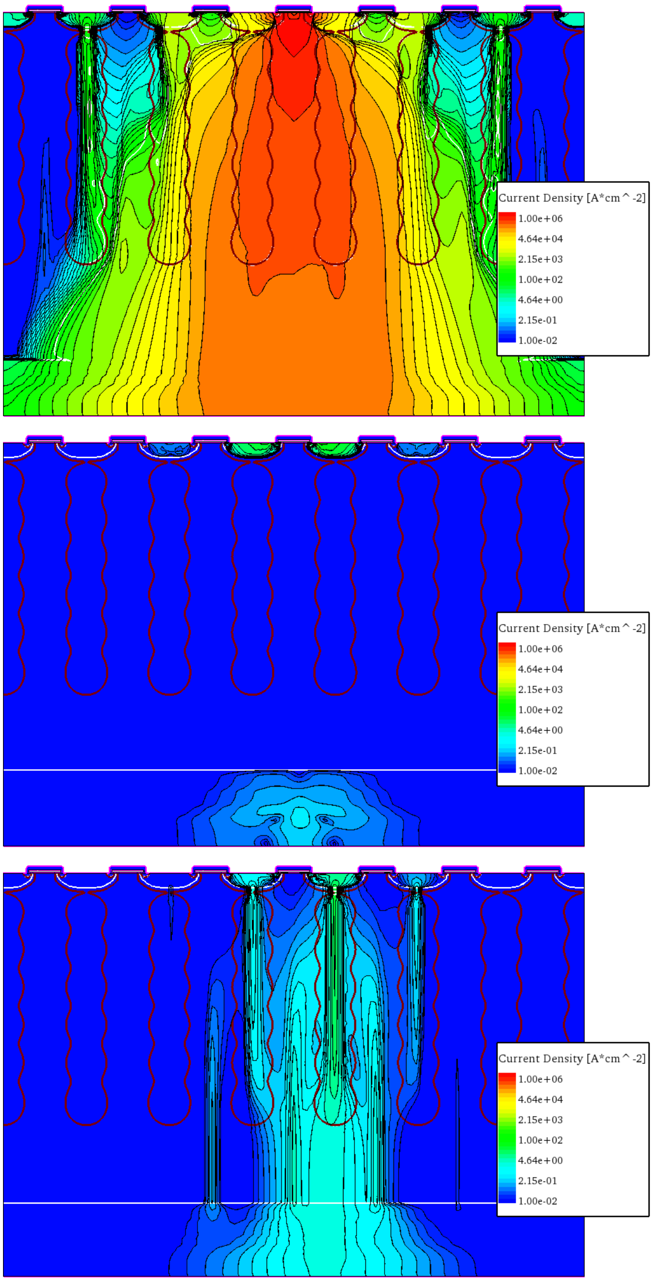

Figure 4.18: Current density distribution in the following conditions: $V_{ds} = 95\% BV_{dss}$, $t = 1.0 \times 10^{-8}$ s, ^{28}Si$(\mathrm{n}, \alpha)^{25}$Mg reaction in points A (upper figure) and C (intermediate figure) and ^{28}Si$(\mathrm{n}, \mathrm{p})^{28}$Al reaction in point A (lower figure)

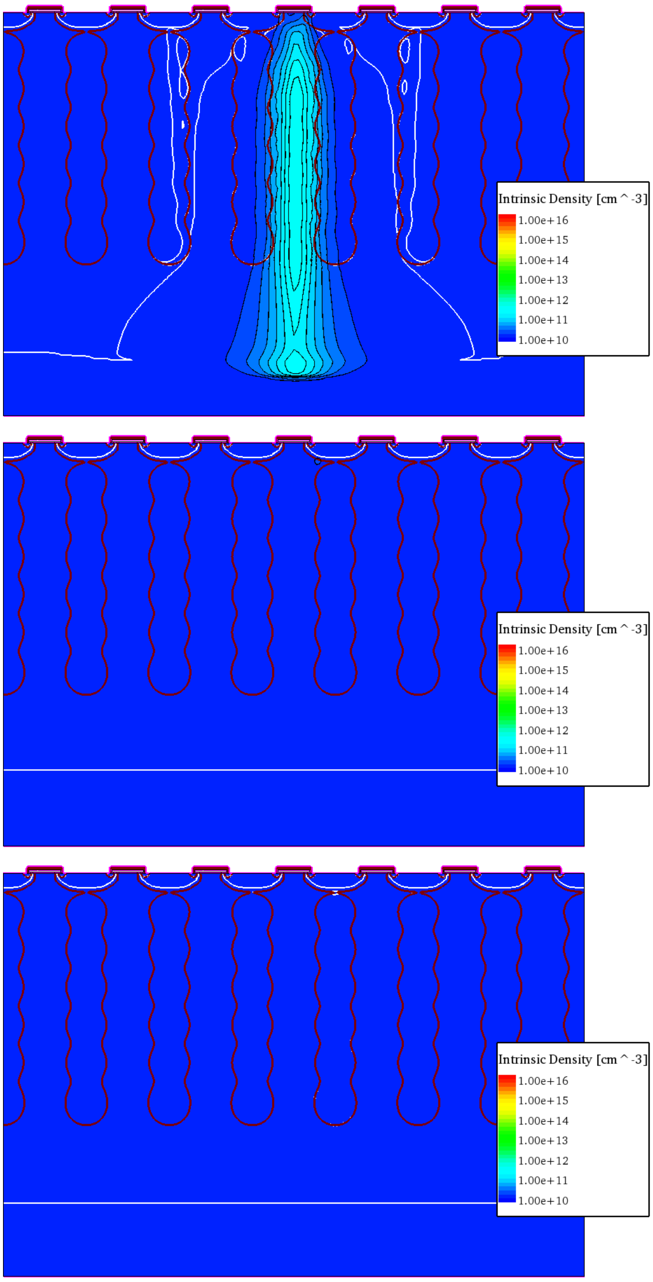

Figure 4.19: Intrinsic density distribution in the following conditions: $V_{ds} = 95\% BV_{dss}$, $t = 8.5 \times 10^{-9}$ s, $^{28}\mathrm{Si}(\mathrm{n}, \alpha)^{25}\mathrm{Mg}$ reaction in points A (upper figure) and C (intermediate figure) and $^{28}\mathrm{Si}(\mathrm{n}, \mathrm{p})^{28}\mathrm{Al}$ reaction in point A (lower figure)

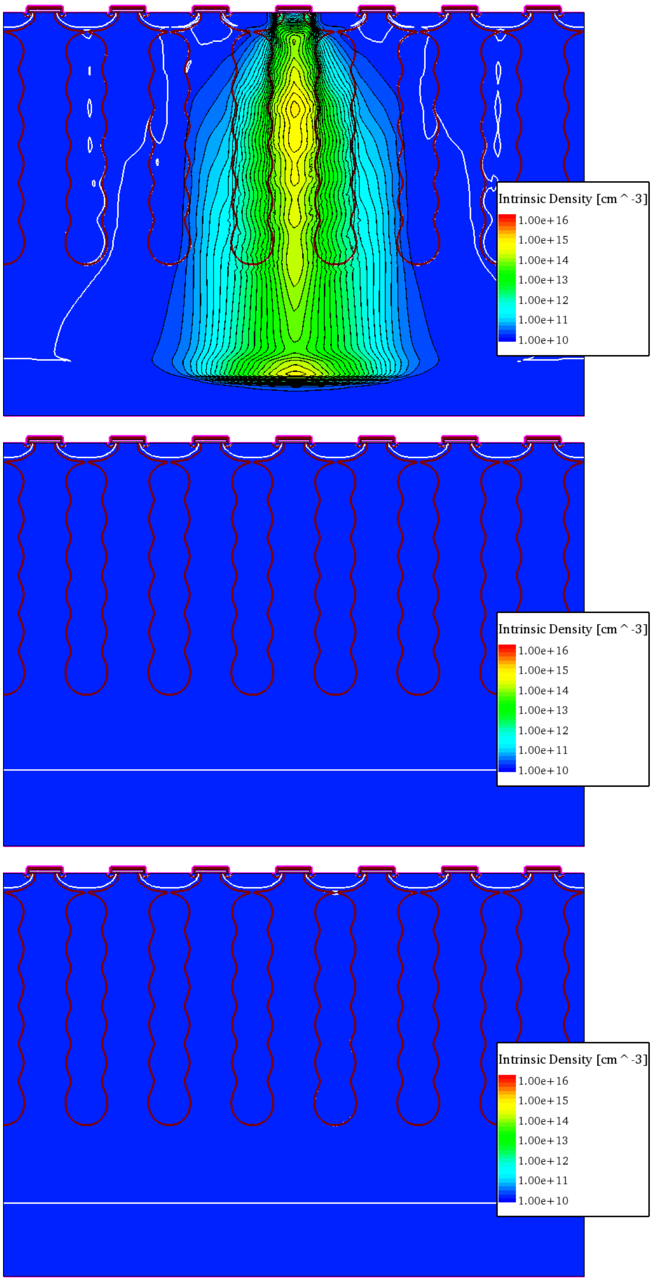

Figure 4.20: Intrinsic density distribution in the following conditions: $V_{ds} = 95\% BV_{dss}$, $t = 1.0 \times 10^{-8}$ s, $^{28}\mathrm{Si}(\mathrm{n}, \alpha)^{25}\mathrm{Mg}$ reaction in points A (upper figure) and C (intermediate figure) and $^{28}\mathrm{Si}(\mathrm{n}, \mathrm{p})^{28}\mathrm{Al}$ reaction in point A (lower figure)

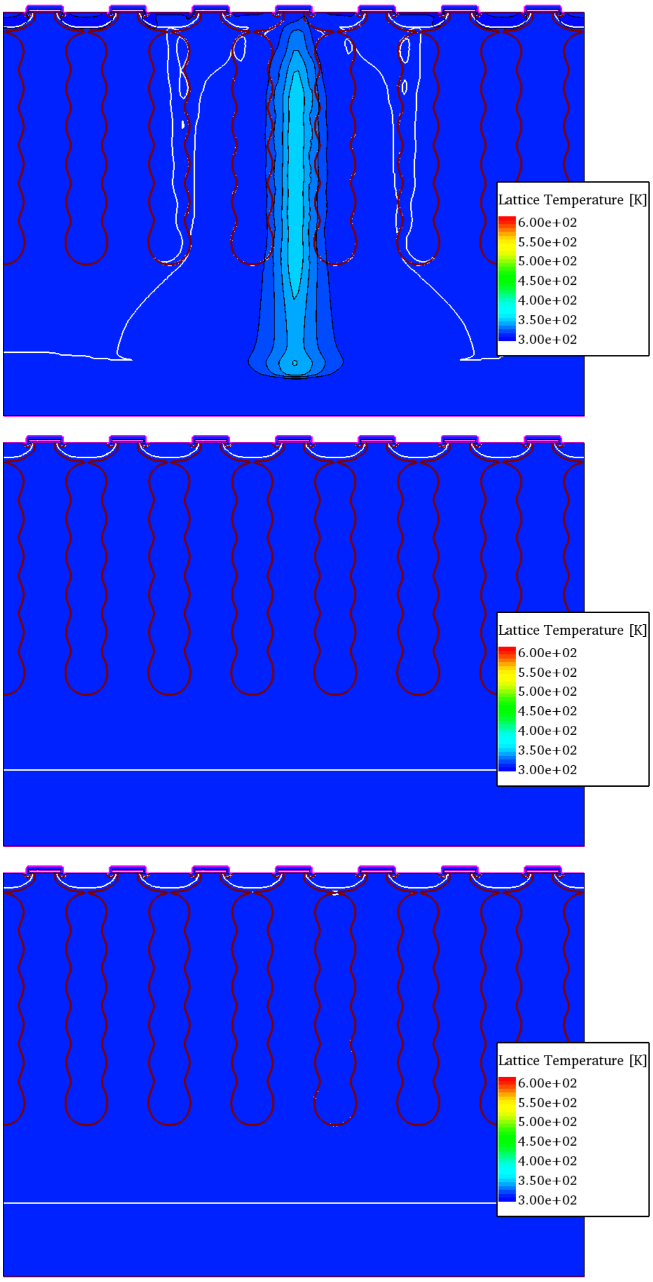

Figure 4.21: Lattice temperature distribution in the following conditions: $V_{ds} = 95\% BV_{dss}$, $t = 8.5 \times 10^{-9}$ s, $^{28}\text{Si}(\text{n}, \alpha)^{25}\text{Mg}$ reaction in points A (upper figure) and C (intermediate figure) and $^{28}\text{Si}(\text{n}, \text{p})^{28}\text{Al}$ reaction in point A (lower figure)

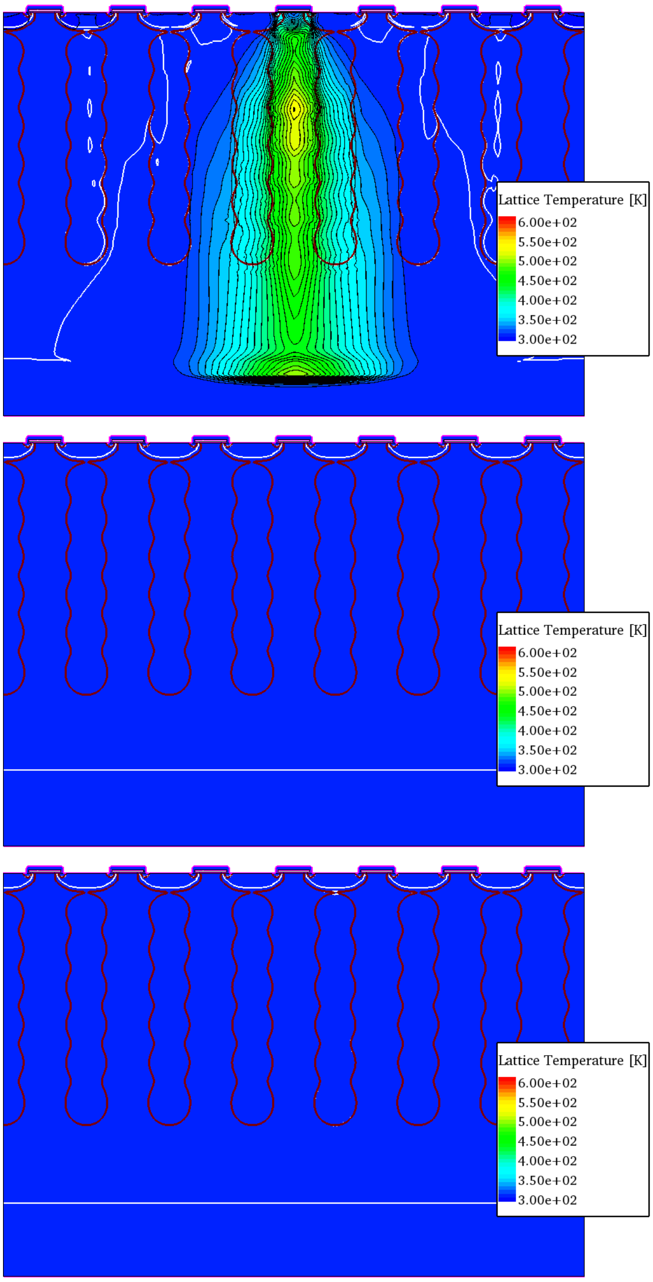

Figure 4.22: Lattice temperature distribution in the following conditions: $V_{ds} = 95\% BV_{dss}$, $t = 1.0 \times 10^{-8}$ s, $^{28}\mathrm{Si}(\mathrm{n},\alpha)^{25}\mathrm{Mg}$ reaction in points A (upper figure) and C (intermediate figure) and $^{28}\mathrm{Si}(\mathrm{n},\mathrm{p})^{28}\mathrm{Al}$ reaction in point A (lower figure)

4.6 3D simulations

3D simulations can be very burdensome from a computational point of view, especially with wide simulation domains and fine grids. Sometimes, convergence issues may also appear. Therefore it makes sense to run them only if they can give additional information compared to 2D simulations. For example, the sensitive volume can be properly evaluated only with 3D simulation because the charged particle induces a so high dense plasma that the carrier transport may be dominated by the minority carrier diffusion.

Because of the long-lasting elaboration times of 3D simulations, we simulated only few combination of test voltage, nuclear reaction and interaction point, based on the previous results. In particular, we simulated the alpha particle impact in the neck region, with the nominal breakdown as test voltage. However, we have no SEB because the drain current and the lattice temperature assume their pre-strike values, after a short transient. This result is in contradiction with the 2D simulations. In order to understand why, we inspected the structure files, performing both cutplanes and cutlines. We found that the excess carrier concentration near the interaction point is lower than the corresponding 2D case. In fact, the minority carrier diffusion occurs transversely with respect to the track but, in 2D simulations this can only have place along the y axis. Furthermore, the electric field distribution realizes a confinement effect between the pillars. In 3D simulation, the lateral diffusion occurs mainly along the z axis, thanks to the absence of strong electric fields. It follows a lower concentration of excess charge that is not sufficient to support the positive feedback which leads to SEB.

The LCD and range values that we used for the simulation are referred to the energy value of the reaction rate peak. However, several combinations are possible. The maximum LCD is obtained at the Bragg peak: under these conditions, the alpha particle has an energy of 0.46 MeV, it releases a charge of $1.6\,\mathrm{pC\,\mu m^{-1}}$ and make a path of $2.2\,\mathrm{\mu m}$. However, also in this case, the SEB is not triggered. On the contrary, because of the reduced range, the drain current pulse is less intense.

Finally, in order to assess the minimum LCD value required to induce SEB, we increase the LCD over the Bragg peak, keeping constant the range. We obtain SEB with an LCD greater than $2.0 \times 10^{-2}\,\mathrm{pC\,\mu m^{-1}}$, then a value not very far from the initial case. Note how the alpha particle can't release this charge into silicon. Assuming the 3D simulations are correct, this mean that SEB are not caused by alpha particles, but by other charged recoils resulting from nuclear interactions that we did not consider. On the other hand, if the 2D simulations are qualitatively correct, we can explain this incongruence with the lack of charge transport modeling or too loose mesh for the required accuracy.

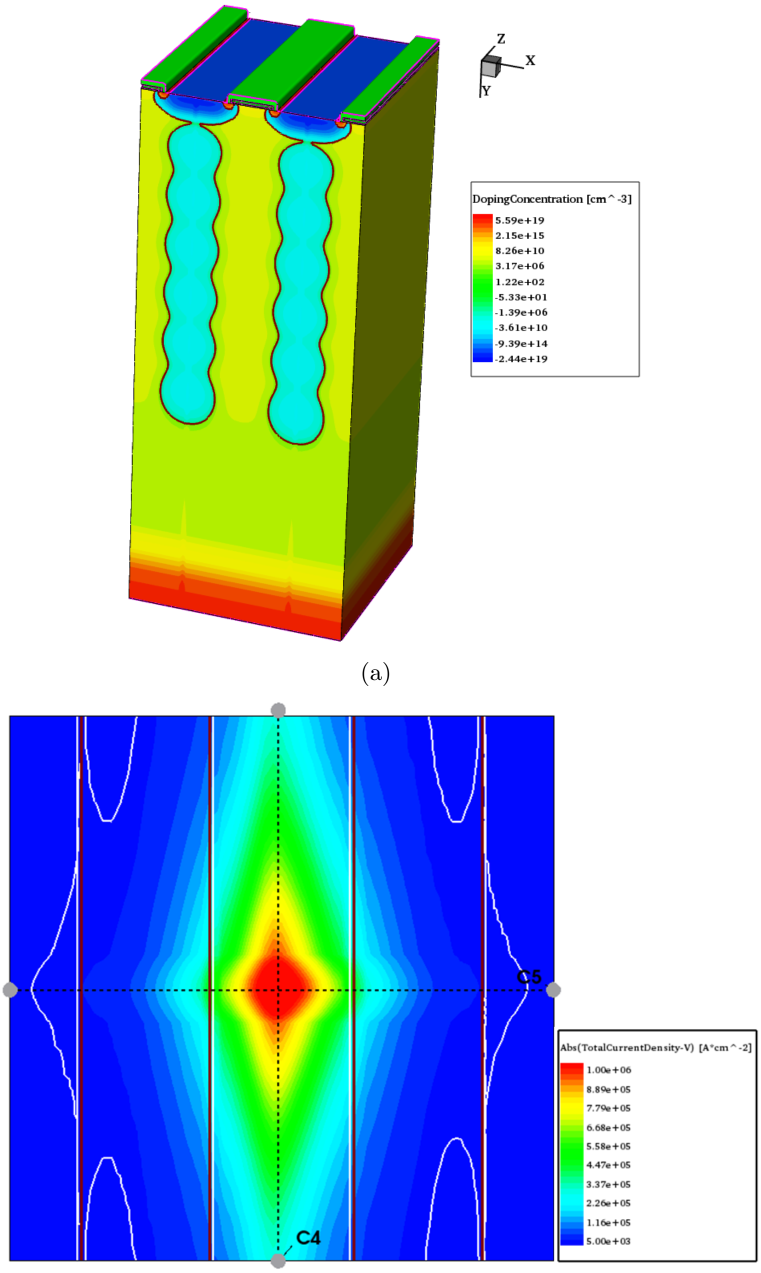

(a)

(b)

Figure 4.23: 3d device structure and xz cutplane

Bibliography chapter 4

[1] `http://www.synopsys.com/tools/tcad/Pages/default.aspx`.

[2] `http://www.srim.org`.

[3] M. Allenspach et al. "Evaluation of SEGR threshold in power MOSFETs". In: *Nuclear Science, IEEE Transactions on* 41.6 (Dec. 1994), pp. 2160–2166. ISSN: 0018-9499. DOI: `10.1109/23.340557`.

[4] P.A. Blakey. "Technology Computer Aided Design". In: *RF and Microwave Semiconductor Device Handbook*. CRC press, 2003.

[5] M.B. Chadwick et al. "ENDF/B-VII.1 Nuclear Data for Science and Technology: Cross Sections, Covariances, Fission Product Yields and Decay Data". In: *Nuclear Data Sheets* 112.12 (2011). Special Issue on ENDF/B-VII.1 Library, pp. 2887–2996. ISSN: 0090-3752. DOI: `http://dx.doi.org/10.1016/j.nds.2011.11.002`. URL: `http://www.sciencedirect.com/science/article/pii/S009037521100113X`.

[6] C. Dachs et al. "Evidence of the ion's impact position effect on SEB in N-channel power MOSFETs". In: *Nuclear Science, IEEE Transactions on* 41.6 (Dec. 1994), pp. 2167–2171. ISSN: 0018-9499. DOI: `10.1109/23.340558`.

[7] C. Dachs et al. "Evidence of the sensitivity inhomogeneity of power MOSFETs' cells to single event burnout". In: *Radiation and its Effects on Components and Systems, 1995. RADECS 95., Third European Conference on*. Sept. 1995, pp. 387–390. DOI: `10.1109/RADECS.1995.509807`.

[8] C. Dachs et al. "Simulation aided hardening of N-channel power MOSFETs to prevent single event burnout". In: *Nuclear Science, IEEE Transactions on* 42.6 (Dec. 1995), pp. 1935–1939. ISSN: 0018-9499. DOI: `10.1109/23.489237`.

[9] P.E. Dodd. "Physics-based simulation of single-event effects". In: *Device and Materials Reliability, IEEE Transactions on* 5.3 (Sept. 2005), pp. 343–357. ISSN: 1530-4388. DOI: `10.1109/TDMR.2005.855826`.

[10] K. Guetarni et al. "Transient device simulation of neutron-induced failure in IGBT: A first step for developing a compact predictive model". In: *Microelectronics Reliability* 53.9–11 (2013). European Symposium on Reliability of Electron Devices, Failure Physics and Analysis, pp. 1293–1299. ISSN: 0026-2714. DOI: `http://dx.doi.org/10.1016/j.microrel.2013.07.108`. URL: `http://www.sciencedirect.com/science/article/pii/S0026271413002849`.

[11] G.H. Johnson et al. “A review of the techniques used for modeling single-event effects in power MOSFETs”. In: *Nuclear Science, IEEE Transactions on* 43.2 (Apr. 1996), pp. 546–560. ISSN: 0018-9499. DOI: `10.1109/23.490900`.

[12] G.H. Johnson et al. “Simulating single-event burnout of n-channel power MOSFET’s”. In: *Electron Devices, IEEE Transactions on* 40.5 (May 1993), pp. 1001–1008. ISSN: 0018-9383. DOI: `10.1109/16.210211`.

[13] K. Krane. “Introductory Nuclear Physics”. In: "John Wiley and Sons", 1988. Chap. 11.

[14] S. Liu et al. “Single-Event Burnout and Avalanche Characteristics of Power DMOSFETs”. In: *Nuclear Science, IEEE Transactions on* 53.6 (Dec. 2006), pp. 3379–3385. ISSN: 0018-9499. DOI: `10.1109/TNS.2006.884971`.

[15] A. Porzio et al. “Experimental and 3D Simulation Study on the Role of the Parasitic BJT Activation in SEB/SEGR of Power MOSFET”. In: *Radiation and Its Effects on Components and Systems, 2005. RADECS 2005. 8th European Conference on.* Sept. 2005, pages. DOI: `10.1109/RADECS.2005.4365576`.

[16] F. Roubaud et al. “Experimental and 2D simulation study of the single-event burnout in N-channel power MOSFETs”. In: *Nuclear Science, IEEE Transactions on* 40.6 (Dec. 1993), pp. 1952–1958. ISSN: 0018-9499. DOI: `10.1109/23.273458`.

[17] *Sentaurus device user guide.* G-2012.06. Synopsys. June 2012.

[18] Tomoyuki Shoji, Shuichi Nishida, and Kimimori Hamada. “Triggering Mechanism for Neutron Induced Single-Event Burnout in Power Devices”. In: *Japanese Journal of Applied Physics* 52.4S (Apr. 2013), 04CP06. DOI: `10.7567/jjap.52.04cp06`. URL: `http://dx.doi.org/10.7567/JJAP.52.04CP06`.

[19] Tomoyuki Shoji et al. “Experimental and simulation studies of neutron-induced single-event burnout in SiC power diodes”. In: *Japanese Journal of Applied Physics* 53.4S (Jan. 2014), 04EP03. DOI: `10.7567/jjap.53.04ep03`. URL: `http://dx.doi.org/10.7567/JJAP.53.04EP03`.

[20] C. Sudre et al. “Application of Device Simulations to Radiation Hardening Studies”. In: *Solid State Device Research Conference, 1995. ESSDERC ’95. Proceedings of the 25th European.* Sept. 1995, pp. 315–319.

Conclusions

This thesis focused on neutron induced SEB, a catastrophic failure mechanism which power MOSFETs are prone to. SEB can adversely affect a device's performance and can cause system failure, if not properly evaluated. This issue does not only concern power transistors operating in harsh radiative environment, but it can occur even at sea level due the terrestrial neutrons. High voltage power MOSFETs (600 V or higher breakdown voltages - typically manufactured with the Super Junction technology) are more susceptible because of their wide epitaxial region.

Several COTS SJ power MOSFETs were characterized in terms of failure rate and MTTF, with the moderated Am-Be source at the University of Palermo and the ANITA source at the The Svedberg Lab in Uppsala. First of all, a custom measurement apparatus was designed in order to perform destructive SEB testing as in STD MIL. The system continuously acquires the drain voltages of the DUTs and save the failure times for each exposure. Other system's features are the modularity, i.e. the sample size can be incremented, adding other capacitor and DUT boards and the remote control. The MTTF and failure rate were esteemed with a statistical analysis, in accordance with the Weibull model: after calculating the empirical fraction yield against the exposure time, a non-linear fit allow to extrapolate the β and τ parameters of the Weibull function. As SEBs are random failures, the experimental β should be unitary and τ the MTTF reciprocal. The sample size influence over the extrapolated β accuracy was also investigated with a custom Montecarlo simulator. The main evidence is that a relative uncertainty of β lower than 15% could be obtained with at least 64 samples.

Several failures were observed during the experiments. In the failed DUTs, post irradiation electrical characterizations evidenced a strong increase in both I_{dss} and I_{gss} leakage currents, as their drain and source contacts were practically shorted. On the other side, no significant variations were noticed into electrical parameters of survived DUTs. The post-failure analysis was carried the microscope inspection and clearly evidenced burnout point sites, with a random distribution over the entire active area of the devices. The typical diameter of SEB trace is about 100 µm.

As for the ANITA experiment, we found that the repetition rate of the source and the distance from the target does not have a significant impact on the failure rate. Among the tested devices, the most reliable is the EIF7 (a 650 V Trench Field Stop IGBT), with a percentage threshold of 85%; among the power MOSFETs we have the 2M6L and 2F6L (600 V MDMesh devices) with a percentage threshold of 72.5%. However, to ensure the SEB immunity for voltages up to 600 V, we have to choose higher breakdown voltage devices such as the VJLL (950 V MDMesh device) with a resulting performance worsening in terms of on-resistance, although they have a lower SEB threshold percentage. The failure rate of the different DUTs, with a test voltage equal to the 15% more than the SEB threshold is about tens of thousands FITs.

UniPA tests were carried out exclusively on the VJLL device, because it resulted, from the ANITA experiment, one of the best candidates for photovoltaic applications. Its SEB threshold is around the 90% of the breakdown voltage, therefore it is higher than the value obtained with the ANITA source. This discrepancy is due to the neutrons with energies higher than 11 MeV: they can trigger more energetic secondary charged particles which in turn can induce a SEB at a lower test voltage. However, the moderated Am-Be neutron sources seems to be suited for engineering tests of radiation hardness evaluation. Furthermore, the SEB events observed at the UniPA source are not caused by radioactive decays, but are due to prompt emission of charged recoils.

The small sample size of the experiments involves a β relative uncertainty of 30%. In the next experiments, more DUTs per run should be tested, in order to achieve a more accurate estimation or, circumvention techniques should be adopted.

The SEB threshold of the VJLL was also characterized with TCAD tools. The simulation results were compared to the experimental result of the UniPA experiment. For this purpose, we used the transient domain analysis approach, usually used for heavy ion SEE simulations. A novel methodology was proposed to adopt the heavy ion model also for the charged recoils induced by the nuclear interactions. First, the most likely reactions was identified. In particular, all the two products nuclear reaction with all the nuclei target in the DUT were considered. Then, the related reaction rate was calculated, using the ENDF cross-section and the facility spectrum. The most likely reaction occurs in the passivation layer and consists in the thermal neutron capture by nitrogen, which determines the emission of a proton. The reaction rates peak is $23\,008\,\mathrm{s}^{-1}$ at the energy of 1×10^{-5} eV. Furthermore, this reaction has a positive Q-value, so it occurs spontaneously with a substantial net release of energy, despite the very low energy of the incident neutron. The same reaction may have place at higher energies, but with lower rates ($95\,\mathrm{s}^{-1}$ barn at 0.49 MeV and $58\,\mathrm{s}^{-1}$ at 1.35 MeV). The emitted proton may trigger SEB, if it crosses the metal layer and reaches the high electric field areas of the active region. All other reactions are characterized by peak values of reaction rates lower than 2-3 orders of magnitude. In the active area and in the substrate, the most likely reactions are related to the silicon, respectively, with a proton ($2063\,\mathrm{s}^{-1}$ at $7.7\,\mathrm{MeV}$) and an alpha particle ($1176\,\mathrm{s}^{-1}$ at $7.9\,\mathrm{MeV}$) emission. These data were used to calculate the reaction products energies and their respective Bragg curves in the silicon. Finally, a parametric simulation has been prepared with the following parameters: test voltage, nuclear reaction and interaction point inside the active area. The more relevant findings are as follows. As in the experiment, SEB occurs with a test voltage of $902.5\,\mathrm{V}$. They are caused by the $^{28}\mathrm{Si}(\mathrm{n},\alpha)^{25}\mathrm{Mg}$ reaction in the active area; the other reactions involving a proton as the light recoil, both in the active area, both in the passivation layer, did not induce failures. Moreover, only few interaction points are really effective, even for drain voltages higher than the SEB threshold: the most sensitive regions are the neck and the channel, in the first $30\,\mu\mathrm{m}$ from the silicon/metal boundary. A typical SEB event has the following features: the drain leakage current diverges, as well as the lattice temperature, exceeding the conventional thermal break criteria of $1000\,\mathrm{K}$. Actually the thermal runaway already occurs at about $600\,\mathrm{K}$: in this condition, silicon intrinsic carrier density, due to thermal generation effect, becomes as high as the n-pillar doping concentration, i.e. $1 \times 10^{15}\,\mathrm{cm}^{-3}$.

Advanced simulation tools for neutrons transport in matter are needed to apply the proposed approach with neutrons having energies greater than $20\,\mathrm{MeV}$.